6-14-2021

Development of Highly Functional, Surface Tunable, and Efficient Composite Coatings for Pool Boiling Heat Transfer Enhancement

Aniket Mohan Rishi
amr6756@rit.edu

R·I·T

Development of Highly Functional, Surface Tunable, and Efficient Composite Coatings for Pool Boiling Heat Transfer Enhancement

by

Aniket Mohan Rishi

A dissertation submitted in partial fulfillment of the requirements

for the degree of Doctorate of Philosophy in Microsystems Engineering

Microsystems Engineering Program

Kate Gleason College of Engineering

Rochester Institute of Technology

Rochester, New York

14th June 2021

Development of Highly Functional, Surface Tunable, and Efficient Composite Coatings for Pool Boiling Heat Transfer Enhancement

by

Aniket M. Rishi

Committee Approval:

We, the undersigned committee members, certify that we have advised and/or supervised the candidate on the work described in this dissertation. We further certify that we have reviewed the dissertation manuscript and approve it in partial fulfillment of the requirements of the degree of Doctor of Philosophy in Microsystems Engineering.

_____

Dr. Anju R. Gupta (Advisor) Date
Assistant Professor, Mechanical, Industrial and Manufacturing Engineering

_____

Dr. Satish G. Kandlikar (Co-advisor) Date
James E. Gleason Professor, Mechanical Engineering

_____

Dr. Robert Stevens Date
Associate Professor, Mechanical Engineering

_____

Dr. Ke Du Date
Assistant Professor, Mechanical Engineering

Certified by:

_____

Dr. Stefan Preble Date

Director, Microsystems Engineering Program

Abstract

Kate Gleason College of Engineering
Rochester Institute of Technology

Degree: Doctor of Philosophy **Program**: Microsystems Engineering
Authors Name: Aniket M. Rishi
Advisors Name: Dr. Anju R. Gupta, Dr. Satish G. Kandlikar

Dissertation Title: Development of Highly Functional, Surface Tunable, and Efficient Composite Coatings for Pool Boiling Heat Transfer Enhancement

Rapid growth and advancements in high-power electronic devices, IC chips, electric vehicles, and lithium-ion batteries have compelled the development of efficient and novel thermal management solutions. Currently used air and liquid cooling systems are unable to remove the heat efficiently due to significant pressure drops, temperature differences, and limited heat-carrying capacities. In contrast, phase-change cooling techniques can remove the larger amount of heat with higher efficiency while maintaining safer operational temperature ranges. Pool boiling heat transfer is a type of phase-change cooling technique in which vapor bubbles generated on the boiling surface carry away the heat. This pool boiling performance is limited by the maximum heat dissipation capacity, quantified by the Critical Heat Flux (CHF), and efficiency of the boiling surface, quantified by the Heat Transfer Coefficient (HTC). This work emphasizes on improving both CHF and HTC by developing highly surface functional and tunable microporous coatings using sintering and electrodeposition techniques.

Initially, graphene nanoplatelets/copper (GNP/Cu)-based composite coatings were developed using a multi-step electrodeposition technique. And 2% GNP/Cu coating rendered the highest reported CHF of 286 W/cm² and HTC of 204 kW/m²-°C with increased bond strength. To further enhance the cohesive and adhesive bond strength of the electrodeposited coatings, a novel multi-step electrodeposition technique was developed and tested on copper-based coatings. This technique dramatically improved the overall functionality, pool boiling performance, and durability of the coatings. Later, a sintering technique was used to develop the coatings using GNP and copper particles. Uniform spreading of GNP over the coatings was obtained via ball milling technique. This technique yielded a CHF of 239 W/cm² and the HTC of 285 kW/m²-°C (~91% and ~438% higher than a plain copper surface, respectively). A novel approach of salt-templated sintering was developed in the final part to attain a better control on porosity and wicking properties of the sintered coatings. This generated interconnected porous networks with a higher nucleating activity, and attained record-breaking CHF of 289 W/cm² and the HTC of 1,314 kW/m²-°C.

Acknowledgements

I would like to express my sincere gratitude to Dr. Anju Gupta and Dr. Satish Kandlikar for giving me this great opportunity to work in the Thermal Analysis, Microfluidics, and Fuel Cell Laboratory (TAMFL). Without their continuous support and guidance, this work would not have been possible. The confidence that you have shown in my work has encouraged me to deliver the best performance. I would also like to thank Dr. Kandlikar for giving numerous opportunities in different outreach and teaching activities.

I would like to thank my committee members Dr. Robert Stevens and Dr. Ke Du for taking time to review and evaluate my thesis work. I am grateful to the directors of the Microsystems Engineering PhD program - Dr. Bruce Smith and Dr. Stefan Preble. I would like to specially thank Dr. Surendra Gupta for giving me the training on XRD and Prof. Richard Hailstone for the assistance with SEM and TEM. I would like to thank all my TAMFL lab members, Aranya, Arvind, Pruthvik, Isaac, Alyssa, Indranil, Travis, Jose Luis, Poornima, Akshat, Farhan, Ishan, and Maharshi for their continuous support, encouragement, and assistance. I am really thankful to them for all the things they have done.

I would like to thank Lisa Zimmerman and all the staff from the Mechanical Engineering office for their continuous support and help. I would also like to thank Jan Maneti, Craig Arnold, and Ricky Wurzer for helping me in the machine shop. I also express my gratitude to William Finch for providing me with IT support whenever necessary.

Finally, I would like to thank my parents, my brother, and my sister-in-law for their continuous support, encouragement, and for showing the confidence in me. I would also like to thank my girlfriend Sharvari for being there all the time, being the best partner, and constantly supporting and motivating me throughout the journey. Thank you for making all the sacrifices and giving me the opportunity to have this wonderful experience. You all are my support system. I would also like to thank all my friends for all the support they have given me throughout this journey.

Table of Contents

List of figures

List of tables

Nomenclature

Symbol	Description	Units
A	Coated surface area	m²
B_y	Bias error	-
C_1	$1 + \cos\theta$	-
C_2	$\sin\theta$	-
$C_{p,l}$	Specific heat of liquid	J/kg-K
$C_{p,v}$	Specific heat of vapor	J/kg-K
d_B	Bubble diameter	N/m²
dT/dx	Temperature gradient	°C/m
F	Faraday's constant	Coulomb
g	Acceleration due to gravity	m/s²
h	Thickness of the deposition	m
h_{lv}, h_{fg}	Latent heat of vaporization	J/kg
k_{Cu}	Thermal conductivity of copper	W/m-K
M	Atomic weight	
n	Number of electrons	-
Q	Charge	
q"	Heat flux	W/m²
r	Roughness	-

r_c	Critical radius	m
r_{cmax}	Maximum critical radius of cavity	m
r_{cmin}	Minimum critical radius of cavity	m
T_1	Top thermocouple	°C
T_2	Middle thermocouple	°C
T_3	Bottom thermocouple	°C
T_{sat}	Saturation temperature of the fluid	°C
T_e	Wall temperature of the boiling surface	°C

Greek symbols

β, θ_r	Receding contact angle	Deg.
Φ	Angle of inclination	Deg.
δ_t	Thermal boundary layer thickness	m
μ_l	Dynamic viscosity	Ns/m²
μ_v	Dynamic viscosity of vapor	Ns/m^2
ρ_l	Density of liquid	kg/m^3
ρ_v	Density of vapor	kg/m^3
σ	Surface tension	N/m
Δx	Distance between two thermocouples	m
ΔT_{sat}	Wall superheat	°C
ΔT_{sub}	Subcooling temperature difference	°C

List of Abbreviations

CHF	Critical Heat Flux	W/cm^2
G	Graphene	-
GNP	Graphene nanoplatelets	-
GO	Graphene oxide	-
r-GNP	Reduced graphene nanoplatelets	-
r-GO	Reduced graphene oxide	-
HTC	Heat Transfer Coefficient	kW/m^2-°C

Chapter 1

1. Introduction

Heat transfer is a phenomenon in which heat is transferred from one medium to another through different modes, viz. conduction, convection, and radiation. Conduction and convection phenomena typically require an intervening medium for the heat transfer to occur effectively, while the radiation heat transfer occurs in the absence of an intervening medium. Convection heat transfer is one of the attractive modes of heat transfer as it allows higher heat removal capacities, and these techniques are either single-phase or two-phase.

Air- and water-cooling are single-phase cooling techniques that utilize sensible heat transfer for cooling and thus have limited heat transfer capabilities. Boiling utilizes latent heat due to which water or any liquid converts to vapor by absorbing a large amount of latent heat. Thus, boiling is one of the most efficient heat transfer techniques in which heat transfer occurs at low surface temperatures. Boiling heat transfer is of two types, viz. pool boiling and flow boiling. In pool boiling heat transfer, a pool of the fluid is held stationary while the natural convection causes the heat transfer. Whereas in a flow boiling system, forced convection regenerates the heat transfer. A two-phase cooling system is required to meet the high demands of electronics cooling due to its high capabilities to transfer heat.

1.1 Pool boiling heat transfer:

Pool boiling is a two-phase heat transfer technique in which the heater surface is immersed in a pool of stagnant liquid. Boiling occurs on the surface when the liquid reaches its saturation temperature. Due to the absence of forced convection in pool boiling, latent heat is absorbed by the fluid to change its phase. Figure 1 shows the schematic of a pool

boiling process, where heat transfer between a heater source and a boiling surface occurs via conduction. In contrast, the heat transfer between the boiling surface and a pool of liquid above the boiling surface takes place via convection. In comparison to flow boiling, pool boiling does not involve any moving parts, pumps, and motors, making it inexpensive and a simple mode of heat transfer. Enhancements in pool boiling aim towards enhancing the heat flux and lowering the surface temperature to ensure the wide operational range and safer operations by avoiding overheating and burn out of the boiling surfaces.

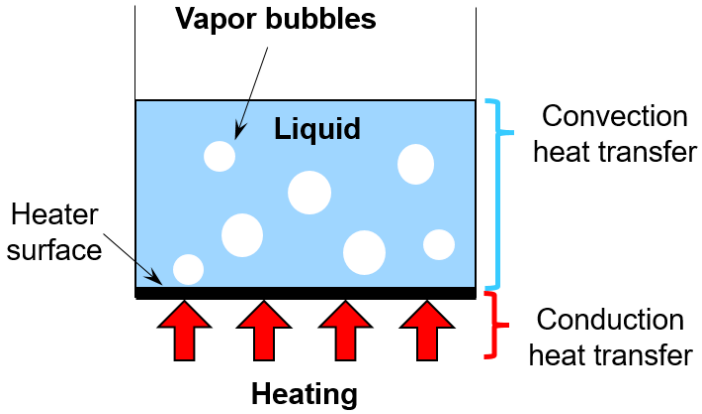

Figure 1. Schematic representation of typical pool boiling process

1.2 Pool boiling curve:

To understand the heat dissipation using boiling, it is essential to understand the pool boiling curve. A characteristic pool boiling curve is plotted with the heat flux on the y-axis and wall superheat on the x-axis. The pool boiling curve is the most fundamental curve that describes the four different stages of the pool boiling phenomenon's mechanisms underlying the pool boiling phenomenon, as shown in Figure 2. The four regimes of the plot are described below:

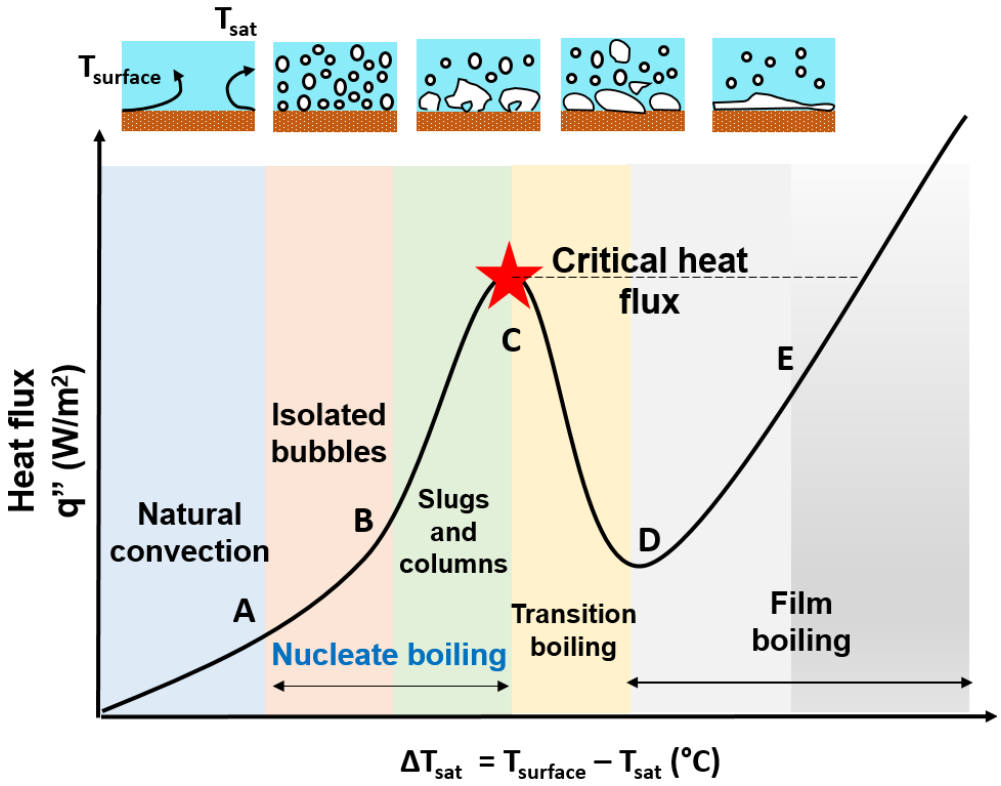

Figure 2. Pool boiling curve

1.2.1 Free convection boiling – natural convection process:

At low wall superheat, the heat is transferred from the boiling surface to bulk liquid by natural convection. There are no bubbles in this stage. When this temperature difference rises to a particular value corresponding to point 'A', a first vapor bubble appears on the surface. Till point A, heat transfer is by natural convection current, and the movement of liquid is due to the density variation.

1.2.2 Nucleate boiling – heat dissipation by bubbles:

Once the nucleation is initiated, under the right conditions, the vapor bubbles nucleate, grow, and depart from the boiling surface and rise to the free surface, shown by the nucleate boiling region in Figure 2 (point A to C). Region A to B in nucleate boiling is

considered as isolate bubbles region as distinct vapor bubbles nucleate from different nucleation cavities on the boiling surface. As the temperature rises beyond point B, additional nucleation sites become active. The rate of generation of bubbles increases which appears like columns of vapor bubbles are departing from the boiling surface. This rate of formation of bubbles increases rapidly, which in turn increases the heat dissipation rate significantly until point C. At this point, heat flux reaches the maximum value and is known as the Critical Heat Flux (CHF), which indicates the maximum heat that can be dissipated. The entire boiling surface gets covered with a thin layer of vapor at this point [1, 2].

1.2.3 Transition boiling – insulation layer of vapor:

Beyond point C, the bubble generation rate is much higher than the bubble detachment rate. The bubbles formed in this stage start to merge and form a layer of vapor film on the boiling surface that prevents any liquid from coming in contact with the surface. The vapor film acts as an insulation layer causing a rapid downfall in heat flux. Under these conditions, the surface temperature may fluctuate rapidly. Since the boiling in this region is the combination of unstable film boiling and nucleate boiling, it is called transition boiling.

1.2.4 Film boiling – heat transfer due to radiation:

In the region, D to E, there is a thin film of vapor covering the boiling surface completely. At this stage, heat transfer occurs by conduction and radiation from the wall through the vapor film. This vapor film does not wet the boiling surface, although some transient wetting can occur, and there can be a formation of bubbles in some regions. At the free interface, evaporation occurs, and bubbles then depart from the interface and rise

through the pool of liquid. Because the heat transfer in the region occurs through the vapor film, this stage is called film boiling.

Nucleate boiling is the main research interest area in all the pool boiling enhancement techniques. By focusing on enhancing CHF, which is the upper limit of maximum allowable heat transfer, and enhancing HTC, which determines how efficiently heat can be extracted from the boiling surface, increment in a wide range of applications and enhancing the safety of boiling surfaces can be achieved.

1.3 Bubble nucleation:

Bubble nucleation occurs when the boiling surface or the test surface submerged in a pool of liquid is at higher temperature than that of the saturation temperature of the bulk liquid above it.

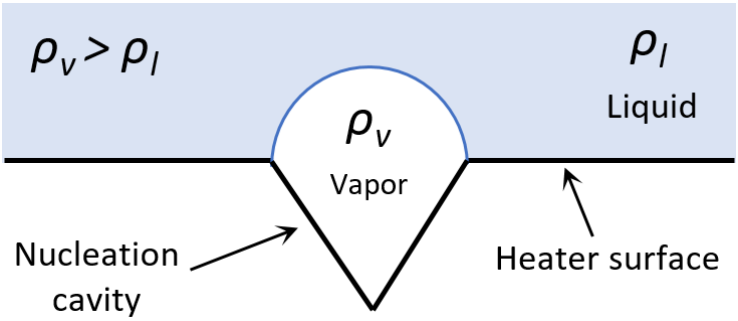

Figure 3. Nucleation of bubble

Figure 3 shows the various forces acting on the bubble, which are pressure force and surface tension force. Force balance of these gives the vapor pressure inside the bubble, and is given by [2],

$$\rho_V = \rho_l + \frac{2\sigma}{R} \quad (1)$$

Where, ρ_V is vapor pressure in the bubble, ρ_l is the pressure of the fluid, σ is the surface tension of the fluid and *R* is the radius of the bubble [2]. From Eq. 1, it is seen that vapor pressure is inversely proportional to the radius of the bubble. Therefore, even for the nucleation of a smaller bubble, higher vapor pressure will be required, which indicates that surface temperature should be higher than the fluid temperature [2,3].

$$\{r_{cmax}, r_{cmin}\} = \frac{\delta_t \sin\theta_r}{2.2}\left(\frac{\Delta T_{sat}}{\Delta T_{sat} + \Delta T_{sub}}\right)\left[1 \pm \sqrt{1} - \frac{8.8\sigma T_{sat}\,(\Delta T_{sat} + \Delta T_{sub})}{\rho_V h_{lv} \delta_t {T_{sat}}^2}\right] \quad (2)$$

Where, r_{cmax}, r_{cmin} are maximum and minimum radii of the cavities, δ_t is the thermal boundary layer thickness, θ_r is the receding contact angle, $\Delta T_{sat}, \Delta T_{sub}$ are wall superheat and subcooled temperature differences, σ is the surface tension, ρ_V density of the vapor, and h_{lv} latent heat of vaporization.

The equation above determines the range of radii of the cavity for nucleation. This implies that the cavities lying within this range will act as a nucleation site. The cavities are also dependent on the surface finish. For a very smooth and polished surface, higher wall superheat temperatures are required and this required high wall superheat is given by [4],

$$\Delta T_{sat,ONB\ at\ r_c} = \frac{1.1 r_c q''}{k_l \sin\theta_r} + \frac{2\sigma \sin\theta_r T_{sat}}{r_c \rho_v h_{lv}} \quad (3)$$

Where, r_c is the critical radius, q" is the heat flux, θ_r is the receding contact angle, σ is the surface tension, T_{sat} is the saturation temperature of the liquid, ρ_v is the density of vapor, and h_{lv} latent heat of vaporization.

1.4 Applications of pool boiling:

Pool boiling has a wide range of applications in the heat transfer field due to its very high latent heat absorption capacity. Critical heat flux (CHF) obtained during pool boiling establishes the operational range or limits of the heat dissipation capacity of the boiling surface. In contrast, the heat transfer coefficient (HTC) represents how efficiently this heat is being removed from the boiling surface. Depending on applications, enhancements in either CHF and/or HTC are desirable for most applications. Various applications can benefit from efficient pool boiling heat transfer. Some of these applications are discussed below:

1.4.1 Electronics cooling:

With the recent advancements in the field of microelectronics, micro-electro-mechanical systems (MEMS) and integrated electronic circuits, a significant increment in the number of smaller transistor devices in microelectronic chips and compact electronic package systems are being developed. However, with these advancements, higher heat fluxes are generated, and the necessity of efficient heat transfer and thermal management of electronic devices has increased more than ever. For the proper functioning of these devices, maintaining the desired surface temperatures is extremely critical. Currently, a single-phase i.e., air and/or water-cooling techniques are implemented to maintain the temperatures in data centers and electronic devices to their desired ranges. Figure 4 shows the heat transfer coefficients or the efficiencies of the cooling methods. Currently, 90% of data centers are either air or water-cooled. As observed from Fig. 4b, around 40% of the total power is utilized by only cooling systems and is expected to grow even further in the coming years. With the implementation of two-phase cooling technology, the power

required for cooling of data centers (server and rack level), supercomputers, and high energy density electronic devices can be reduced drastically due to the ability of a liquid to absorb a large amount of latent heat while changing its phase from liquid to vapor.

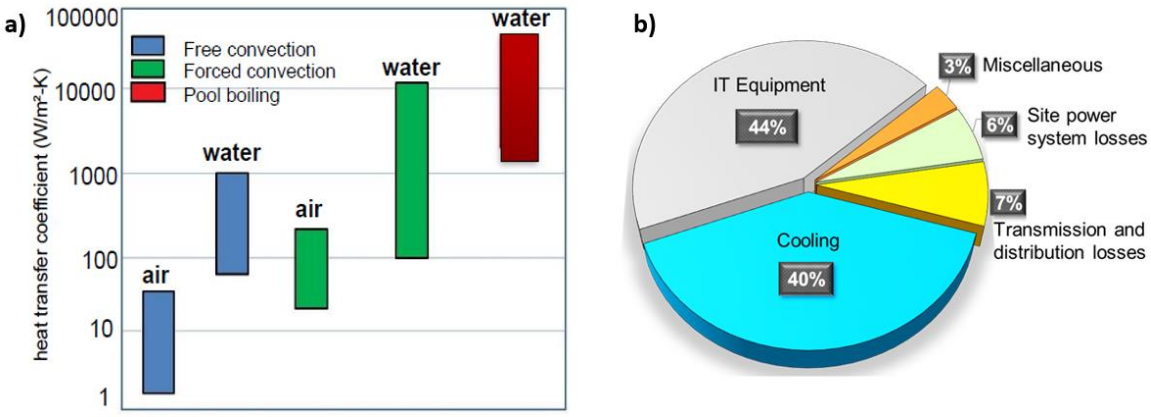

Figure 4. Heat transfer coefficients for single and two phase cooling [5]

1.4.2 Desalination:

The increasing scarcity of pure water in large cities all over the world is an extremely alarming situation. Desalination is a technique that basically uses sea water and makes it portable for human consumption as well as other applications, including agricultural and food industries by removing the salts from it. Thermal desalination is a type of technology that uses boiling or evaporation techniques to evaporate the seawater and produce fresh potable water. As the world moves toward renewable and clean energy sources, the integration of desalination plants with either wind or solar plants is expected to further improve the efficiencies of the desalination plants.

1.4.3 Reboilers and heat exchangers:

Kettle reboilers are most widely used in different chemical and gas processing industries. With more efficient boiling techniques, the vapor generation rate in these reboilers can be increased further to obtain more power output. Additionally, with improved boiling techniques, additional vapor can be generated for the same input power.

1.4.4 Distillation columns:

During the separation process in the distillation column, evaporation and boiling of a volatile liquid occur on the trays of distillation columns. By increasing the evaporation rate and/or boiling during this separation process, higher efficiency can be achieved for the same vapor input. Based on this, various surface enhancement techniques can be implemented on distillation plates to achieve improvement in evaporation and/or boiling.

1.4.5 Evaporators and heat pipes:

Boiling is an integral part of numerous refrigeration and air conditioning industries. The evaporators in refrigeration and air conditioners undergo boiling heat transfer on the tube bundles and flooded evaporators and chillers. Since the boiling points of the refrigerants used in the industries are very low, and their thermal conductivity is also lower, the overall performance and the efficiency of the systems are lower. The enhancements in boiling performances with better efficiency can directly impact refrigeration and air conditioning systems improvements, producing a significant impact on global warming due to these units.

1.5 Electrodeposition technique:

Electrochemical deposition is the process of coating solids on the conductive base materials to modify the surface properties. It consists of an electrolyte solution comprising positive and negative ions usually prepared from metal salts. The two working electrodes that can be of either conducting or semiconducting nature known as the cathode (on which the coating is desired) and an anode. The resultant electric current (rate of the motion of the electric charge) between the two electrodes under an external voltage is due to the migration and diffusion of the charged species. An electric voltage is an electric force per unit charge. The field direction is the force exerted on the positive charge and from the positive charge towards the negative charge.

The principle behind electrodeposition is to use an electric current to strip the cations from a sacrificial material (anode) in a solution and coat that material in the form of a thin film onto a conductive substrate (cathode). The electrodes are placed in the electrolyte solution containing both positively charged ions called cations and negatively charged ions called anions. When an external electric field is applied, the cations depart to the cathode and get deposited as metal. On the surface of the electrodes, conduction of ions to electrons takes place as a result of electrochemical reaction (or the redox reactions) that occurs between chemical species and the electrode. The reduction reactions occur at the substrate electrode, which is to be coated and involves the reduction of metal ions. And the oxidation reaction occurs at the counter electrode. According to which, the process follows Faraday's law, the amount of the deposited metal on the electrode is proportional to the applied current to the electrochemical cell [5].

$$Q = \frac{n*d*A*h*F}{M} \qquad (4)$$

Where, Q is the charge, n is no. of electrons, A is the coated surface area, h is the thickness of the deposition, F is Faraday's constant, and M is the atomic weight.

In this work, the duration of applied current is also taken into account.

$$Q = I * t \tag{5}$$

Where, Q is the charge applied, I is the amount of current supplied in mA, and t is the duration for which the current has been provided.

The electrodeposited metal under the applied current forms a uniform and continuous layer on the substrate electrode as a result of the interlocking of grains of the deposited metals, which further depends on the electric field distribution in the electrolyte. Hence, the composition of the electrolyte, ionic species, and their transport are additional factors in forming an electrodeposited layer with tunable morphology and tunable wetting and wicking characteristics. The transport of ionic species in the electrolyte depends on several mechanisms, including diffusion, migration, and convection. This work focuses on the diffusion process as the mode of transportation of the ions that form a gradient near the electrode surfaces. Redox reactions cause the depletion of the ions and their deposition on the substrate electrode via the formation of an electric double layer. This electric double layer is composed of – i) Helmholtz, a monolayer deposition of ions on the electrode surface, and ii) the Gouy-Chapman layer representing the electrolyte outside the Helmholtz layer that is composed of the bulk of the electrolyte with ionic species. Outside, this double layer is the diffusion layer that is wider than the double layer and is formed due to the change in concentration of ions during the deposition step. Other transport processes, including migration of the ions under an applied electric field and convection resulting from the changes in concentrations and temperature, also take place in addition to the

primary diffusion transport process. A multi-step electrodeposition technique includes multiple steps of varying current and time durations while performing the electrodeposition process. Each step has specific values of controlling parameters. The electrodeposition technique can be implemented on the substrate of any shape, size, and material. And its applications are not only limited to boiling heat transfer surfaces but also include any electroplating and coating-based applications. Some of the target applications include corrosion protection, decorative coatings, prolonged life of coating and surface, abrasion and wear resistance protection, durability to maintain the aesthetics, integrated electronics, solar reactors, fabrications, and others.

Dynamic template-assisted electrodeposition technique:

Template-assisted electrodeposition permits more size and shape-controlled deposition. The templates could either be dynamic, restrictive, or self-organized. In an aqueous solution, where electrolysis of water takes place in one of the electrochemical reactions, the evolved hydrogen serves as the dynamic template that results in porous surface coatings. The electrochemical reaction takes place when direct current is supplied through the electrochemical cell. First, hydrogen bubbles are formed on the cathode (substrate) at a higher current density supply. Typically, the electrolysis of water in the electrolyte creates hydrogen gas. If the evolution of bubbles is continued, the copper ions start to grow within the interstitial spaces between hydrogen bubbles. The resultant hydrogen bubbles behave as dynamic templates around which copper particles deposit and grow. When the higher current density supply is stopped, the hydrogen gas bubbles collapse, leaving behind the porous open network of copper. The bubble behavior determines the size of the pores, and the morphology of the metal film is determined by the nucleation and growth mechanism of the metal on the substrate. Thus, two simultaneous

reactions occur at the cathode, deposition of copper ions and the evolution of hydrogen bubbles. For electrolyte with copper sulfate, sulfuric acid, and water, the electrolyte reactions are given as follows.

At cathode: $Cu^{2+} + 2e^- \rightarrow Cu$

$2H^+ + 2e^- \rightarrow H_2\,(g)\uparrow$

At anode: $Cu \rightarrow Cu^{2+} + 2e$-

Electrolyte: $CuSO_4 \rightarrow Cu^{2+} + SO_4^{2-}$

$H_2SO_4 \rightarrow 2H^+ + SO_4^{2-}$

$H_2O \rightarrow H^+ + OH^-$

The hydrogen evolution reaction rate depends on the applied current density, which depends on the depositing metal-hydrogen chemisorption energy or the dissociation of hydrogen ions from the electrode surface that further combines with protons to form hydrogen gas. This is dependent on the current exchange density, which is defined as the rate of hydrogen evolution per surface area at the electrode. Metals that have weak interaction energy with hydrogen do not abet in the passage of sufficient electrons, whereas metals that interact strongly with hydrogen result in greater adherence to the surface and not getting released in the solution instantly. The applied current density and duration control the surface morphology characteristics such as porosity, thickness, wickability, wettability, contact angle, hydrophilicity, and hydrophobicity of the electrodeposited coatings. Bubble behavior dictates the size of the pores. A higher bubble generation rate

leads to shorter residence times that further control the coalescence of the bubbles. Reduced coalescence results in the smaller pore sizes of the deposited materials. Effectively, higher current density results in the production of the higher amount of hydrogen ions that result in the formation of hydrogen bubbles which provide the anatomy for the porous network and subsequent higher amounts of metal ions produced in this step get deposited around these hydrogen bubbles.

When direct current is supplied from the electrodeposition equipment, the anode loses its electrons, and the cathode gains the electrons. The current in the solution always flows from anode to cathode. The electrons freed from the anode to form the metal cations travel to the cathode and get deposited at the cathode. During the electrochemical reaction, the cathode undergoes reduction while the anode undergoes oxidation. According to Faraday's law of electrolysis [7], the amount of deposited material is proportional to the duration and time of the deposition. The deposition is usually accomplished using two methods: (i) supplying the constant current during the deposition process, and (ii) holding the constant potential during the electrodeposition. These methods are called as Galvanostatic and potentiostatic modes of deposition, respectively. In the current study, all the depositions are performed using the Galvanostatic method, i.e., the constant current is supplied for the fixed duration and the voltage is varied accordingly. By controlling the current density and time required for the deposition, the morphological structure and porosity of the coating can be controlled using the electrodeposition technique.

1.6 Sintering technique:

Sintering is the process of compacting a powdered material and forming a solid or porous mass by heat or pressure without melting it to the point of liquefaction. Sintering is a heat treatment process that is commonly used to increase the strength and structural integrity of the material. During a sintering process, the powder is heated at an appropriate temperature, pressure, and appropriate atmosphere to produce a coherent, predominantly solid structure. The produced coating provides a higher surface area to volume ratio compared to its bulk counterpart. Sintering strengthens the particle contacts by means of the thermal mass transport process and provides a change in porosity and pore geometry. Advantages of the sintering method over other coating processes include – controlled deposition for tunable coating thickness, the ability to coat substrates of varying shapes and thickness, and cost-effectiveness. Traditionally implemented sintering techniques yield coatings with uniform porous structure throughout the coating. Such sintering techniques are limited by their control over the resultant morphological features, such as porosity and pore diameter. This also limits the consequential surface properties such as wettability and wicking behavior of the coatings.

A sintering process is an irreversible event that happens in different stages. The sintering temperature during the process is always lower than the melting point of the metal in the material. However, it is high enough to promote neck formation at the point of contact between the adjacent particles. The process initiates with loose powders with a specific packing density if no compression is involved, as shown in Fig. 3 a). Initially, necks between the contacting particles grow to the point where the neck size is less than one-third of the particle size. During the next intermediate stage, with the continuation of

necking among the contacting particles, tubular pores start forming and are connected to the external surface. Finally, the necking state is achieved to a point where only a small porosity is available in the material. The grain boundaries are developed at these neck regions. The porosity is an inherent property during a sintering process and can be altered by changing the sintering time. The schematic of the different stages is shown in Figure 5.

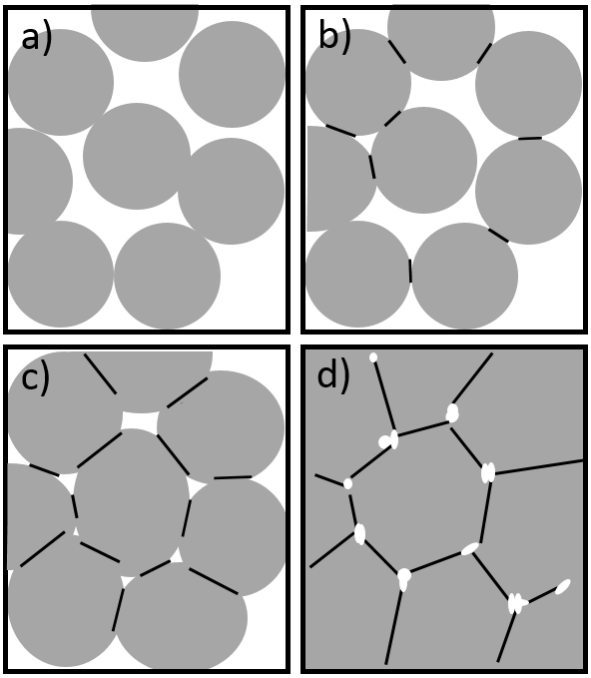

Figure 5. Illustration of the sintering stages showing the change in porosity at each stage a) loose powder, b) initial stage, c) intermediate stage, and d) final stage

The porosity of the coating is primarily dependent on the sintering time, sintering temperature, and the ratio of powder to sintering oil. Effectively, if the sintering temperature is less, the resultant coating cannot develop enough bonding between the particles due to low temperature. This can reflect in poor bond strength and removal of the coatings. A higher temperature can distort the shape of the particles. The sintering time also plays a crucial role in deciding the porosity of the coating. If the sintering time is less, the bond strength of the deposited coating is inadequate and fails to sustain vigorous forces.

And if the sintering time is more, it can reduce the porosity drastically. Thus, the sintering conditions control the surface morphological characteristics such as porosity and thickness and the subsequent surface properties such as wickability, wettability, contact angle, hydrophilicity, and hydrophobicity of the sintered coatings.

1.7 Graphene and graphene-based materials

Graphene is a two-dimensional form of graphite and consists of a tightly packed layer of carbon atoms that are bonded together in the form of a hexagonal lattice structure. Owing to its atomic layer thickness, a single layer of graphene possesses extremely high thermal, mechanical, and electrical properties. The thermal conductivity of a single layer of graphene can be reached in the range of 4000-5300 W/m-K. The extremely high in-plane thermal conductivity of graphene is primarily due to the sp^2-hybridized carbon atoms. In contrast, out-of-plane thermal conductivity is low because weak van der Waals interactions link the adjacent graphene planes within multilayer graphene.

1.7.1 Basics of sp^2-hybridization:

A carbon atom consists of six electrons and as per the energy states, 2 electrons are in 1s state and remaining 4 electrons occupy 2s and 2p orbitals. As shown in Fig. 6b, alternate carbon atoms are bonded via double bonds in case of the hexagonal structure of graphene. Due to similar energies of 2s and 2p orbitals, the electrons in these two orbitals arrange themselves such a way that 1 electron from 2s orbital shifts in p orbit and contribute to forming three sp^2-hybrid orbitals, while a remaining 1 electron in p orbital forms a pi-bond with the neighboring carbon atom. Three sp^2 hybridized carbon atoms are bonded via a strong covalent sigma bond to other carbon atoms. Figure 6c indicates the sp^2-

hybridization mechanism and the formation of 1 pi and three sigma bonds between 2 carbon atoms [8,9].

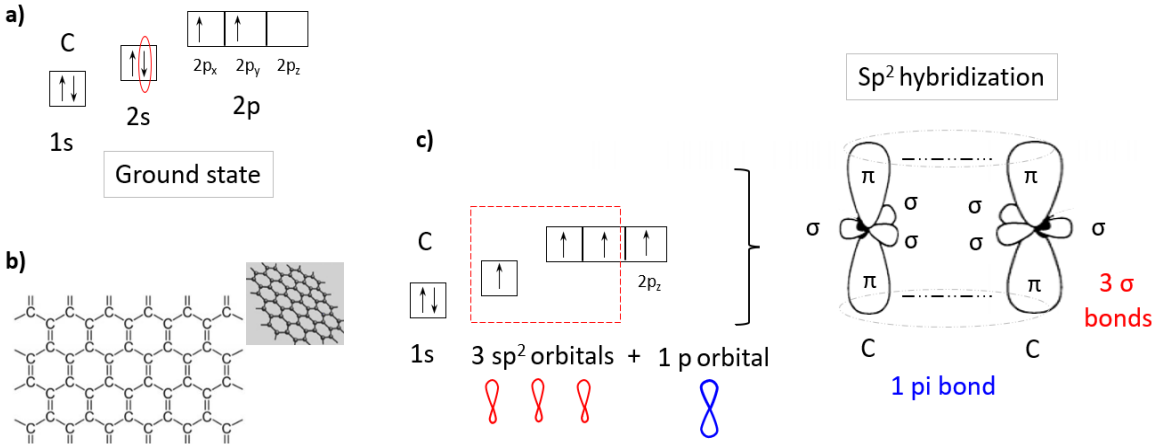

Figure 6. a) Distribution of electrons in a carbon atom in a ground state, b) Structure of a single layer of carbon atoms forming a hexagonal lattice structure of graphene, and c) sp2 hybridization of carbon atoms and formation of corresponding sigma and pi bonds

1.7.2 Graphene-based nanomaterials:

Manufacturing techniques for a single layer of graphene are expensive and time-consuming, leading to the development of more uncomplicated manufacturing techniques for developing different graphene derivatives. Some of the alternatives include graphene oxide, reduced graphene oxide, and graphene nanoplatelets. Compared to graphene, graphene oxide (GO) has additional oxygen, hydroxyl, and carboxyl groups attached to the hexagonal lattice of carbon atoms. Due to the presence of these groups, the thermal conductivity of GO is less than pristine graphene, while the wettability of GO is higher. Graphene oxide can further be reduced to form reduced graphene oxide (rGO) by eliminating the oxygen-based groups. Defects in graphene correspond to the breaking of the symmetry of honeycomb lattice carbon structure, including edge defect, grain

boundaries defect, and defects associated with the change of hybridization of carbon from sp^2 into sp^3. The amount and nature of defects strongly depend on the production method and can have a strong influence on the properties of graphene. Graphene nanoplatelets (GNP) are another type of graphene comprising a few graphene layers tightly packed together in a hexagonal lattice structure. And despite their multilayer structure, GNP can yield thermal conductivity in the range of 2500-3500 W/m-K, comparable to a single layer of graphene. Additionally, GNP have higher wettability than pristine graphene.

1.8 Composite coatings:

Pool boiling performance enhancements using deposition of composite coatings have been reported extensively. Composite coatings represent the deposition of a material using more than one metal and/or non-metal on the boiling surface by means of various deposition techniques. And these composite coatings typically attain higher critical heat fluxes at low wall superheats due to the formation of porosity which results in increment in surface area and nucleation sites available for boiling. Electrodeposition, dip coating, chemical and physical vapor deposition, and sintering are some of the simple deposition techniques that are typically used to develop the composite coatings not only for pool boiling enhancement applications but also for a variety of different industrial applications, including water desalination, vapor chambers, electrodes of lithium-ion batteries, evaporation heat transfer.

To be effectively tested for pool boiling, the bond strength of the porous surfaces must be strong enough to sustain the vigorous boiling without peeling off from the boiling surface. Steady vapor formation takes place on the porous media and the nucleation takes place within the matrix via the re-entrant cavities that are not susceptible to flooding by

liquid. When the heat is supplied to the boiling surface, the nucleus of a bubble grows in the cavity. The cavities may be formed inside the porous matrix or may appear on the surface of the coating. When this bubble nucleates, it carries heat with itself. As the bubble departs, the liquid in the vicinity of the void fills the cavity; thus, there is a continuous supply of fluid for evaporation. Higher the nucleation frequency, the higher the heat dissipated from the surface. Further, the agitation caused by the bubble activity may increase the heat transfer rate between the surface and the liquid.

1.9 Structure of dissertation:

This dissertation is structured as follow:

Chapter 1 (Introduction and background): The basic concepts and underlying physical mechanisms in boiling heat transfer and their relevance to industrial applications are highlighted. Details about the mechanisms of coating techniques and graphene chemistry have also been introduced in this section.

Chapter 2 (Literature review and research needs): This section reviews the recent advances and notable contributions in enhancing pool boiling heat transfer performances. A perspective of the mechanistic evolution of surface modifications and coatings along with a critical review is provided.

Chapter 3 (Approach and experimental details): The mechanical design and fabrication details of the basic test section components are described. The experimental procedure and protocols followed during the experimental testing are presented. Heat loss and uncertainty analysis arising from the instrumentation and testing is also explained.

Chapter 4 (Results and Discussion): The results are presented in four main sections classified based on the deposition technique used for developing multiscale morphological coatings.

Chapter 5 (Summary and major accomplishments): The section outlines the accomplishments achieved in this work using deposition techniques and their enhancement mechanisms. The societal context in terms of targeted industrial applications is also described in this section.

Chapter 6 and 7: This part represents the references and appendices, respectively.

Chapter 2

2. Literature review

This section covers a detailed literature review on different coating techniques and performance of boiling surfaces with porous media, and the mechanisms involved for the enhancements in boiling heat transfer. A critical review of each enhancement technique is also presented. The different coating techniques that alter the various surface properties such as wettability, wickability, porosity, and morphology to increase the boiling efficiencies and performance will be covered.

2.1 Enhanced heat transfer – Microporous surfaces

Pool boiling performance of the microporous surfaces has been reported extensively. Various techniques such as sintering, plasma coating, spraying, welding, or brazing have been implemented to deposit the micro and nanoscale coatings. Bargles and Chyu [10] demonstrated that a steady vapor formation occurs on the porous media and the nucleation occurs within the matrix via the re-entrant cavities that are not susceptible to flooding by liquid. When the heat is supplied, bubble nucleation carries heat with itself. As the bubble departs, the liquid in the vicinity of the void fills the cavity; thus, there is a continuous supply of fluid for evaporation (Fig. 7). Higher nucleation frequency ensures higher heat dissipated from the surface. [5]

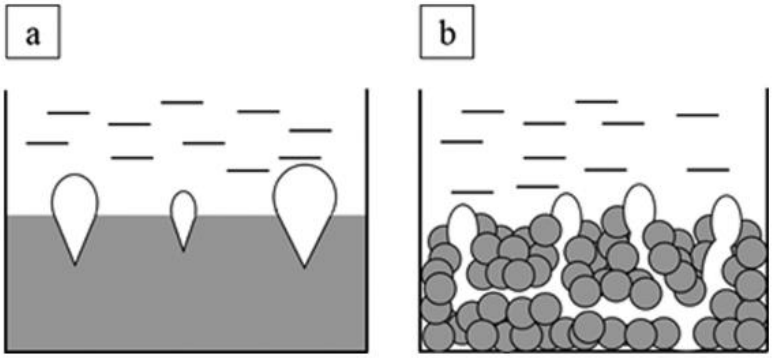

Figure 7. Bubble nucleation from a surface on a) Plain surface with discrete cavity structure, b) Porous network [12]

Webb [13] conducted a series of boiling experiments to study the effect of geometric parameters of porous coatings like particle size, pore size and coating thickness. The results revealed that a maximum HTC was obtained with a porous coating thickness of roughly four to six times the particle diameter. Additionally, it was suggested that the pore size has a more significant role compared to the overall porosity in enhancing the boiling heat transfer performance of porous surfaces. Mori and Okuyama [14] enhanced CHF by the attachment of a honeycomb structured porous plate with different thicknesses (1.2 mm, 5 mm, 10 mm) on a heated surface. As the thickness of the porous honeycomb plate on the heated surface decreased, the CHF increased to 250 W/cm². They found that the self-regulated liquid supply due to capillary action and reduced flow resistance to liquid and vapor flow improved the heat transfer. Jun et al. [15] developed porous copper coatings on copper substrates using a brazing technique with various thicknesses. They achieved a maximum CHF of 210 W/cm² for 67 µm thick coating, which is two times that of a plain copper surface. In addition to higher wicking due to capillary forces and microporous network, higher vapor velocity due to smaller vapor column size is responsible for the higher performance.

Li et al. [16] developed various microstructures, nanostructures, and hybrid micro, nano structures on copper surfaces and discovered that the CHF for hybrid surfaces was about 15% more than that of the only nanowires and micro pillars. CHF of 250 W/cm^2 at wall superheat of 28°C was reached for the combined micro-pillar and nanowire sample. Litter and Kaviany [17] developed porous coating using spherical particles of copper, with an average diameter of 200 μm on a copper substrate. They compared the developed porous surfaces with untreated surfaces for pool boiling and reported enhancement of CHF up to 3 times.

2.2 Heat transfer improvement – Effect of wettability and wickability

Wickability and wettability are the most critical surface properties of the boiling surface, influencing the CHF and HTC in pool boiling. Kandlikar [12] developed a theoretical model to describe the hydrodynamic behavior of the vapor-liquid interface of a bubble leading to the initiation of CHF. In general, surfaces with high wettability have been identified to enhance phase change heat transfer. Hydrophilic networks assist in delaying the formation of an insulating vapor layer on the boiling surface. Different networks were evaluated by Betz et al. [13], and it was found that the hydrophobic surfaces promote the nucleation at the beginning, which results in boiling at low wall superheat, with increased heat flux. In comparison, the hydrophilic network promotes a higher heat flux by delaying the formation of the insulation vapor layer.

Chu and co-workers [19] fabricated structures using electrophoretic deposition of silica nanoparticles on microstructured silicon and electroplated copper microstructures covered with copper oxide (CuO) nanostructures (Fig. 8a) to increase the surface roughness. They increased the CHF performance by ~200%. Kim et al. manipulated the

characteristic lengths of hexagonally arranged nanopillars (Fig. 8c) within sub-micron range using lithography techniques. Strong wicking gave the improvement of ~164% in CHF than the plain surface. Strong wicking enhanced the boiling performance by ensuring hydrodynamic stability as against surface dry-out. Yao et al. [20] developed a new technique to directly grow copper nanowires using electrochemical deposition (Fig. 8b) to increase the hydrophilicity of the coatings and in turn the pool boiling performance. They found that performance increased with the increase in nanowires height up to a certain limit and CHF of 164 W/cm² at 11°C was achieved for 35 µm height. Rahman et al. [21] used bio-templated virus to generate micro pillar wick structures (Fig. 8d) and demonstrated that the wickability is the dominant factor dictating the CHF of structured surfaces. This technique demonstrated that the wicked volume flux underneath a growing bubble determined the increase in CHF up to 257 W/cm².

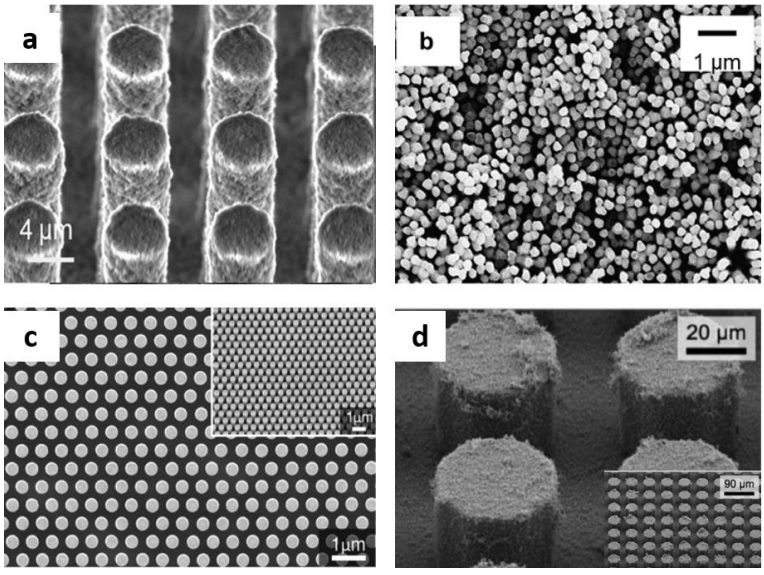

Figure 8. Comparison of morphological wicking structures prepared with different techniques a) Electrophoretic deposition of silica, micropillars in a square array [19] b) Electrochemical deposition of copper nanowires on silicon substrate [20], c) Silicon nanopillars structure using lithography technique [19], d) Silicon surfaces coated with TMV-templated nickel nanostructures [21]

2.3 Enhancement in heat transfer performance – Carbon derivatives

Carbon and carbon derivatives have shown promising enhancements in pool boiling applications. Researchers have developed various techniques to create the deposition of carbon-based coatings on boiling surfaces. Typically, this can be divided into three major parts: i) Formation of coating on the boiling surface as a result of boiling with carbon-based nanofluids, ii) Formation of carbon nanotubes (CNT) based coatings on the boiling surfaces, and iii) Formation of graphene-based coatings on the boiling surfaces.

2.3.1 Pool boiling enhancement with carbon-based nanofluids (active technique):

Nanofluids have emerged as a new type of heat transfer fluid in recent years, which contains nanometer-sized particles in a colloidal form. In the case of pool boiling, high thermal conductivity and self-assembly of nanofluids are the primary requirements to enhance the performance. With the advent of carbon-based nanomaterials, various carbon-based nanofluids have been explored for pool boiling enhancement due to their higher thermal properties.

Park et al. [22] used graphene/graphene oxide nanofluids on the wire and enhanced the CHF by ~179%. They proposed that a self-assembled porous structure and a change in critical distance between vapor columns on the boiling surface are responsible for the enhancement. Sarafraz and Hormozi [23] instigated carbon nanotube-based nanofluids on micro-finned surfaces with 0.1 and 0.3 wt. %. Reduction in fouling rate, intensification in bubble rate formation, and local agitation are responsible for increment in performance. Azizi et al. [24] added gum-arabic to enhance the dispensability of the graphene in water for testing a thermal performance of a two-phase closed thermosiphon. The highest thermal efficiency for thermosiphon was attained for 1 wt. % graphene. Kim et al. [25] prepared

composite coatings with micropillar arrays and implemented them with reduced graphene oxide colloids as the working fluid to enhance the pool boiling performance. Arrays were prepared by dry-etching and the graphene was pre-coated by boiling at a particular heat flux. They found that thick graphene coatings reduce the performance (~185 W/cm²) compared to the coatings only on the heads of the pillars (~205 W/cm²). Ahn et al. [26] sprayed reduced graphene oxide (rGO) flakes on copper substrates. The rGO colloid was synthesized by chemical reduction of hydrazine from graphene oxide. They identified that increased wettability and increase in the percentage of GO led to significantly enhanced boiling characteristics.

Ahn et al. [27] postulated that the thermal conductivity of rGO played a significant role in increasing the CHF while the wall temperature did not increase rapidly. In another study, Kim et al. reported high hydrophobic wetting as a consequence of layer build upon the substrates. The large thermal conductivity of GO layer inhibited the formation of local hotspots and prevented the formation of dry-out regions, which improved the CHF.

2.3.2 Carbon nanotube (CNT)-based coatings on the boiling surface (passive technique):

Carbon nanotubes (CNT, 1-100 nm diameter and 1-50 μm length) have been exploited by numerous researchers to utilize their high thermal conductivity. Typically, CNT can be single-walled or multi-walled made from a single sheet and multiple sheets of graphene, respectively. CNT possesses very high mechanical and thermal properties, due to which various studies have been performed to enhance the pool boiling heat transfer performance.

Ujereh et al. [28] grew multi-walled carbon nanotubes (MWCNT) using a plasma-enhanced chemical vapor deposition technique on a copper surface (Fig. 9a) to enhance pool boiling performance with FC-72. They achieved an increment of 6% and 33% in CHF and HTC, respectively, when compared to the plain copper surface. Deeper liquid penetration and the reservoir-type function of CNT were responsible for the improvement in performance. Similar work with MWCNT (Fig. 9e) has shown the enhancement of ~27% in CHF for silicon surfaces [29]. Seo et al. [30] coated single-walled carbon nanotubes (SWCNT) on a stainless steel surface (Fig. 9b) and enhanced the performance by 55% compared to plain stainless steel surfaces and identified the increased porosity as the responsible factor for the improvement. Zheng and Park [31] electrostatically sprayed and sintered copper and CNT composite powder on copper substrates (Fig. 9f) for testing with R134a refrigerant. Even though the significant enhancement was not achieved, early nucleation was obtained for 20 vol. % MWCNT content. Lee et al. [32] developed layer-by-layer-assembled poly-ethylenimine (PEI)-multi-walled carbon nanotube (MWCNT) coatings on stainless steel (Fig. 9d). Compared to bare stainless steel, they achieved ~147% enhancement in CHF owing to the formation of nano-cavities and inner nanoporous structures. Dharmendra et al. [33] coated carbon nanotubes on bare copper surfaces (Fig. 9c) and achieved an enhancement of 38% in CHF. They attributed this enhancement to the increment in surface roughness and hydrophobicity of the coatings. It has been observed that similar morphologies are achieved in most of the CNT based coatings and they do not yield a very high performance. Additionally, the coating and manufacturing process of CNT is complex and time consuming, and thus it is not feasible to implement CNT based coatings for improving pool boiling performance.

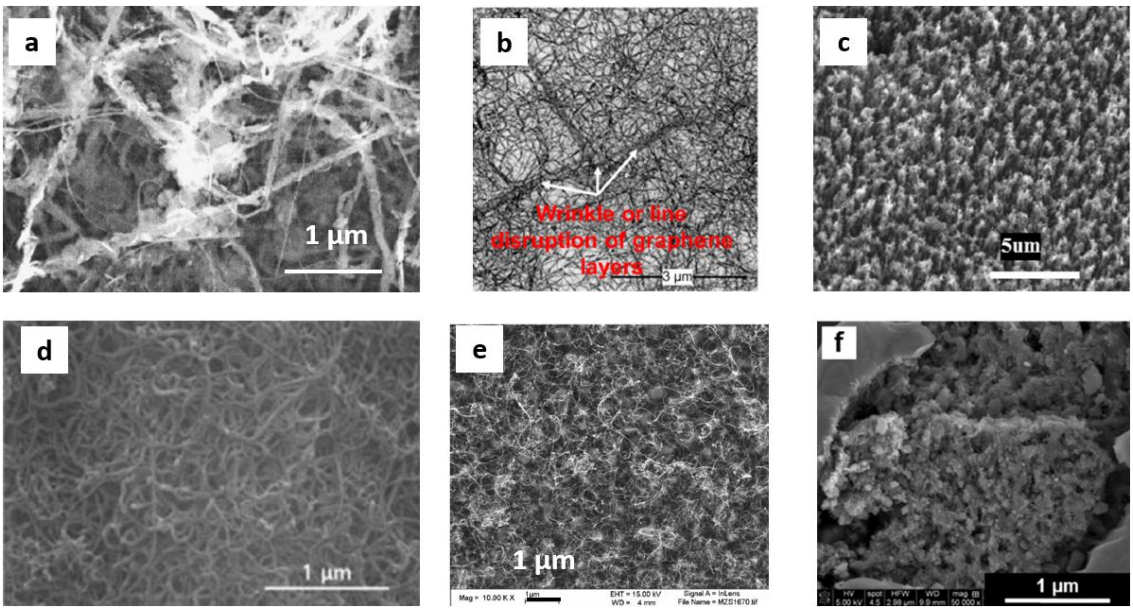

Figure 9. Comparison of scanning electron microscope images of morphological structures of various coatings a) CNT-coated copper [28], b) Hybrid graphene/SWCNT surface [33], c) CNT on bare copper [33], d) Layer-by-layer-assembled PEI-MWCNT on stainless steel [32], e) MWCNT on silicon [29], and f) Cu-MWCNT sintered composite coating with 20 vol. % MWCNT [31]

2.3.3 Graphene (G) and/or graphene oxide (GO)-based coatings for pool boiling enhancement (passive technique):

Since the successful synthesis of the world's thinnest material, graphene, numerous studies have been carried out to coat graphene and graphene derivatives to enhance the pool boiling performance. A study by Protich et al. [34] involved electrochemical deposition of copper in graphene quantum dot bath. A string-like structure of composite was obtained, which gave CHF of 216 W/cm² and HTC of 86 kW/m²-°C. The improved performance was obtained due to the higher thermal conductivity of graphene layers arising from the porous surface with increased surface area. Jin et al. [35] tested the graphite foams with FC-72 and HFE-7000 for the pool boiling enhancement. Two porous foams (30 x 30 x 20 mm) with similar porosity but different pore diameters (0.31 mm and 0.5 mm) were tested. Wall superheat below 100°C was maintained by graphite foams at a heat flux of

112 W/cm², while it was 105°C for the copper block at a heat flux of just 56 W/cm². They found that thermal conductivity and pore size are interrelated factors, indicating an increase in the pore size with a reduction of effective thermal conductivity due to the increased void volume.

An et al. [36] sprayed reduced graphene oxide (rGO) flakes on the copper substrates and increased the CHF to ~150 W/cm². They found the increment in nucleation sites and increased wettability were responsible for higher performance. Sadaghiani et al. [12] coated three-dimensional foam-like graphene on silicon surfaces using chemical vapor deposition (Fig. 10d). They found an optimum thickness for the higher pool boiling performance and concluded that the thick coatings affected the bubble dynamics, i.e., bubble departure diameter and bubble frequency. A slight improvement in CHF and ~50% in HTC was obtained for the 13 nm thick graphene coating as compared to the plain silicon surface. Seo et al. [37] developed porous graphene layers on the Indium Tin Oxide surface (Fig. 10c) using plasma-enhanced chemical vapor deposition and improved CHF values by 90% compared to the plain surface. The increment in porosity and permeability and their effect on capillary pumping limit were the responsible factors for the enhancement.

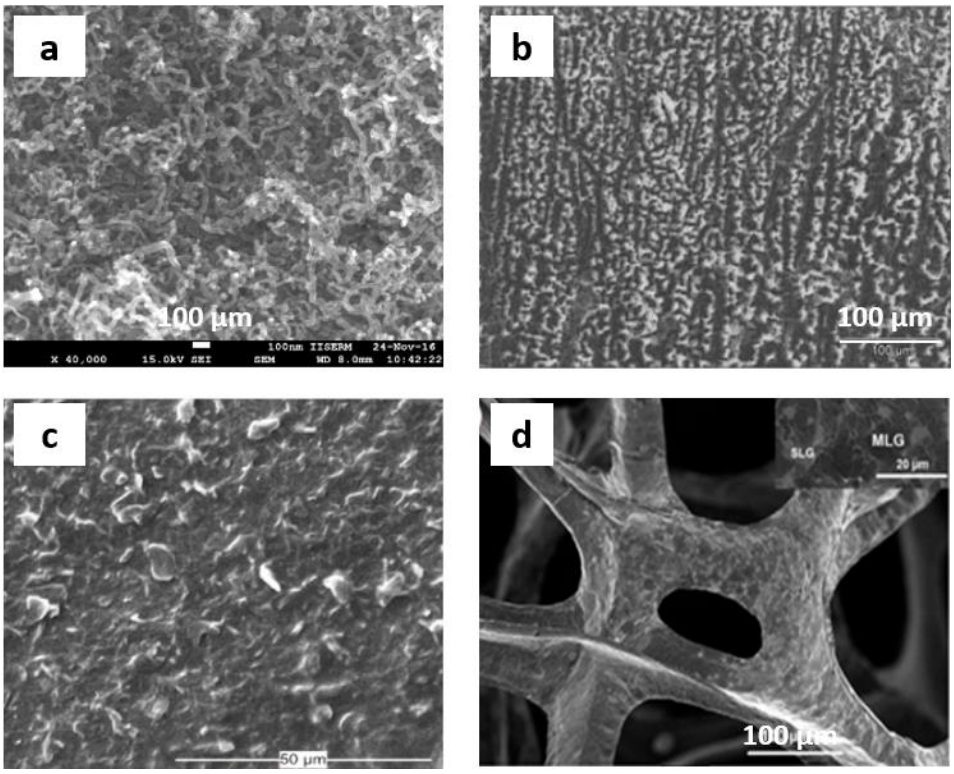

Figure 10. Comparison of scanning electron microscope images of morphological structures of various coatings a) G/CNT coated on copper [38], b) Dip coated G/GO on copper [39], c) Porous graphene on Indium Tin Oxide surface [37], d) 3-D foam like graphene on nickel [12]

Ganesan et al. [38] coated graphene/carbon nanotubes (G/CNTs) heterostructures (Fig. 10a) on the copper substrates and enhanced CHF by 40% and HTC by 155%. They found that factors such as increased nucleation sites, capillary effect, lateral heat transfer through graphene intermediate layer and improved bubble dynamics were responsible for enhancing the performance. Coating methods such as chemical vapor deposition and dip coating were developed by Jaikumar et al. [39] to deposit graphene and graphene oxide coatings in the nanoscale and microscale, respectively. Maximum CHF of 192 W/cm² was achieved for the 5 minutes dip-coated sample (Fig. 10b), and the increment in roughness and contact angle hysteresis were the responsible mechanisms for performance

improvement. In comparison, the hysteresis in contact angle was identified as the driving mechanism in the case of nanoscale coatings.

Typically, coatings are created on the boiling surfaces to accomplish primary functions such as increment in porosity, wickability, and thermal conductivity, which ultimately assist in enhancing the pool boiling performance. It is observed and concluded from the literature review that the morphologies achieved with different coating techniques have been uniform throughout the coating. This uniform morphological coating creates a uniform porous network resulting in lower CHF and HTC values. This is postulated due to the formation of the uniform porous network; similar-sized vapor bubbles are formed, leading to early vapor layer formation by agglomerating in the horizontal direction, thus covering an entire boiling surface with an insulating vapor layer. This can be eliminated by creating a non-uniform porous network.

2.4 Research needs

As noted from the literature review, carbon-based nanomaterials can significantly impact the CHF and overall pool boiling performance due to their higher thermal properties. Nevertheless, these enhancements introduce new challenges such as weak adhesion with the substrate, lack of durability and sustainability, and complexity related to liquid-vapor interaction and inefficient vapor removal at the boiling surface, which can lead to lower CHF and/or increased wall superheats due to early coalescence. This also translates to lower efficiency of the boiling surfaces during boiling. Carbon-based nanomaterials employed to date have resulted in CHFs of less than 230 W/cm^2, and the HTCs have been lower than 120 $kW/m^2\text{-}°C$ on the plain copper surfaces using distilled water as a working fluid at atmospheric pressure. Higher operational range and safety are

essential for the real-world applications of carbon-based coatings. Thus, a research gap is recognized where along with enhancement in CHF and HTC, the durability of the boiling surfaces and coatings is desirable. This research work aims to achieve this by introducing a non-uniform hierarchical porous network with unique morphological structures that can assist in delaying the vapor layer formation. Various deposition and powder metallurgy techniques are explored in this work to develop these morphological structures. This work also aims at improving the sustainability of the electrodeposited coatings and is expected to have a direct impact on increasing the practicability of the carbon nanomaterials-based coatings and ensuring safe operations and wide operational ranges for various industrial applications, including electronics cooling, heat exchangers, reboilers, distillation columns, desalination, and refrigeration industries. The mechanisms introduced in this work can also be implemented to improve the performance characteristics based on specific targeted applications such as lithium-ion batteries, corrosion protection, anti-wetting, and anti-fogging applications.

Chapter 3

3. Approach

3.1.1 Overview:

One of the significant challenges in enhancement using various coatings is the ease of formation and sustainability of the coatings. Pool boiling is a technique that involves vigorous motion of bubbles on the boiling surface and causes damage to the coating. If the bond strength of the coating is not high, it can significantly impede the heat transfer performance and makes the system highly erratic and highly unstable. The damage on the coating is higher if the substrate bond strength is less and if the adhesive forces are weak. These weak forces also reflect in the reduction of pool boiling performance and increase in wall superheat temperature owing to the removal of the coating material from the substrate. In some cases, the vapor layer formation on the boiling surface can result in a thermal meltdown of the system. To overcome these challenges and to enhance the pool boiling performance, various coating preparation parameters and methods have been considered in this work. With better control on surface properties such as porosity and wickability, the CHF and HTC of the coatings are expected to increase to very high values. This research work is divided into four main parts: the first part focuses on the development of graphene nanoplatelets/copper (GNP/Cu) composite coatings using the electrodeposition technique to enhance the pool boiling performance. The second part focuses on improving bond strength and adhesion of the electrodeposited coatings on boiling surfaces. This improvement is also expected to enhance the durability and pool boiling performance of the coatings. This is tested using copper-based microporous coatings. The third part involves the formation of GNP-copper based composite coatings

using sintering technique. The performance of sintered coatings is further enhanced by using a powder metallurgy-based ball milling technique which allows the formation of a homogeneous mixture of GNP and copper particles. By optimizing the process parameters during ball milling, the draping of GNP on individual copper particles was yielded. Finally, the fourth part of this work focuses on further enhancing sintered GNP-Cu coatings via the implementation of salt templated sintering. Salt templated sintering is performed to gain better control on porosity and pore size of the sintered coatings and to impart a wide range of pore diameter-based networks and enhance the pool boiling performance in terms of both CHF and HTC.

An in-depth morphological study was conducted for each of the coated surfaces before performing the pool boiling studies. Some of the characterization techniques included Goniometer for contact angle testing, scanning electron microscopy (SEM), transmission electron microscopy (TEM), X-ray diffraction (XRD), Raman Spectroscopy, Fourier transform infrared (FTIR) spectroscopy, and Thermogravimetric analysis (TGA).

3.1.2 Test section:

Plain copper test surfaces made of copper alloy 101 were used in this study. Boiling surfaces consisted of a 17 mm x 17 mm x 9 mm surface with a 10-mm deep rectangular base to accommodate the thermocouples used for estimating surface temperature and heat flux. The thermocouple holes were drilled to reach the center of the rectangular base. As shown in Figure 11, the distance between the two successive holes on a rectangular base is 3 mm (Δx), while the distance between the hole near the boiling surface and the top of the test surface is 1.5 mm. (x_1). To read the three temperatures, K-type T_1, T_2, T_3, thermocouples were inserted into the holes.

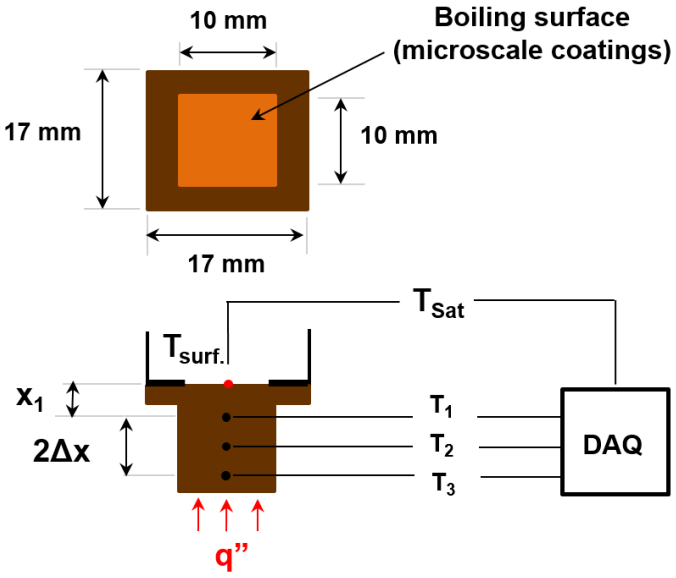

Figure 11. Top view and front view of the test/boiling surface along with data acquisition

Heat flux (q'') dissipated by the boiling surface was calculated using steady-state 1-D conduction equation:

$$q'' = -k_{Cu}\frac{dT}{dx} \tag{6}$$

Where k_{Cu} is the thermal conductivity of copper and the temperature gradient dT/dx was calculated using the three-point backward Taylor's series approximation

$$\frac{dT}{dx} = \frac{3T_1 - 4T_2 + T_3}{2\Delta x} \tag{7}$$

The surface temperature of the copper test chip or wall temperature was obtained by using Equations 6 and 7, and is given by,

$$T_{wall} = T_1 - q''\left(\frac{x_1}{k_{Cu}}\right) \tag{8}$$

Temperatures T_1, T_2, T_3 are the measured temperatures of the copper test chip indicating top, middle, and bottom temperatures, respectively.

And heat transfer coefficient (h) is calculated using the following Equation (9).

$$h = \frac{q''}{T_{wall} - T_{sat}} \quad (9)$$

Here, T_{wall} is the boiling surface temperature or wall temperature of the copper test chip and T_{sat} is the saturation temperature of the liquid.

3.1.3 Experimental setup:

A schematic of the experimental setup used for the pool boiling tests of the test chips is shown in Fig. 12. The test setup included a water bath, an instrumented test chip/ boiling surface, and a heater. The test chip was placed in the ceramic chip holder with slots to insert the thermocouples. Only the 10 mm x 10 mm area of the test chip surface was exposed to the boiling and the remaining area was covered with Kapton® tape, which acts as an insulation. Above the test chip, a quartz glass water bath, rectangular in cross-section, with dimensions 14 mm x 14 mm x 38 mm, was placed. To seal the contacting surfaces at the bottom and the top, a rubber gasket was used.

Two stainless steel socket head cap screws were used to hold the middle garolite plate and the top aluminum plate. In the top aluminum plate, an auxiliary cartridge-type heater (60-V DC, 200W) of circular cross-section was fitted along with a small circular hole to insert the saturation thermocouple probe. Four cartridge type heaters of 120-VDC, 200W capacity were inserted into a copper heater block which was then placed on the ceramic block below the test chip. The heater block fits snugly into the groove on the

bottom of the ceramic chip holder. A Grafoil sheet was placed above the heater to minimize the air gap between the chip and the heater. The aluminum block is placed below the ceramic block, which is supported by four compression springs to establish the correct contact between the heater block and the test chip. The adjustable platform of rack and pinion type motion is also used to maintain the proper contact between the copper heater surface and the copper test chip. This also ensured only 1-D steady-state conduction from the heat source to the test chip [34].

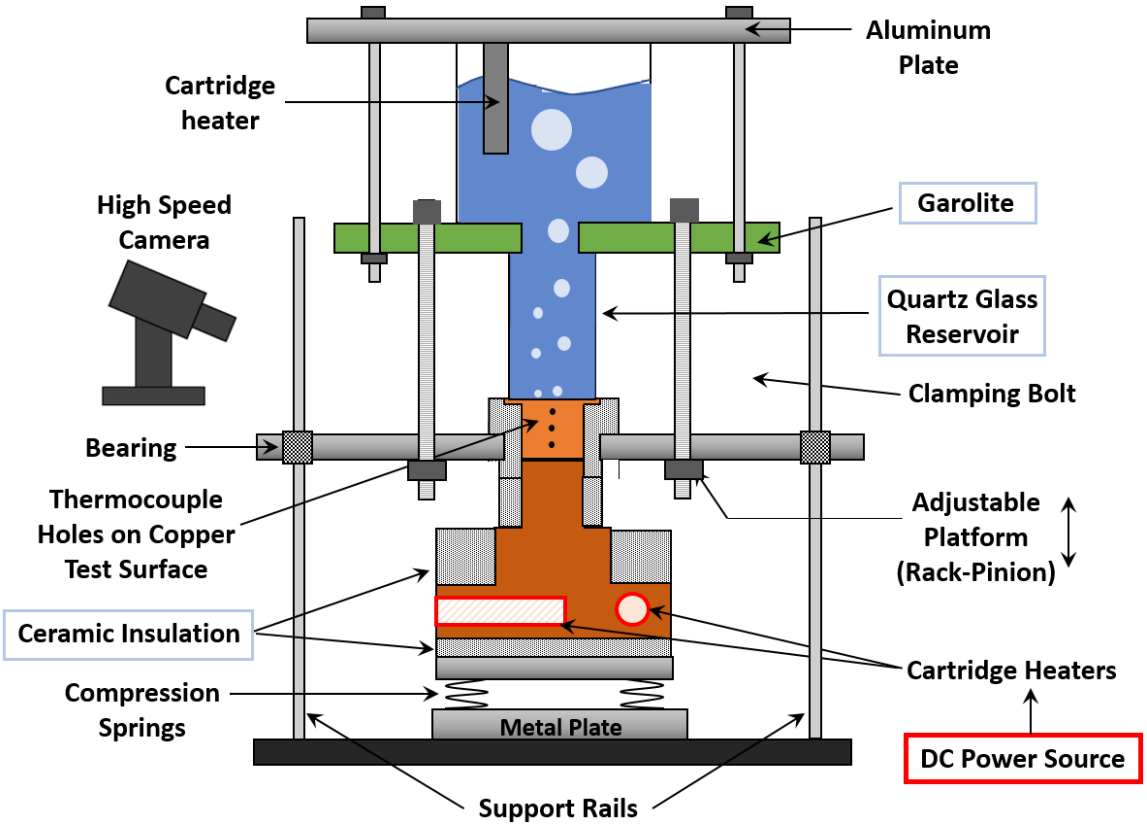

Figure 12. Pool boiling setup

3.1.4 Uncertainty analysis:

During the experiment, a certain amount of error occurs in measuring the values. The two main errors are precision error and bias error. Bias errors are the difference between the expected measurement value and the true measurement value. So, bias errors are the errors due to calibration, while precision errors are due to the variations in measurements. And are calculated using a statistical analysis of the data. A standard equation to calculate the uncertainty is given as follow:

$$U_p = \sqrt{\sum_{i=1}^{n} \left(\frac{\partial p}{\partial \sigma_i} * U_{\sigma i} \right)^2} \quad (10)$$

where, U_p is the uncertainty of any parameter p, and $U_{\sigma i}$ is the uncertainty of any measured parameter σ_i. The uncertainty in the heat flux and heat transfer coefficient can thus be expressed by equations 11 and 12, respectively. The detailed derivations of these equations are provided in the appendix section 7.1 Uncertainty in heat flux and 7.3 Uncertainty in heat transfer coefficient:.

$$\frac{U_{q"}}{q"} = \sqrt{\left[\left(\frac{U_{k_{Cu}}}{k_{Cu}} \right)^2 + \left(\frac{3U_{T_1}}{\alpha} \right)^2 + \left(\frac{4U_{T_2}}{\alpha} \right)^2 + \left(\frac{U_{T_3}}{\alpha} \right)^2 + \left(\frac{U_{\Delta x}}{\Delta x} \right)^2 \right]} \quad (11)$$

$$\frac{U_h}{h} = \sqrt{\frac{U_{q"}^2}{q"^2} + \frac{U_{T_w}^2}{\Delta T_{sat}^2} + \frac{U_{T_{sat}}^2}{\Delta T_{sat}^2}} \quad (12)$$

where, $U_{k_{Cu}}$ is the uncertainty in thermal conductivity of copper, U_{T_1}, U_{T_2}, and U_{T_3} are the uncertainty in temperatures T_1, T_2, and T_3, respectively. $U_{\Delta x}$ is the uncertainty in measurement between two thermocouple holes, $U_{q"}$, U_{T_w}, and $U_{T_{sat}}$ are the uncertainties in heat flux, wall temperature and saturated temperatures, respectively.

3.1.4.1 Biased Uncertainty

The biased uncertainty for thermocouples was measured by calibrating the thermocouples in a hot cell by varying the temperature of the hot cell from 60°C to 250°C. For each steady-state value of temperature, 50 data points were recorded for three thermocouples (T_1, T_2, and T_3). The true temperature value of the hot cell was recorded during each step and the standard deviation for each thermocouple was calculated using the true value for all steady-state conditions. This average standard deviation value was multiplied by two to estimate the biased error for each thermocouple to get a 95% confidence interval.

The biased uncertainty for thermal conductivity of copper 101 alloy was 9 W/m-K, which was provided by the material provider "Online Metals". The biased uncertainty for the distance between two successive thermocouple holes (Δx), and the distance between the top thermocouple and the boiling surface (x_1) was 0.0001 mm. This value was taken from the least count of the Vernier caliper which was used to measure the respective distances. The absolute value and percentage of biased uncertainties for all the variables are shown in Table 1. The error associated with thermocouples (T_1, T_2, and T_3) differs depending on the actual temperature of the hot cell.

Table 1: Biased Uncertainty

Parameters	Value	Units	Biased Uncertainty	% Uncertainty
k_{Cu}	391	W/m-K	9.00	2%
Δx	3.00E-03	m	0.001	3%
x_1	1.50E-03	m	0.001	6%
T_1	Varies	°C	0.16	Varies
T_2	Varies	°C	0.40	Varies
T_3	Varies	°C	0.25	Varies

3.1.4.2 Precision Uncertainty

An approach similar to the calculation of biased uncertainty was followed to calculate the precision uncertainty of three thermocouples. Instead of using the true temperature value at a given heat flux, the mean temperature value of 50 data points was used for calculating the standard deviation. This method was implemented for all thermocouples and for each heat flux value. Precision error in each thermocouple after calibration and statistical calculation was ± 0.1°C. The precision errors related to the thermal conductivity of copper and distances between thermocouple holes (Δx *and* x_1) were considered zero since these parameters do not alter by varying the heat flux during the experimental study. The total uncertainty for all the parameters was calculated by taking the square root of the squares of biased and precision uncertainties.

Figure 13 below shows the % uncertainties for heat flux and heat transfer coefficients for one of the best-performing coated surfaces. Similar percent uncertainties were observed for the rest of the surfaces.

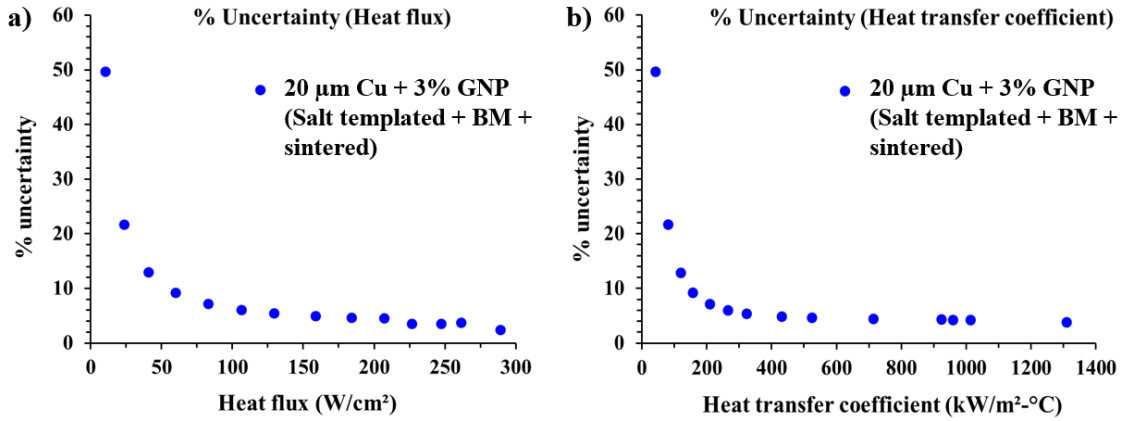

Figure 13. Uncertainty in heat flux and heat transfer coefficient for 20 µm Cu- 3% GNP ball milled + salt templated sintered surface

Chapter 4

4. Results and discussions

The first two sections (4.1 and 4.2) of the results and discussions chapter focus on boiling enhancements via electrodeposition technique, while sections 4.3 and 4.4 focus on boiling enhancements using powder metallurgy and sintering-based techniques.

4.1 Enhancement through Improved Wettability via Graphene Nanoplatelets/Copper (GNP/Cu) Composite Coatings:

4.1.1 Formation of GNP/Cu composites via electrochemical deposition:

As discussed in the literature study, one of the promising and effective ways to enhance the pool boiling heat transfer performance is by improving the boiling surface's wettability and thermal conductivity. Electrodeposition is one of the easier techniques to achieve microporous, robust, and sustainable coatings with higher bond strength. Preliminary work was performed to create only graphene-based coatings using chemical vapor deposition and dip coating techniques but did not increase the performance due to lesser porous structure formation. Thus, a combination of copper and GNP was deposited on the boiling surfaces to develop composite coatings. Copper particles deposited during electrodeposition control the morphology of the coatings at the microscale, while GNP control and influence the wettability and thermal conductivity of the coatings. A two-step electrodeposition technique was employed to deposit copper reported earlier by the authors [41]. Plain copper surfaces were cleaned with Isopropyl Alcohol (IPA) and distilled water to remove any impurities if present on the test chip. Test chip with the central 10mm x 10mm area is then marked, and the area outside this region is covered with electrical insulation tape. This is performed to avoid any deposition occurring in the region outside

the central test area. The copper test surface acted as the working electrode with a copper block as the counter electrode to create the electrochemical cell. A Polytetrafluoroethylene (PTFE) holder was designed to maintain the working and counter electrode parallel to each other. The distance of 3 mm between the cathode and the anode is maintained for all the electrodeposition processes. The working area was delineated with Kapton® tape. Once both working and counter electrodes are placed in the holder and connected to the power source, the whole structure is placed in a solution as shown in Fig. 14. Electrolytic bath consisted of 5.85 gm $CuSO_4$ (0.8M), 3.14 mL H_2SO_4 (1.5M), 40mL distilled water, and GNP aggregates with 0.25%, 0.5%, 1.0%, 1.5%, 2%, and 2.5% weight/volume. The chemical reaction of $CuSO_4$ and H_2SO_4 is exothermic, and therefore water was added in two intervals, 20 mL before and 20 mL after adding H_2SO_4. The electrolyte solution was then sonicated using (Q Sonica, 125W, 20 kHz) ultra sonicator for 45 minutes.

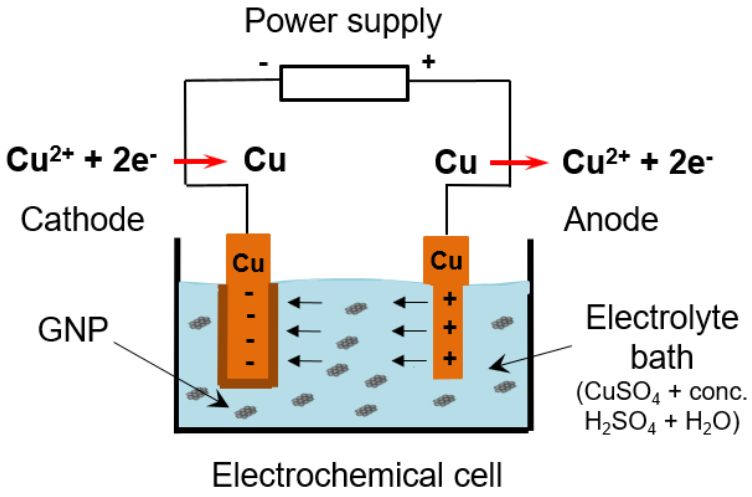

Figure 14. Schematic representation of experimental setup of electrochemical cell

A Galvanostatic method of electrodeposition was used due to its simplicity and control on current density and time (Figure 15). Step 1 of electrodeposition processes involved applying a current density of 400 mA/cm² for 15 sec. that caused the evolution of

hydrogen bubbles, which served as a template for the copper particles to get deposited around the bubbles forming a porous network. This was followed by the application of a lower current density of 40 mA/cm² for 2500 sec that strengthened the bonding between the deposited GNP/Cu composite and substrate copper (Figure 15). Cupric Sulfate Pentahydrate ($CuSO_4.5H_2O$) was purchased from EMD Millipore Chemicals and Sulphuric Acid (H_2SO_4) manufactured by Avantor™ Performance Materials, Inc. was used. Sub-micron particles of GNP aggregates having a surface area of 500 m²/g were purchased from Alfa Aesar. A standard tape test (ASTM 3359) was performed on all the electrodeposited surfaces to evaluate the adhesion of GNP/Cu coatings on the copper test substrate.

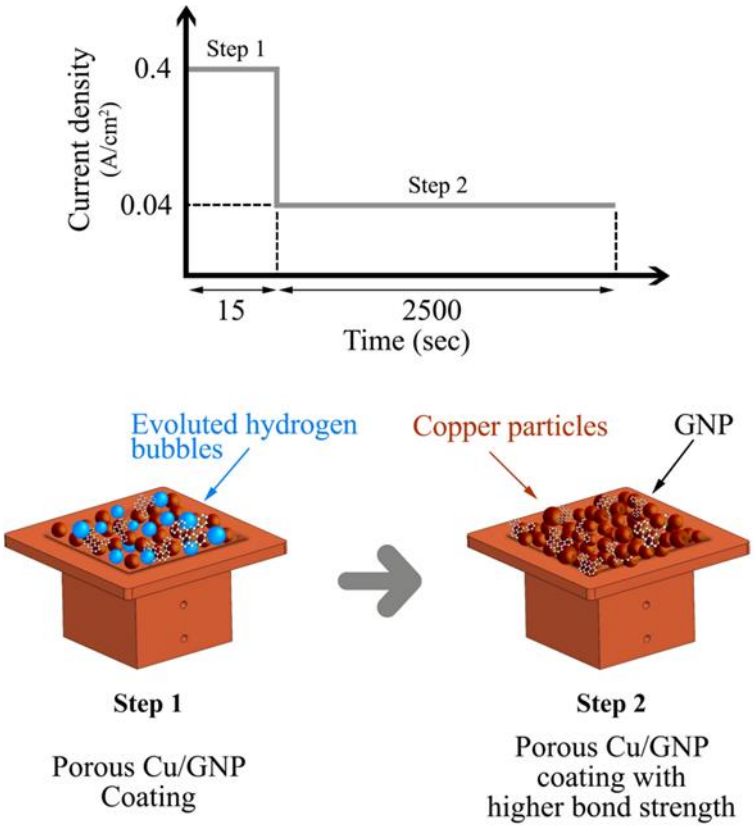

Figure 15. Schematic representing the two-step electrodeposition process showing the evolution of hydrogen bubbles and deposition of coating with high bond strength

4.1.1.2 Surface characterization techniques:

Surface morphology of GNP/Cu composites were analysed using a Field Emission Scanning Electron Microscope, and the chemical composition was analysed using Raman Spectroscope and X-Ray Diffractometer (XRD). Static wettability and dynamic wicking of GNP/Cu coatings were measured for all the test surfaces using a VCA Optima Goniometer. For dynamic wicking, a distilled water droplet of 2 µL was steadily brought into contact with the electrodeposited test surfaces using a static sessile drop method, and liquid propagation was recorded using a high-speed camera. The measurements were conducted on a minimum of two different locations on the electrodeposited surface. A Photron Fastcam high-speed camera was used for capturing the bubble images at a frame rate of 2000 fps, and a Photron Fastcam Viewer (PFV) was used to observe the propagation of bubbles at each frame.

4.1.1.2.1 Scanning electron microscope analysis of electrodeposited GNP/Cu surfaces-

The two-step electrodeposition method with varying concentrations of GNP with copper yielded unique morphological structures on the coated surfaces. Figures 16a to 16d summarize the scanning electron microscope images of GNP/Cu 0.5, 1, 2, and 2.5% GNP/Cu composite coatings, respectively. 0.5% GNP/Cu coatings seen in 3a demonstrated rough spherical structures typically observed with copper-based coatings. With an increase in GNP concentration from 1 to 2.5% GNP, hierarchical porous structures were observed. 1% GNP coating is shown in Fig. 16b exhibits a heterogeneous morphology showing flattened regions and regions with stacked spheres whereas with 2% complex porous structures with pore sizes ranging from 0.6 µm to 20 µm. However, for 2.5% GNP, the observed pore sizes were between 2 µm to 10 µm, which can be attributed to the deposition

of excess GNP that were filling in the larger pores. The coated surfaces were also examined at 70º stage tilt to gain an insight on the vertical features of the surfaces for 1% and 2% GNP test surfaces seen in Figures 16e and 16f, respectively. With a GNP concentration increase from 1 to 2% GNP, the height of porous structures increased from 20-50 µm to 60-80 µm.

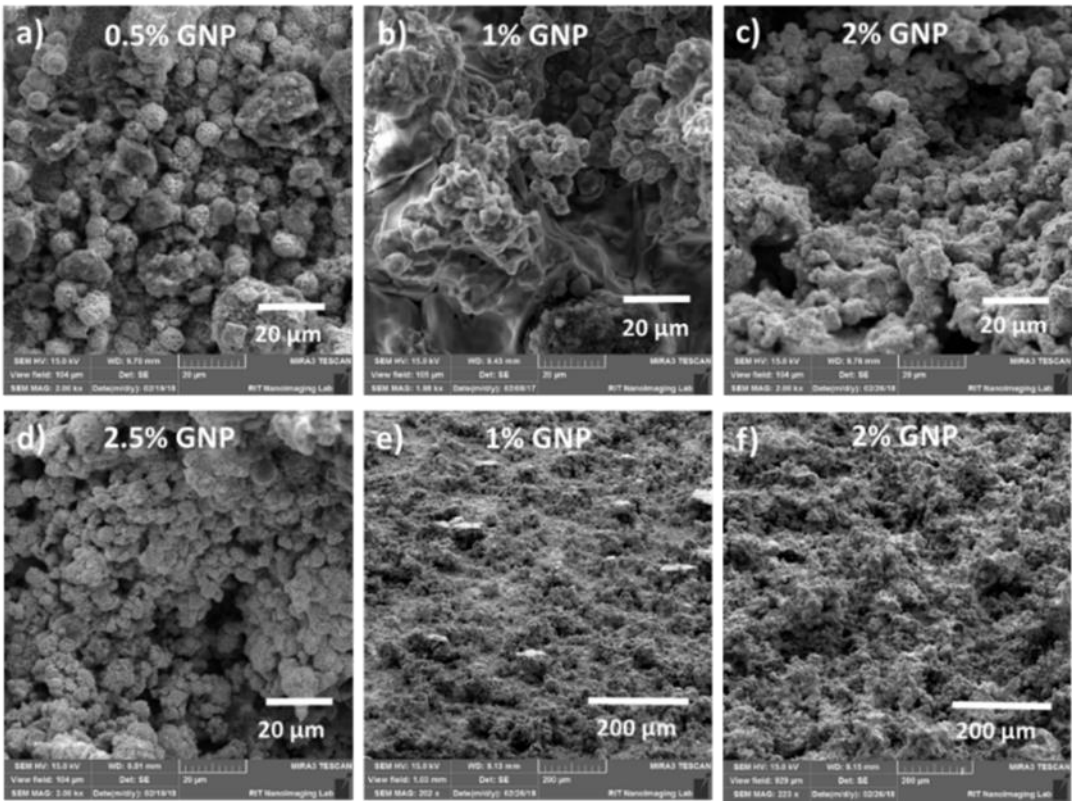

Figure 16. Scanning electron microscope (SEM) images at 2kX magnification of GNP/Cu composites containing a) 0.5% GNP, b) 1% GNP, c) 2% GNP, d) 2.5% GNP, and 70° tilted images at 200X of composites containing e) 1% GNP, and f) 2% GNP

Figure 17 shows 70° stage tilted SEM and energy dispersive spectroscopy (EDS) images comparing the different coatings and their corresponding carbon and copper mapping. EDS analysis shows the presence of carbon on all GNP-based coatings. Additional pores are also observed with increment in GNP concentration.

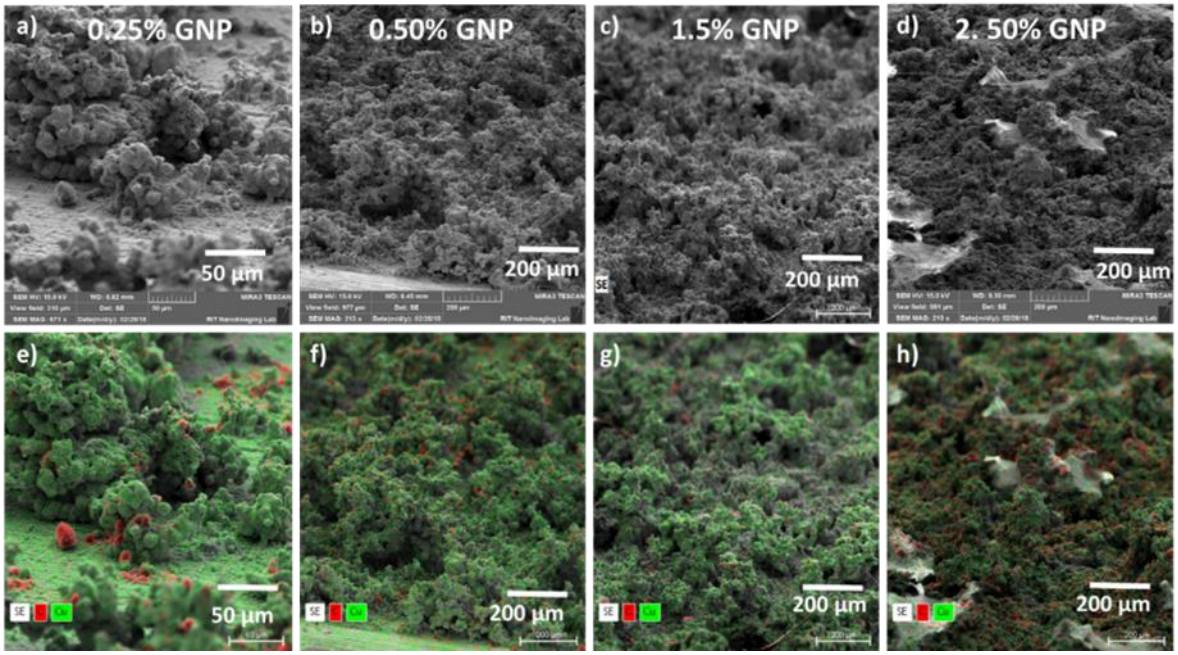

Figure 17. Stage tilted SEM images and corresponding EDS mapping for GNP/Cu electrodeposited surfaces at GNP concentration of a), e) 0.25%, b), f), and 0.5 % GNP, c), g) 1.5%, and d), h) 2.5% GNP

4.1.1.2.2 X-ray diffraction and Raman spectroscopy analysis of GNP/Cu coatings:

X-ray diffraction is a technique used for determining the atomic and molecular structure of a crystal in which crystalline atoms cause a beam of X-rays to diffract in specific directions. When X-rays are incident on the sample, the incident beam gets separated into a transmitted beam and diffracted beam. The diffraction pattern is recorded in terms of 2θ angle that indicates the crystalline phase of the material. The crystalline phases of GNP/Cu electrodeposited coatings were investigated using a Rigaku DMAZ-IIB X-Ray Diffractometer (XRD) with Cu Kα radiation; wavelength 1.5418 Å. The spectra were recorded for 2θ ranges between 5° and 75° at a rate of 3°/min rate. The step size was 0.02° with an x-ray power of 40 kV and 35 mA. This range is expected to capture peaks

from carbon and the underlying copper substrate. The location of characteristic peaks determines the presence of elements on the surface.

X-ray diffraction 2θ reflection peaks between 6° to 10° correspond to graphene. The peaks detected at 47° to 54° correspond to the crystalline structure of copper. Figure 18 shows the comparison of the XRD plot for different test surfaces with intensity on the y-axis and 2θ reflection peaks on the x-axis. The peaks confirm the presence of graphene along with copper.

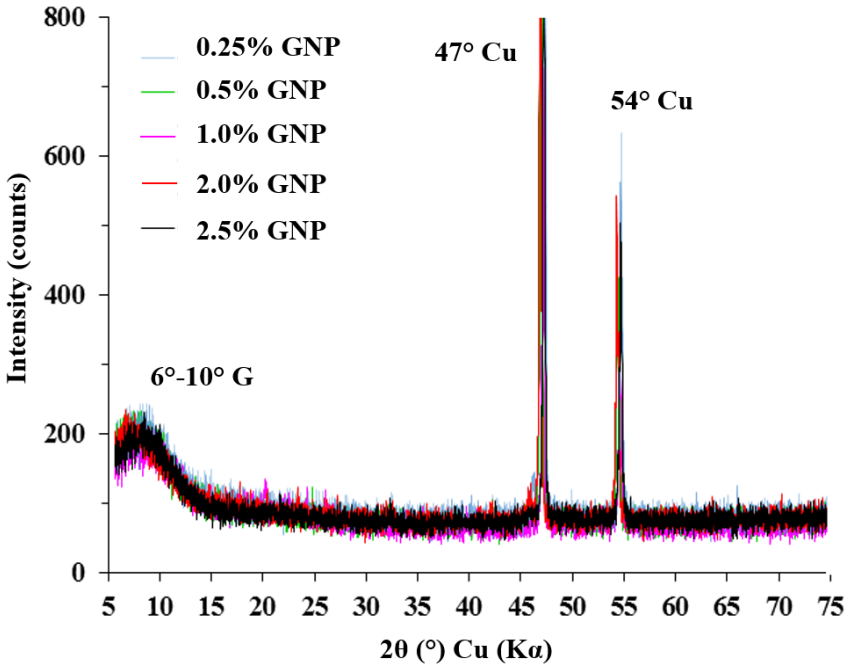

Figure 18. Comparison of x-ray diffraction (XRD) spectroscopy analysis of GNP/Cu electrodeposited test surfaces

4.1.1.2.3 Energy dispersive spectroscopy analysis of GNP/Cu coatings:

Intuitively, an increase in the concentration of GNP in the electrolyte solution will deposit more graphene on the test surface during electrodeposition. This was confirmed by energy-dispersive x-ray spectroscopy (EDS) analysis shown in Fig. 19 that exhibits a set

of peaks for carbon, copper and oxygen based on their electromagnetic spectrum pertaining to their unique atomic structures. On the energy spectrum, the peaks at approximately 0.3 keV, 0.5 keV, and 0.9 keV correspond to the presence of carbon, oxygen, and copper, respectively. The copper and carbon mapping for 2% GNP surface is shown on its analogous SEM image in Fig. 20. The energy shows the increment in carbon intensity for the samples with higher percentages of GNP 0.25% GNP to 2% GNP. However, the 2.5% GNP test surface demonstrated a lower intensity peak than the 2% GNP test surface. It was due to the addition of excessive GNP that aggregated in the solution with the electrolyte causing and producing a menial coating with less graphene deposition.

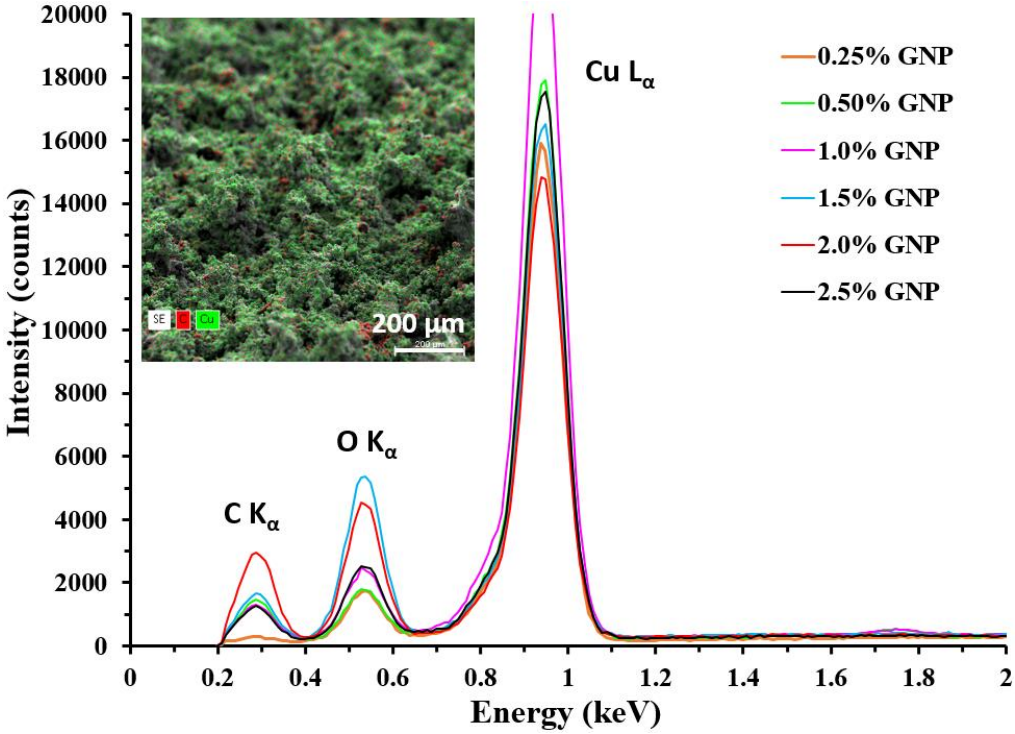

Figure 19. a) Energy dispersive x-ray spectroscopy (EDS) analysis, and b) Raman spectra of GNP/Cu electrodeposited test surfaces

4.1.1.2.3 Raman spectroscopy analysis of GNP/Cu coatings:

Raman spectroscopy is a powerful tool that can be used for both qualitative and quantitative applications in which scattering of light is used to measure the vibrational energy modes of samples. Raman data provides a unique chemical fingerprint of the material and the peak intensity provided by Raman spectroscopy is proportional with the concentration and is helpful for quantification. In this study, Raman spectroscopy was employed to quantify the number of graphene layers deposited on the test surfaces with respect to varying concentrations of GNP in the sample. Raman spectra on Fig. 20 show G, D, and 2D peaks, which correspond to graphene and graphene-based derivatives. G and D peaks correlate to in-plane vibrations of sp^2-hybridized carbon atoms and degree of disorder of sp^3-hybridized carbon structure, respectively, for graphene [42]. While the 2D peak is the second-order D-peak and is typically the connotation of D peak. The ratio of intensities of G and 2D peaks is used to determine the number of graphene layers deposited on the surface [43].

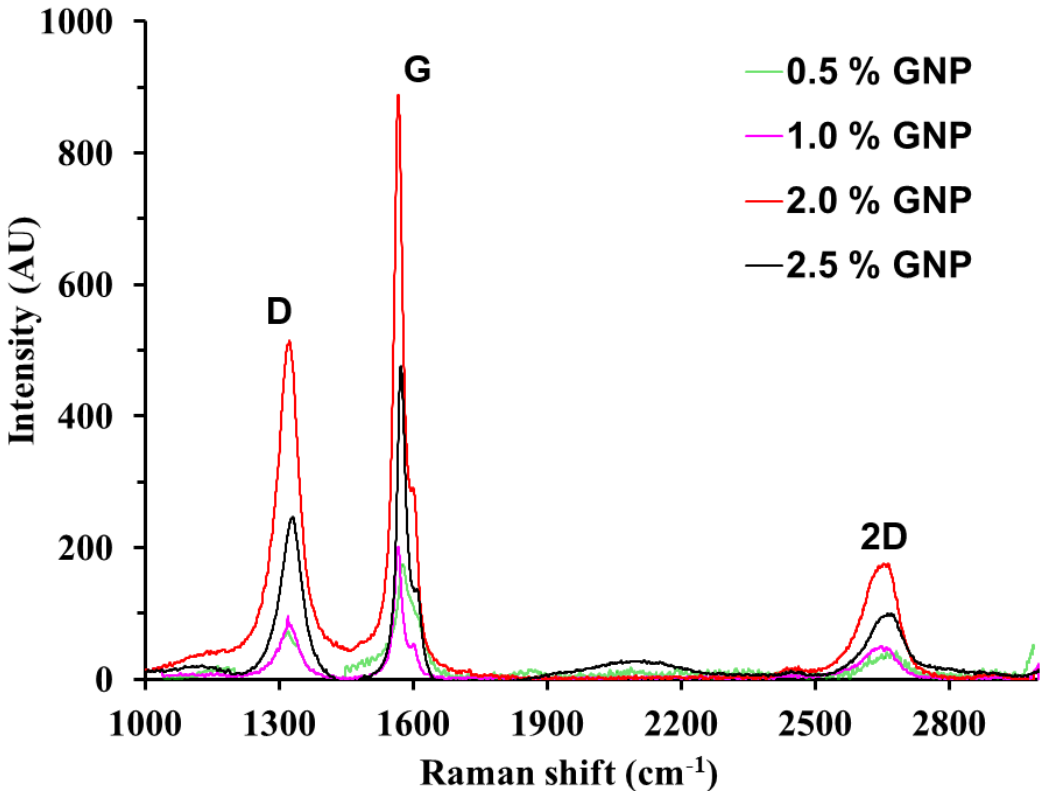

Figure 20. Raman spectra of GNP/Cu electrodeposited test surfaces

For all the absorption peaks at D, G, and 2D, a Raman shift was observed due to the application of a higher wavelength of Laser (λ = 632.8 nm instead of λ = 514 nm), which has also been reported in the literature [44]. For all the GNP/Cu samples, the absorption peaks for D and G bands were seen at ~1340 cm^{-1} and ~1580 $cm^{-1,}$ respectively and the intensities varied with respect to the varying concentrations of GNP. Table 2 summarizes the ratios of I_D/I_G that demonstrate the oxidation degree and defects [43], and ratios I_G/I_{2D} that quantify the number of graphene layers in each sample. I_G/I_{2D} ratios greater than 1 confirmed the presence of multilayers of graphene on all the samples.

Table 2. Quantification of layers of graphene through analysis of characteristic D and G peaks obtained using Raman spectroscopy

Test chip	**I_D/I_G (oxidation degree and defects)**	**I_G/I_{2D} (number of layers of graphene)**
0.5% GNP	0.41	~ 3.8
1.0% GNP	0.47	~ 4.01
2.0% GNP	0.58	~ 5.08
2.5% GNP	0.52	~ 4.76

The influence of laser power intensities on the Raman spectra of GNP was also studied at room temperature to establish the relationship between the laser power and GNP peaks. Varying laser power Raman spectroscopy analysis was performed on a 2.5% GNP-Cu sample. The 100% laser intensity in Fig. 21 represents the 0.5 mW power of the He-Ne laser source (λ = 632.8 nm). Changes in laser intensity induce the changes in temperature and thus, a linear shift of D and G peaks is observed. When the laser beam is incident on the sample during Raman spectroscopy, GNP absorbs a significant amount of laser and visible light and absorbed energy converts into heat, causing the shift in D and G peaks due to the thermal expansion and phonon dispersion phenomena. Similar peak shifts are also observed in the literature for Raman spectroscopy of graphene with defects [45].

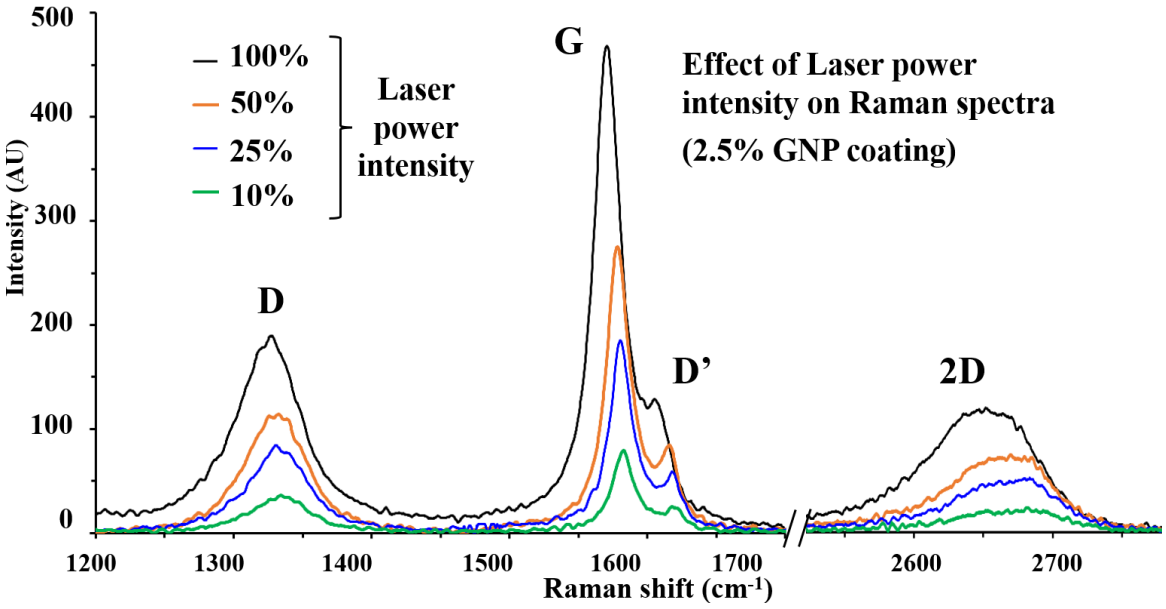

Figure 21. Influence of laser power intensity on Raman peaks of 2.5% GNP/Cu test surfaces

Figure 22a shows the effect of laser power on the intensities of G, D, and 2D peaks. During the laser power Raman analysis, 2.5% GNP-Cu sample was exposed to four different laser powers 0.5, 0.25, 0.125, and 0.05 mW representing the 100%, 50%, 25%, and 10% power intensities of the laser, respectively. A linear reduction in peak intensity was observed for all G, D, and 2D peaks and is shown in Fig. 22a. Figure 22b shows the position of G band as a function of laser power. The defects on the graphene sheets of GNP make the sample susceptible to influence the intensity of the incident laser. By changing the laser power during the Raman study, changes in temperature cause changes in peak positions of the Raman spectra. As seen from Fig. 22b, as the temperature increases with an increase in laser power intensity, a linear shift of G-peak position is observed due to the combination of thermal expansion and phonon coupling [22]. Compared to pristine graphene, this shift of position is higher in the presence of GNP due to the presence of

functional groups (such as oxygen and hydroxyl) on graphene sheets [22]. However, the shift is minimal and is within ~10 cm^{-1} confirming a small defect density on GNP.

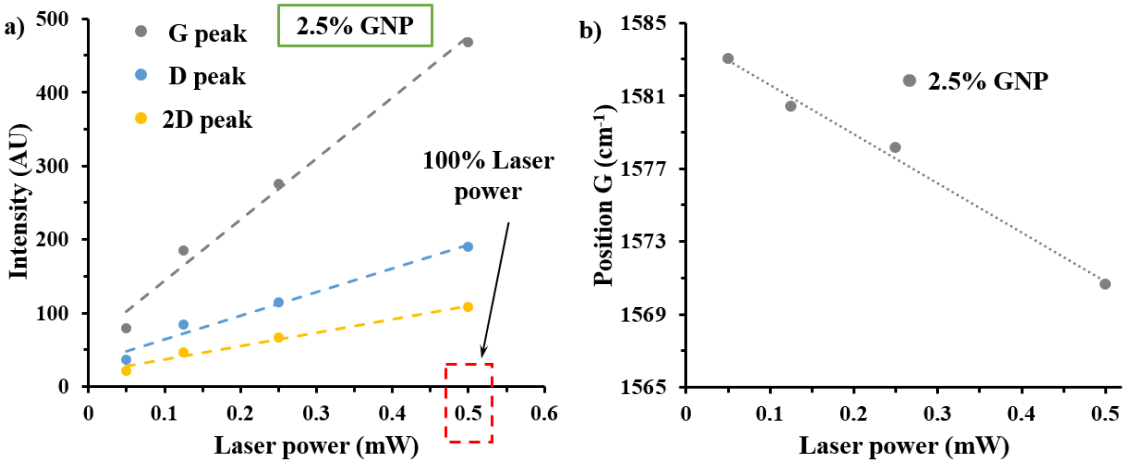

Figure 22. a) Plot showing the G, D, and 2D GNP peaks as a function of laser power b) Shift in G peak position as a function of laser power (λ=632.8nm)

4.1.1.3 Surface wetting characteristics and correlation with the morphology of electrodeposited GNP/Cu surfaces-

All the GNP/Cu electrodeposited surfaces were found to be superhydrophilic in nature, indicating the 0° contact angle for all the coatings. Owing to very high wicking ability of the coatings, it was observed that the water droplet was wicked into the coating as soon as it was dropped on the surface. Thus, to distinguish the wicking rates of each GNP % coating, water spreading behavior for each surface was observed from the top view using a high-speed camera. Figure 23a-c shows the propagation of the water droplet on 2% GNP/Cu test surface at captured at t = 1 ms and 12 ms, respectively. Figure 23d correlates the wickability as the propagation time required for a 2 µL water droplet with an average diameter *D* (1.6 mm) to spread to an average diameter 2*D* of 3.2 mm for varying % GNP/Cu

test surfaces. It is observed that the wicking rate increases with an increase in % GNP and eventually stabilizes for higher % GNP. The highest wicking rate (~145 mm/s) was observed for 2% GNP/Cu with a propagation time of approximately 11.5 ms due to its highly porous morphology compared to the 18 mm/s calculated for a 0.5% GNP surface with a propagation time of roughly 90 ms. Owing to the similar hierarchical microporous structure and deposition of an approximately equal number of graphene layers (as shown in Table 2), a similar propagation time for the droplet was observed for both 2% GNP and 2.5% GNP surface.

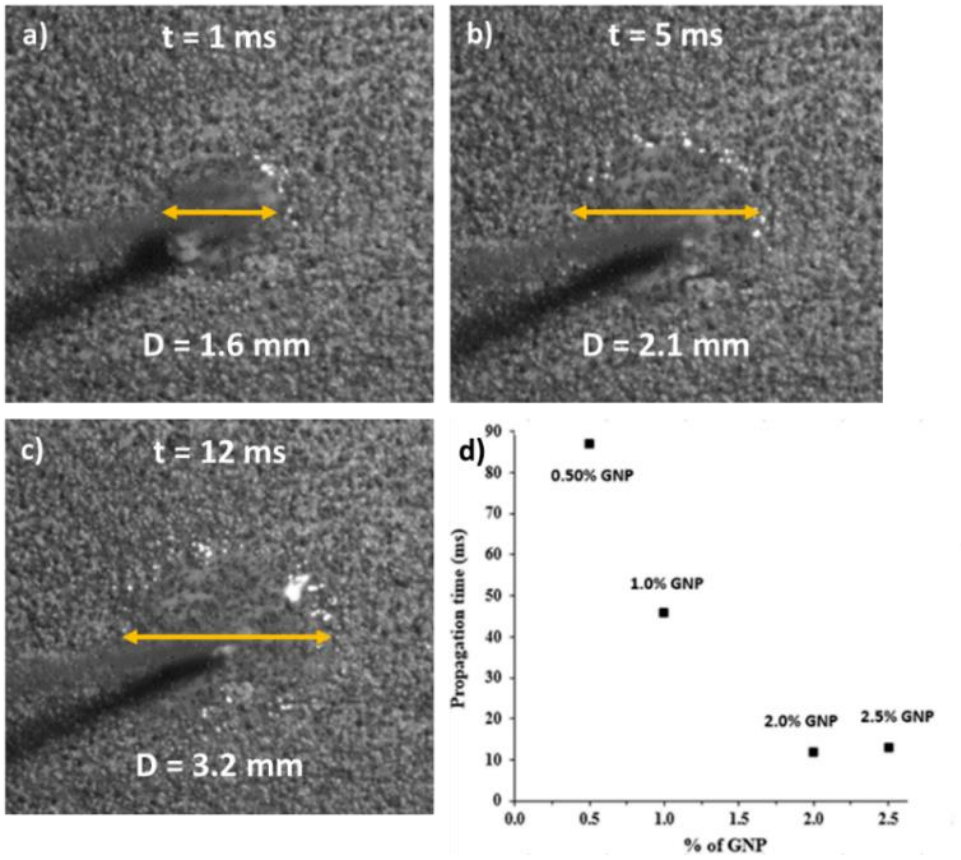

Figure 23. Surface wettability studies of GNP/Cu surfaces a) – c) Frame wise propagation of water droplet on 2%GNP/Cu (weight/volume) at t = 1, 5 and 12 ms, and d) propagation time vs % GNP

4.1.1.4 Pool Boiling studies on GNP/Cu electrodeposited surfaces

Pool boiling performance was quantified by measuring maximum heat dissipated, also known as the critical heat flux (CHF), heat transfer coefficient (HTC) and wall superheat on the water on GNP/Cu test surfaces. A higher heat flux with moderate wall superheat in concurrence with liquid boiling is desirable for engineering applications requiring larger heat transfer in compact spaces. The baseline values for CHF around 125 W/cm² and an HTC of 53 kW/m²-°C were obtained for plain copper surfaces**.** Figure 24a represents the plot for the heat flux values vs. the wall superheat or the temperature difference between the boiling surface (T_w) and saturated water (T_{sat}) obtained for various % GNP/Cu surfaces. Nucleate boiling is the primary regime of interest of this study, and therefore, the experiments were terminated when the CHF was reached. Free convection occurs when the surface temperature is slightly higher than the temperature of the surrounding saturated water. In this regime, natural convection currents circulate the superheated water. As the circulated superheated water reached the free water surface, evaporation takes place. Further increase in surface temperature results in generation of vapor bubbles at various nucleation sites on the surface. The bubbles detach, ascent and condense before spanning to the free water surface [46].

The pool boiling performance plot shows an overall increase in critical heat flux with an increased concentration of GNP on the surfaces. A 2% GNP surface yielded the highest CHF of 286 W/cm² at a wall superheat of 14.1°C, and compared to a plain copper surface; it yielded ~130 % increment in CHF. In a typical boiling heat transfer system, the wall superheats increase with increment in heat flux. However, experimental investigations of pool boiling on enhanced surfaces have been reported to yield higher critical heat fluxes

at lower wall superheats and the phenomena is termed as “boiling inversion” [41], [47], [48]. Here, a shift in pool boiling curve towards the left or lower wall superheats for 0.5, 1, 1.5 and 2% GNP/Cu surfaces is observed. This shift is a function of active nucleation sites available for boiling, and these nucleation sites become active at different wall superheat temperatures for each surface. The underlying mechanism for boiling inversion in porous surfaces is not well understood, but some studies attributed the boiling inversion phenomena to the presence of hierarchical pores that form auxiliary nucleation cavities at higher flux and thermally induced gradients along with the pores due to varying thermal conductivity of the materials [49].

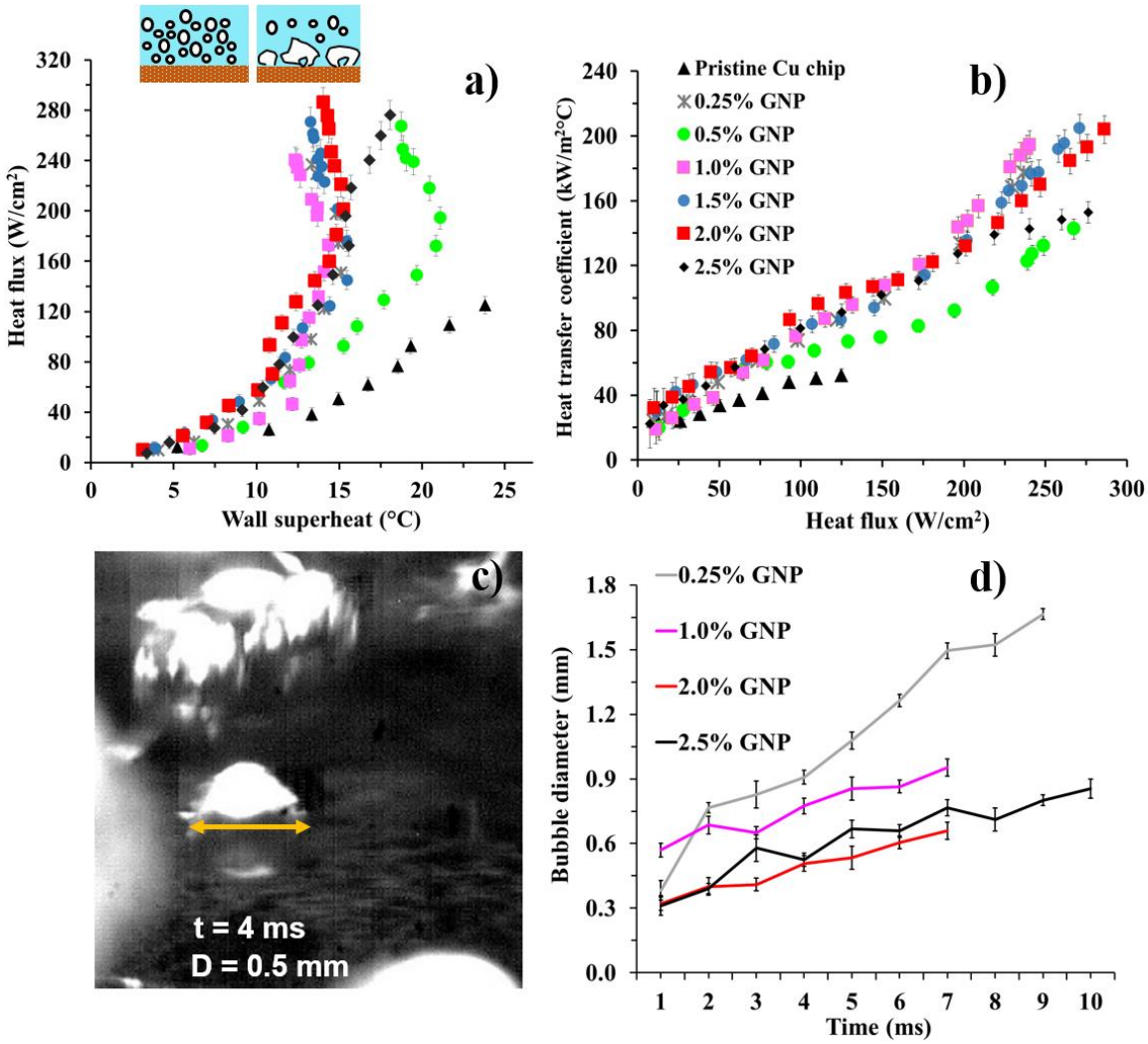

Figure 24. a) Critical Heat Fluxes vs wall superheat depicting pool boiling regimes and performance, b) Heat transfer coefficient vs critical heat fluxes summarizing heat transfer performance, c) progression of bubble diameter during pool boiling on various GNP/Cu surfaces and d, high speed camera image of bubble on 2% GNP/Cu surface

Heat transfer performance of the test surfaces was determined by plotting the calculated values of heat transfer coefficients vs. experimentally found CHF represented in Fig. 24b. 2% GNP surfaces rendered an HTC of 204 kW/m^2 ºC and showed a 290% increment compared to the plain copper surface. Table 3 summarizes the pool boiling (CHF) and heat transfer performance (HTC) for all the test surfaces.

Table 3. Summary of critical heat fluxes and calculated heat transfer coefficients for GNP/Cu test surfaces

Test surface	Critical heat flux (CHF) (W/cm^2)	Heat transfer coefficient (HTC) (kW/m^2-°C)
0.25% GNP	237	177
0.50% GNP	267	142
1.0% GNP	240	194
1.5% GNP	271	201
2.0% GNP	286	204
2.5% GNP	275	150

4.1.1.5 Enhancement mechanism for GNP/Cu electrodeposited surfaces:

As observed from pool boiling plots, addition of GNP during electrodeposition alters various functional properties of the boiling surface. Overall increment in pool boiling performance of these surfaces is attributed to the combined effect of depositing microporous copper structure and deposition of highly thermally conductive (thermal conductivity ~3000 W/m-K) hydrophilic GNP [50]. This combined effect intensified the boiling related properties of the coated surface, and thus yielded the highest pool boiling performance. The presence of hierarchical pores served as nucleation sites for generating additional vapor bubbles that improved the phase change heat transfer efficiency.

4.1.1.5.1 Unique morphological structures and reduced vapor bubble diameters:

Formation of higher peak to valley height difference is one of the important factors in maintaining lower wall superheat temperature. Laser confocal microscope analysis (Figure 25) for all GNP/Cu surfaces except 0.5% GNP shows larger variations in peak to valley heights and coatings with variable morphologies. This resulted in reduced heat transfer coefficient for 0.5% GNP. Larger peak to valley height difference provides thermal

gradient across the coating and increases the effect of microlayer evaporation during boiling.

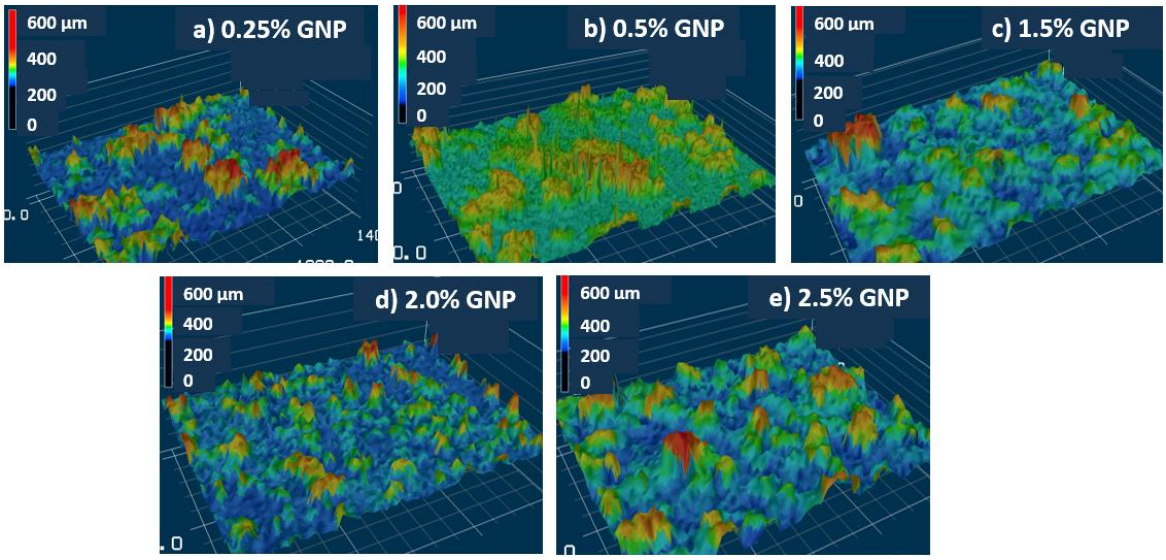

Figure 25. Laser confocal microscope images of the electrodeposited GNP-Cu surfaces

Overall pool boiling performance of the boiling surface is also dependent on the bubble departure diameter and bubble release frequency. A high-speed camera was utilized to record the change in diameter of bubbles from their nucleation till their departure at a heat flux of ~15 W/cm², represented for the 2% GNP test surface in Fig. 26c. A plot of progression of bubble departure diameter as a function of time relative to the pool boiling tests conducted on different test surfaces are summarized with time is shown in Fig. 26d. It was observed that the bubbles departing from all the electrodeposited surfaces were smaller than that on a plain copper test surface because of their microporous matrix that served as nucleation sites resulting in faster growth rates of bubbles with smaller departure diameters. 2% GNP surface produced the smallest bubble departure average diameter of 0.68 mm. Additionally, a reduction in total bubble cycle time – nucleation, growth, and departure of the bubble was observed for the GNP/Cu surfaces compared to the plain

copper surface. The maximum cycle time of 10 ms was observed for the 2.5% GNP test surface, while the lowest cycle time was obtained for 1% GNP and 2% GNP test surfaces was approximately 7 ms. The corresponding cycle time for a plain copper surface was much higher (13.25 ms). Figure 26a shows the progression of vapor bubbles from the nucleation cavity for different GNP concentration surfaces and from the plain copper surface. The third image in each sequence is of the diameter just before the departure from the boiling surface. The delayed bubble departure on the 2.5% GNP test surface was attributed to the effect of multiple contraction and expansion of a bubble before departing from the cavity that reduced the number of bubbles formed per unit time. This was reflected in higher wall superheat temperatures and reduced CHF obtained for 2.5% GNP surface compared to 2% GNP test surface. Hence, a close relation between bubble departure diameter and CHF, HTC is determined and dictated by the vapor bubble behavior during boiling.

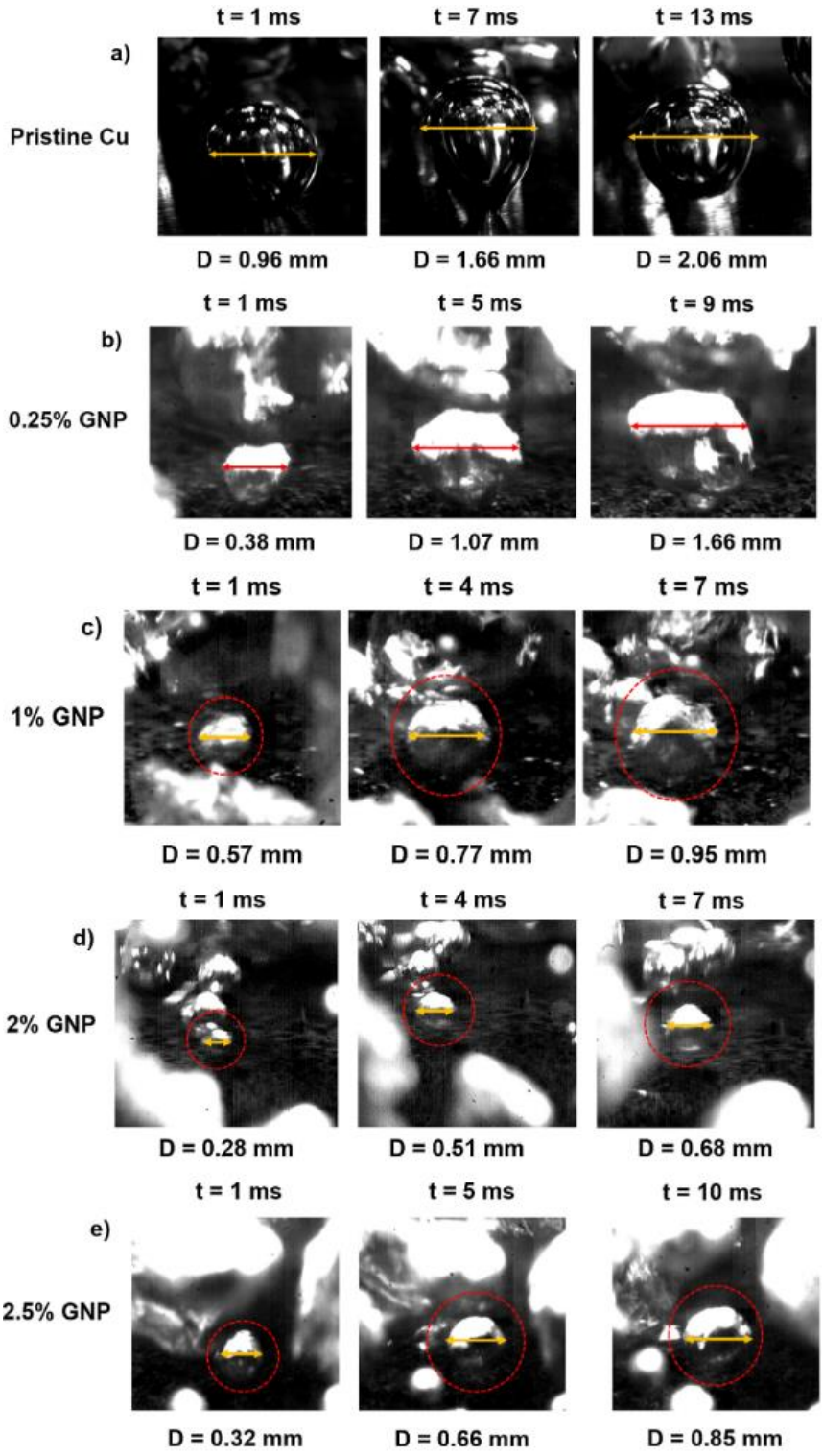

Figure 26. High-speed images representing the sequence of bubble nucleation, growth, and just before departure for different GNP surfaces and a plain copper surface

4.1.1.5.2 Hierarchical pores and wickability

The hierarchical porous structures obtained via composite coatings of GNP/Cu played a significant role in enhancing wicking properties and promoting nucleation. Previous work with copper/graphene oxide coatings yielded a variety of mechanisms with varying CHF and wall superheats. Galvanostatic electrodeposited Cu/GO surfaces produced highly wickable Cu dendritic tall structures with underlying GO sheets that promoted nucleation [51]. The taller microporous structures possess a temperature gradient with a range of cavity sizes that served as additional nucleation sites.

In the present study, two-step electrodeposition of 2% GNP/Cu test surface yielded the highest CHF at low wall superheat temperature reported in pool studies involving graphene and porous coatings. Graphene nanoplatelets (GNP) are composed of few layers of graphene with a very high surface area compared to monolayer graphene sheets [52]. It is well known that as the number of layers of graphene increases, the graphene loses its thermal and mechanical properties and behaves similar to graphite [53]. However, in case of GNP, despite the increase in the number of layers, GNP emulate the properties as that of the single layer of graphene and possess a higher surface area [52]. These properties of GNP contribute towards achieving higher heat fluxes as compared to graphene mono and multilayers.

Higher surface area of GNP led to increased binding with copper particles during the electrodeposition process that formed a unique taller porous matrix. The resultant morphology offers improved surface wickability and wettability, promoting nucleation and microlayer partitioning, as summarized in Fig. 27. A surface is regarded, highly wickable when there is high volume of liquid being wicked into the coating and this retention of liquid in tall porous structures promotes evaporation. A thin film or microlayer is present

under the bubble and microlayer evaporation develops when the liquid is captured under the growing bubble. When the microlayer evaporates due to the solid/fluid contact profiles, it promotes the heat transfer by intensifying the bubble growth. Partitioning results in additional liquid volume available for evaporation, as shown in Fig. 27a. The microlayer film also undergoes thermal relaxations and maintains contact with the wall during the initial superheat domain [54].

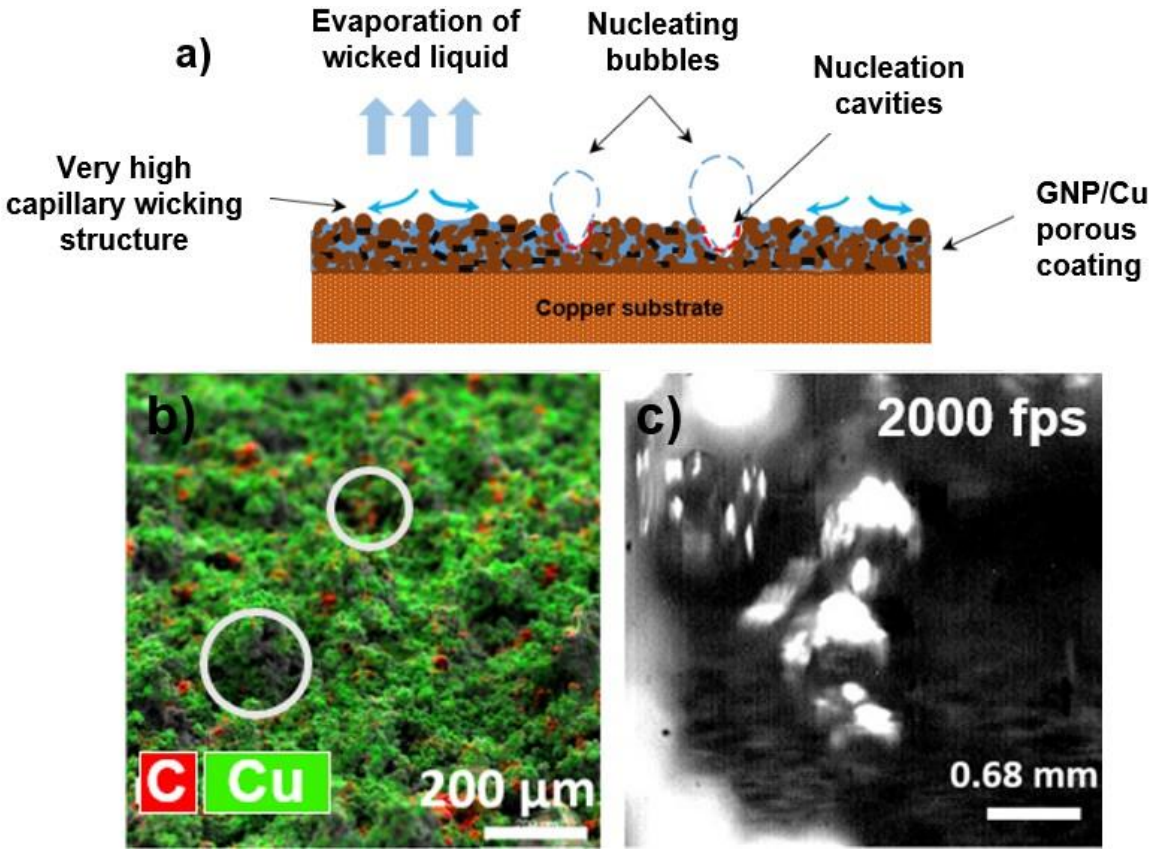

Figure 27. Schematic representation of mechanism of enhanced phase change heat transfer on GNP/Cu surfaces due to a) increased wickability leading to microlayer evaporation, and b) additional nucleation sites for increased bubble growth and departure

The process of nucleation is further promoted by enhanced evaporation through microlayer partitioning, which occurs when the height of the microlayer is lower than the porous structure heights. Growth in nucleation boiling results in an increased number of

bubbles and frequencies [55] represented in Fig. 27b. The difference in thermal conductivities that give rise to thermal gradients is also known to enhance nucleation [56]. The mechanism by which GNP/Cu surpasses the phase change heat transfer or pool boiling performance of porous and graphene coatings reported in the literature is attributed to an increase in liquid confinement in wicking structures. The resultant nucleation sites that get augmented under suitable wall superheat temperatures further contribute to the reduction of the wall superheat.

4.1.1.6 Comparison of pool boiling performance with literature

In addition to various coatings, Graphene (G) and Graphene Oxide (GO) based coatings have recently gained humongous attention due to very high thermal conductivity of graphene. Figure 28 compares the pool boiling performance from literature using different coatings on a plain flat surface with this work [57]-[58]. It is observed that compared to existing techniques and coatings, electrodeposited GNP/Cu-based composites yielded the highest CHF and HTC performance. Owing to its hydrophobic nature, graphene coatings lack the rewetting phenomena, which lead to lower CHF [59]. However, an array of hierarchical porous coating of GNP/Cu composite forms a highly wicking structure with a very high wicking rate. This leads to improved microlayer evaporation and higher CHF.

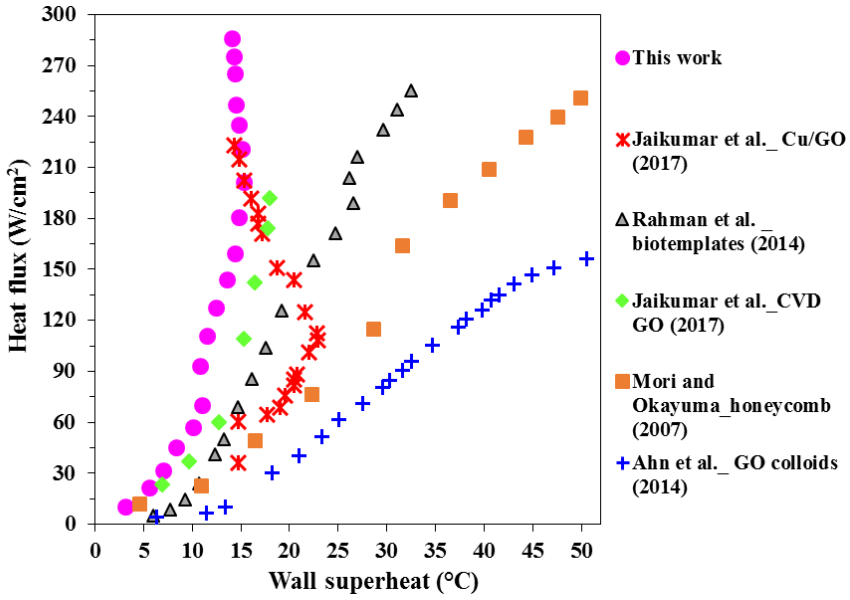

Figure 28. Comparison of pool boiling of current work with existing literature

4.1.1.7 Durability study of the GNP/Cu test surfaces

Pool boiling is an extremely vigorous process and involves continuous intense bubble activity on the boiling surface, which can damage the coating. Additionally, the durability study of coatings is essential for their applicability in industries. A fundamental understanding of the effects of repetitive boiling on the coatings is also crucial for further enhancement. Thus, repetitive pool boiling tests till CHF were performed on the best performing GNP-Cu coating. Scanning electron microscopy and Raman spectroscopy analysis were performed on the coatings after three repetitive tests. The contact angle of the coating after 3 repetitive tests was also measured to understand the effect of repetitive boiling on wettability of the coating.

Figure 29 shows the pool boiling and heat transfer performance for the three repetitive tests. With each repetitive pool boiling test, a small reduction in CHF was observed. However, a drastic enhancement in heat transfer efficiency was attained after each repetitive test. Figure 29b shows the pool boiling and heat transfer coefficients of the

repetitive tests (T1 – repetitive test 1). A maximum HTC of ~300 kW/m²-°C was recorded for the third repetitive test of 2% GNP-Cu surface, providing ~456% increment in HTC when compared to HTC of the plain copper surface.

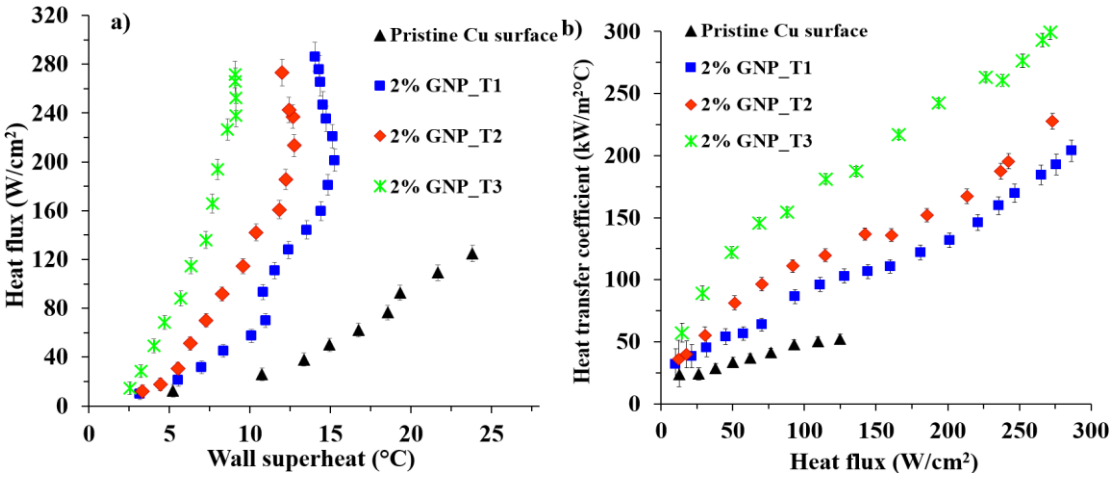

Figure 29: Repetitive pool boiling studies of 2% GNP/Cu test surface showing a) Heat fluxes vs wall superheat plot depicting pool boiling curve, and b) Heat transfer coefficient vs heat fluxes summarizing heat transfer performance (R1 – repetitive test 1)

4.1.1.7.1 Effect of repetitive testing on the surface morphology of GNP-Cu coatings:

The subsequent changes in morphology after 3 repetitive pool boiling tests on the best performing surface (2% GNP-Cu) are shown in Fig. 30. The images were captured at the same magnification, both before and after the tests. EDS analysis indicates the presence of carbon on the coating after repetitive boiling tests, indicating the strong adhesion achieved via the multi-step electrodeposition technique.

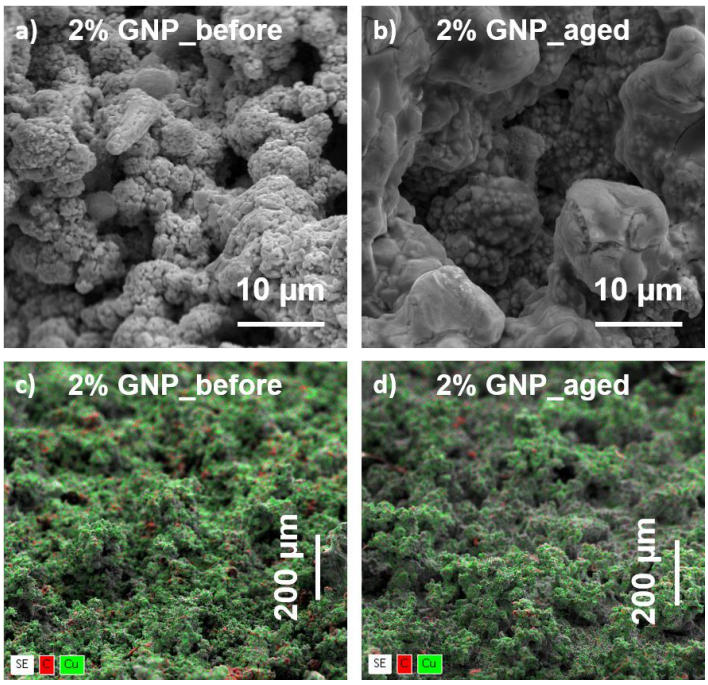

Figure 30. Comparison of SEM images of 2% GNP surface before and after 3 repetitive boiling tests at 5 kX a, b) Top view and c, d) 70° stage tilted view

As observed from Fig. 30a-d, with repetitive testing, substantial morphological changes were not observed. However, the pore size of the coating was increased from 0.6-5 µm to 2-10 µm. This can be due to extremely intense and vigorous bubble activity during the boiling and continuation of the boiling test till the CHF. Stage tilted SEM images before and after repetitive tests show the traces of both carbon and copper on the coating. Adhesive and cohesive bond strength of the coatings can further be enhanced by implementing a multi-step electrodeposition technique [60].

4.1.1.7.2 Effect of repetitive testing on graphene layers and quality of graphene:

For 2% GNP-Cu test surface, before pool boiling test, the Raman absorption peaks for D and G bands were seen at ~1350 cm^{-1} and ~1583 cm^{-1} respectively with G peak intensity higher than D peak intensity, while after 3 repetitive pool boiling tests, intensity

of D band became more prominent than G band, both without shifting their positions. The ratios of D and G bands, I_D/I_G correlate to the degree of disordered carbon as expressed by sp^3/sp^2 carbon ratio. Reduced graphene nanoplatelets (r-GNP) is a state of GNP in which the reduction process occurs with the removal of oxygen and/or hydroxyl groups along with the formation of defects in tightly packed graphene sheets. As seen from Fig. 31, the increased D peak intensity after 3 repetitive tests indicates the increased sp^3 hybridized carbon atoms. This change in D band intensity indicates the self-healing and successful reduction of GNP to reduced-GNP (r-GNP), allowing the restacking of graphene layers. The reduction process of GO to rGO after repetitive pool boiling was observed in previous work [61]. A similar reduction of GNP to r-GNP is observed in this study as well.

The 2D peak for the GNP-Cu surface before the test was observed at ~2690 cm^{-1}. With repetitive pool boiling, a widened peak at ~2900 cm^{-1} was also observed, which is associated with *D+D'* or *D+G* mode of r-GNP and this peak is a combination of D and D' peaks. This peak is observed for the samples with sufficient defects. This again confirms the successful reduction of GNP to r-GNP. Interestingly, the number of layers of GNP (determined by the ratio of I_G/I_{2D}) after repetitive boiling tests remained the same. This indicated the strong adhesion between the GNP-Cu composite and the substrate due to the implementation of the two-step electrodeposition technique.

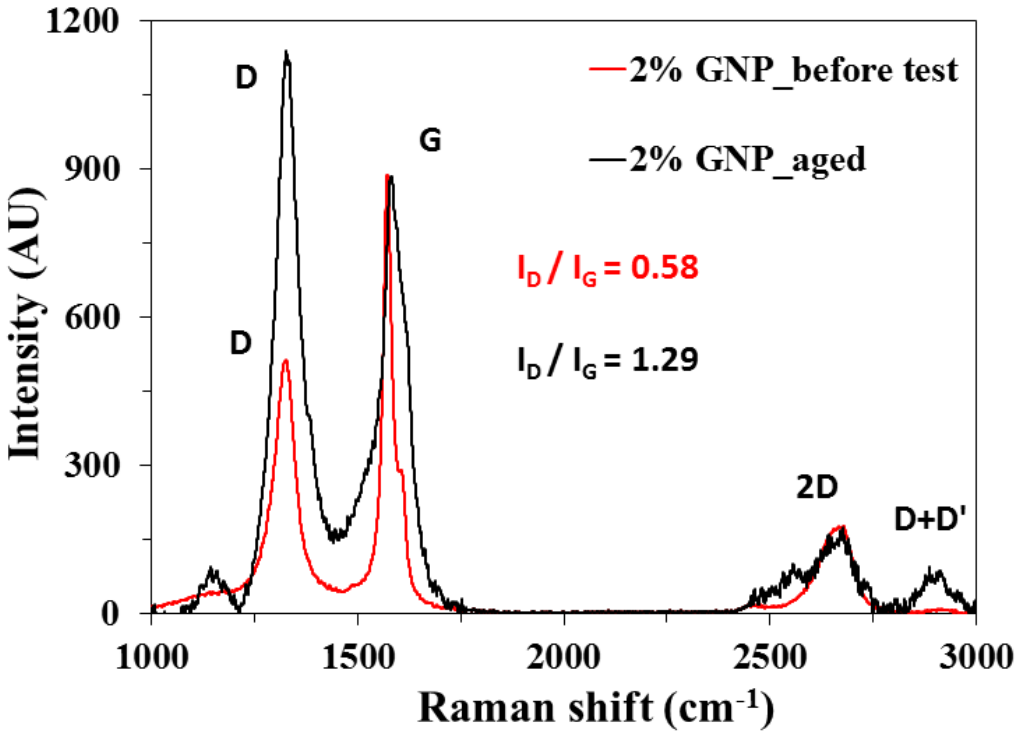

Figure 31. Comparison of Raman spectra of 2% GNP surface before and after 3 repetitive pool boiling tests

4.1.1.7.3 Enhancement mechanisms for aged GNP/Cu coatings

4.1.1.7.3.1 Hydrophilic to hydrophobic transition: Mechanism for enhanced heat transfer coefficient of the coating

Initially, after implementing the two-step electrodeposition technique, a superhydrophilic coating with a very high wickability was achieved for all GNP wt. % coatings. Figure 32 a, b shows the propagation of water droplet for 2% GNP-Cu coating before pool boiling test captured with a high-speed camera. Extremely high wicking rates of the coating delayed the vapor blanket formation on the boiling surface due to continuous liquid supply to nucleation sites and intensified microlayer evaporation during boiling.

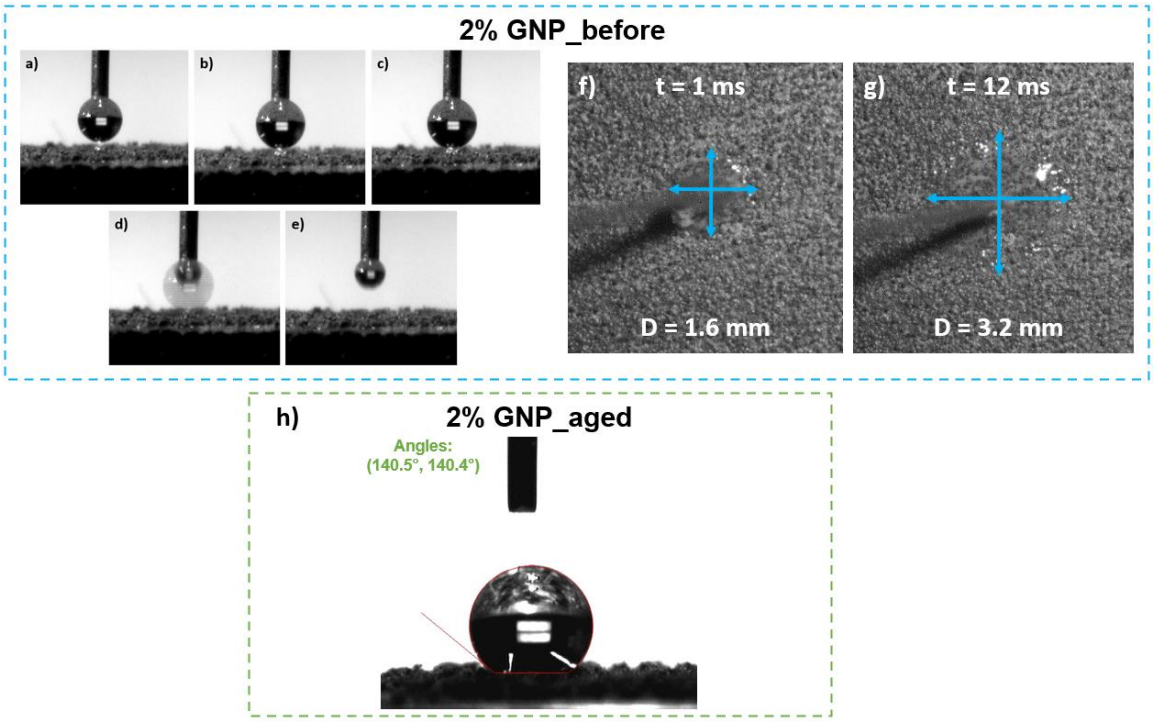

Figure 32: Images showing wicking from side view on 2% GNP/Cu coating before the test (a – e), f) and g) indicating the wicking phenomena with propagation of water droplet twice the droplet diameter on 2% GNP/Cu coating before the test from top view, h) indicating the superhydrophobicity of 2% GNP/Cu coating from side view after 3 repetitive boiling tests

However, after 3 repetitive pool boiling tests, it was observed that the coating did not possess any hydrophilic and wicking characteristics due to removal of oxygen and hydroxyl groups (confirmed via Raman spectroscopy analysis), which resulted in absolute reversal of wetting characteristics, yielding almost superhydrophobic coating with a contact angle of 141±1° (as shown in Fig. 32 h for 2% GNP-Cu coating. Contact angles were measured at 4 different locations and the average of both left-side and right-side contact angles were used to calculate the average value. Hydrophobic surfaces provided early nucleation as compared to superhydrophilic surfaces. This resulted in the reduction of wall superheat temperature during the repetitive pool boiling tests. In the previous work [26], it has been discovered that with repetitive pool boiling, graphene oxide (GO) reduces

and converts to reduced-graphene oxide (rGO). rGO is the reduced state of graphene oxide with eliminated oxygen-based groups, due to which rGO behaves similarly to pristine graphene. Again, the reduction of GNP to r-GNP was confirmed by Raman spectroscopy study. With this reduction, the thermal conductivity of GNP tends to increase. The combination of these two factors of early nucleation and reduction of GNP to r-GNP caused a drastic enhancement in the heat transfer coefficient (HTC) of the coating for repetitive pool boiling tests (Fig. 29b).

4.1.1.7.3.2 Roughness effect and unique morphological microscale coating: Mechanism for higher CHF of aged GNP/Cu coatings

CHF for 2% GNP/Cu coating after the third repetitive boiling test was ~260 W/cm². In addition to higher in-plane thermal conductivity of GNP, morphology, and surface roughness induced mechanisms are responsible for higher CHF values. Current trends and studies have shown that the increase in surface roughness tends to increase CHF. The Kandlikar model has been established for predicting the CHF on plain surfaces [62]. The Kandlikar model has further been modified by Chu et al. [63] which includes the effect of roughness in predicting the CHF on microstructured surfaces. The equation to predict the CHF based on roughness augmented structures is given as follow:

$$q''_{CHF} = K * h_{fg}\rho_g^{1/2} * [\sigma_{lv} * g * \rho_l - \rho_g]^{1/4} \quad (13)$$

Where, $K = \left(\frac{1+\cos\beta}{16}\right) * \left[\frac{2*(1+r*cos\beta)}{\pi(1+cos\beta)} + \frac{\pi}{4}(1+cos\beta)*cos\varphi\right]^{1/2}$

In these equations, h_{fg} represents the latent heat of vaporization, σ_{lv} represents the surface tension of water at saturation temperature, ρ_l and ρ_g are the liquid and vapor densities, g

is the acceleration due to gravity, r is roughness, β is receding contact angle, and φ is the angle of inclination. An additional term $(rcos\beta)$ was incorporated to account for the surface roughness effect in the Kandlikar model. The surface roughness of 2% GNP/Cu composite coating was estimated using laser confocal microscope and was ~15 μm. The coating developed in this work has a non-uniform microstructured morphology and thus, this roughness value is assumed and considered while estimating the CHF using equation 13. The receding contact angle was measured using VCA Optima Goniometer. Compared to CHF of ~260 W/cm², an estimated CHF of ~220 W/cm² was obtained. This indicates that in addition to surface roughness, the higher in-plane thermal conductivity of GNP and formation of hierarchical GNP/Cu composite porous structure were responsible for the CHF enhancement.

4.2 Pool Boiling and Durability Enhancement via Multi-step Electrodeposition Technique:

Adhesion of the electrodeposited coatings mainly depends on the substrate bond strength. Higher bond strength will ensure the ability of the coatings to withstand repetitive boiling. Current electrodeposition techniques do not yield a strong bond between the electrodeposited coating and the substrate and thus, the repetitive boiling tests result in gradual peeling off the coating. Hence, to enhance the bond strength, a multi-step electrodeposition technique is developed with an initial bonding step of lower current over a longer period followed by alternating steps of coating deposition at high current densities over a short period and bonding steps at low current densities over a prolonged duration. An in-depth explanation of each step and the comparison of the achieved coatings with the conventional two-step electrodeposition technique is provided in the following section.

4.2.1 Development of microporous coatings using multi-step electrodeposition techniques:

4.2.1.1 Two-step (2-S) electrodeposition technique:

For the two-step electrodeposition technique, different current densities and time durations are applied in each step. For creating a microporous surface, the evolution of hydrogen bubbles is essential. The two-step electrodeposition was performed by initially coating with higher current density for a short duration of time, followed by a lower current density for a longer duration of time. In the first step, copper deposition occurred along with the evolution of hydrogen bubbles (as shown in Fig. 33b), while in the second step, lower current density was chosen such that further deposition of copper occurred with very low evolution of hydrogen bubbles. The values of current density and time duration for

each step are chosen from the optimum values for enhancing pool boiling CHF as suggested by Patil and Kandlikar [35]. For step 1, a current density of 400 mA/cm² is applied for 15 seconds, while for the second step, a current density of 40 mA/cm² is applied for 2500 seconds. This served as a baseline surface which is then used for the comparison with newly developed electrodeposited surfaces.

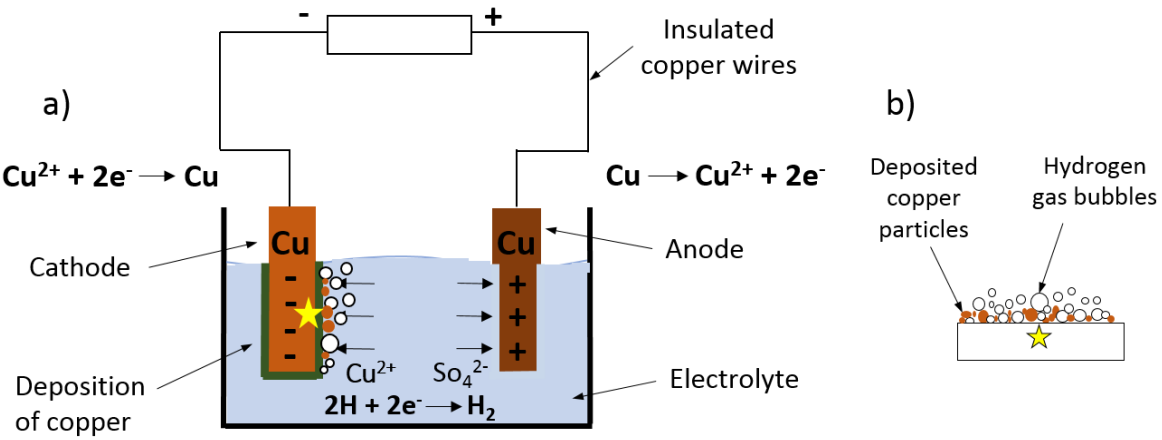

Figure 33: Schematic showing a) High current electrodeposition step b) Evolution of hydrogen bubbles at the cathode with simultaneous deposition of copper during high current step

4.2.1.2 Three-step (3-S) electrodeposition technique:

The multi-step electrochemical deposition method comprises of alternate and strategic application of high and low current steps. A distinct porous and durable coatings can be achieved by either starting with a low current step that results in the formation of an initial base layer of deposited metal that supports a bonding ground for successively deposited metal ions or starting with a high current step that adopts hydrogen bubbles to provide a framework for the deposition that gets strengthened by the subsequent low current step. However, when the multiple electrodeposition steps are terminated at the high current step, the deposited layer will constitute large amounts of deposited metal that may not necessarily be strong.

The three-step electrodeposition technique implemented in this work includes an initial step of application of low current (LC) density for a higher time (HT) that results in the deposition of an initial base layer of the coating material on the copper substrate. Figure – shows the schematic representing the 3-S electrodeposition technique and corresponding deposition occurring on the cathode. This layer acts as a support to sustain the deposition of additional coating material with enhanced bonding. This initial step is helpful because the following step involves a higher current (HC) density for a lower time (LT) to deposit copper particles in an open porous network and the base layer provides a suitable bonding surface. The last step of low current density shown in Fig. 34a ensures the strong adhesion of the copper particles with the base layer, providing a unique microporous structure with higher porosity. Table 4 shows the number of steps and corresponding current and time values.

Table 4. Three-step electrodeposition technique.

Step #	**Step ID**	**Current density (mA/cm^2)**	**Time (sec.)**
1	LC (Low Current) – HT (High Time)	40	2500
2	HC – LT	400	15
3	LC – HT	40	2500

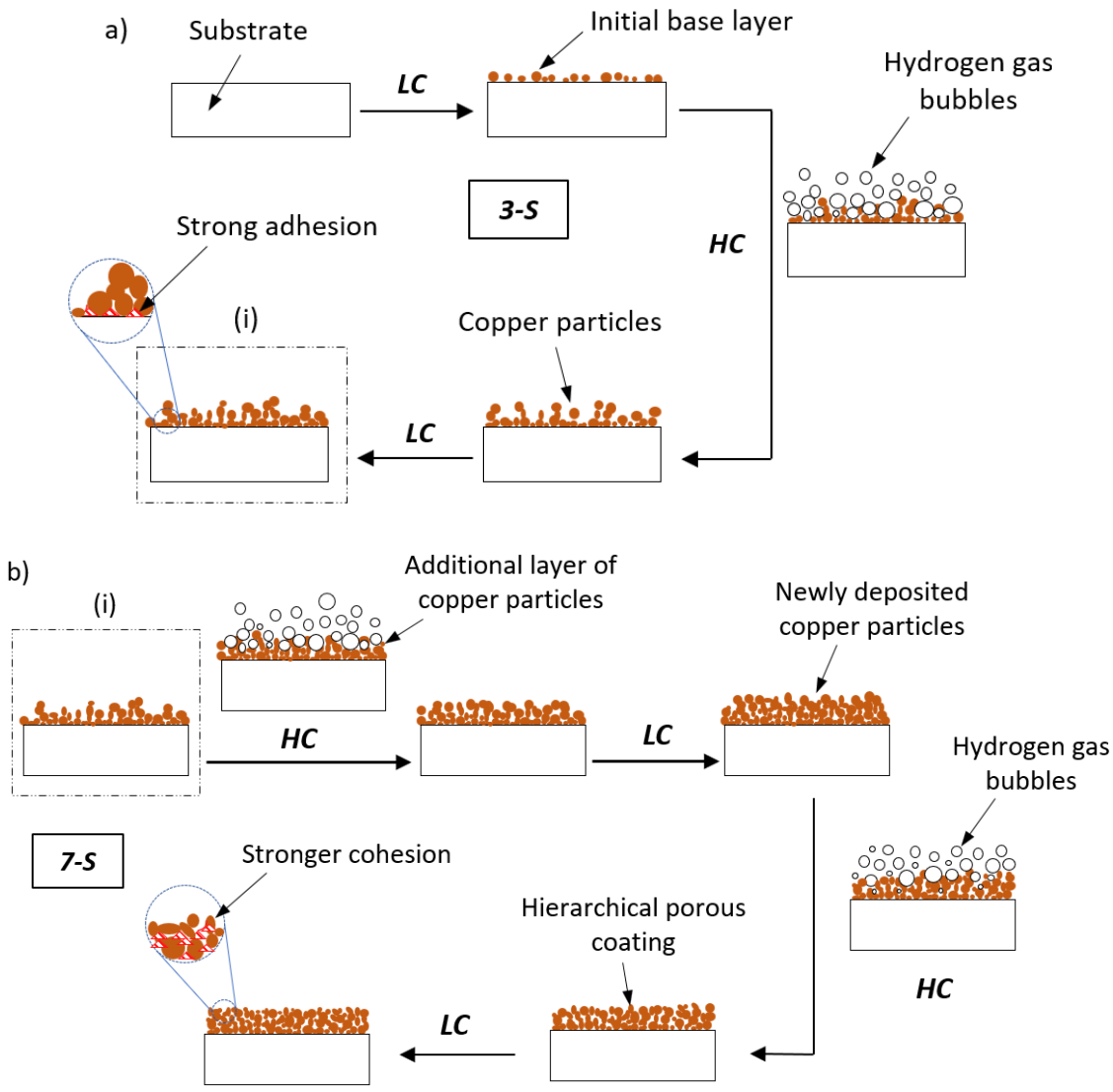

Figure 34: Schematic showing effect of low current (LC) step followed by high current (HC) and low current steps respectively for electrodeposition of copper on copper

4.2.1.3 Seven-step (7-S) electrodeposition technique:

A better control on different surface characteristic properties such as porosity, morphology, thickness, and pore size formation and distribution can be obtained by increasing the number of electrodeposition steps. To test this, a seven-step electrodeposition technique was implemented to develop copper based microporous structures. Similar to 3-S technique, a series of alternate high current low time and low

current high time steps were considered during the electrodeposition. Initially, similar to 3-S, an initial base layer was provided as a support to sustain the deposition of additional coating material with enhanced bonding. Table 5 shows the corresponding time and current values that were used for the formation of coating using the seven-step electrodeposition technique. The schematic shown in Fig. 34b explains the electrodeposition process. In the schematic Fig. 34b, the continuation of deposition after 3-S coating is used and the effect of alternate high and low current steps is indicated. Strong adhesion and cohesion-based hierarchical microporous structure is obtained with seven-step electrodeposition technique.

Table 5. Seven-step electrodeposition technique.

Step #	**Step ID**	**Current density (mA/cm^2)**	**Time (sec.)**
1	LC (Low Current) – HT (High Time)	40	2500
2	HC – LT	400	5
3	LC – HT	40	2500
4	HC – LT	400	5
5	LC – HT	40	2500
6	HC – LT	400	5
7	LC – HT	40	2500

After the first step of low current and high time, a base layer is developed with higher bond strength to the substrate. During the second step of high current density, the copper deposition occurs with the evolution of hydrogen bubbles. The hydrogen bubbles on the copper test surface assist in developing the porous structure. The growth, separation

and coalescence of these hydrogen bubbles determine the pore size and the density. Once the high current density supply is stopped, the evolution of hydrogen bubbles also terminates, and the porous structure is formed. Followed by this, the low current and high duration during the third step of electrodeposition facilitate the bonding of coating with the base material that is already deposited. During this step, the shells of the deposited coatings are formed, and the interconnection of the coating is performed. This way the bond of the deposition is enhanced due to this third step.

During the fourth electrodeposition step, when a high current is again applied for the shorter duration, there is an evolution of hydrogen bubbles, which starts building another layer of the deposition on top of the deposited layer. The evolution of hydrogen bubbles takes place over the entire cross-section of the test chip. This means that bubbles will form at the already deposited coating and as well as in the voids which were previously formed. This is depicted in the schematic shown in Fig. 34b. This phenomenon helps in reducing the size of the pores by simultaneously depositing the copper. The new layer starts forming and it enhances the bonding with the existing coating on the surface (deposited via the first three steps of the electrodeposition). Moreover, this high current step also assists in enhancing the bonds between the deposited material in the voids and the base material. During the fifth step, the application of low current density impedes the evolution of hydrogen bubbles at the cathode. In this step, the activity of strengthening of the deposition of the newly deposited coating of copper is performed. The lower current and the higher deposition duration ensure the slow and steady deposition rate and the enhancement of the adhesive bonding.

When the sixth step of high current density is applied, as shown in Fig. 34b, the new layer of the deposition starts building again with the evolution of hydrogen bubbles on the existing coating. This step helps in refining the pore size and the morphology of the structure will be controlled. The application of this step again coats an additional porous network of copper and provides better control over the morphology of the coating. The final seventh low current density step with higher duration provides the final adhesion to the deposited copper layer and drastically improves the bond strength of the coating.

4.2.2 Comparison of morphology and wettability:

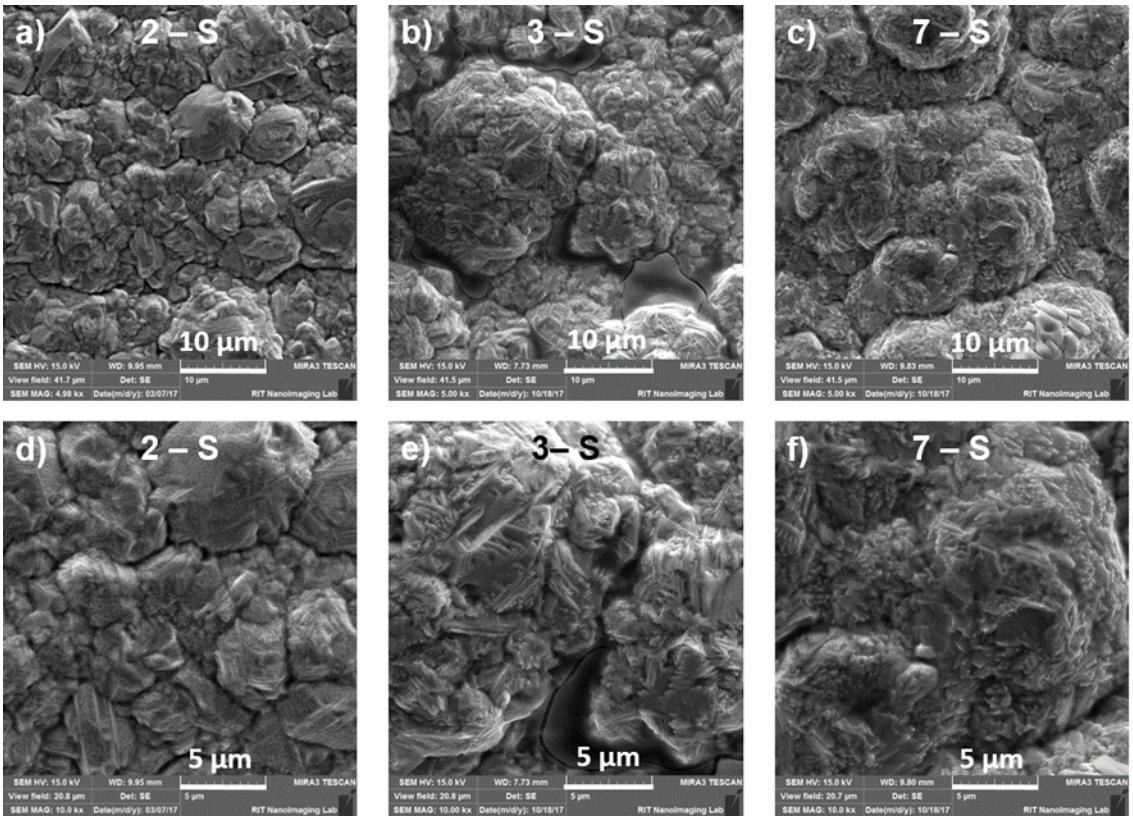

Figure 35: Comparison of scanning electron microscope images for copper-on-copper electrodeposited coatings created with a) and d) two-step (2 – S) electrodeposition technique, b) and e) three-step (3 – S) electrodeposition technique, and c) and f) seven-step (7 – S) electrodeposition technique

Figure 35 compares the scanning electron microscope images of 2-S, 3-S, and 7-S. As seen from Fig. 35b, the feature size of the 3-S coated surface is higher than 2-S. The cauliflower structure is more prominent in the 3-S coated surface and has a diameter ranging from 3 µm to 16 µm. Apart from that, the pore size of the 3-S surface has been reduced, which can further improve boiling performance. The feature size for 2-S deposited surface is in the range of 5 µm to 12 µm. The pore size and density achieved using the 3-S technique is higher, ranging the pore size from 0.9 µm to 4 µm. In the case of a 7-S coated surface, a wide range of feature sizes from 2 µm to 15 µm is achieved. Due to the availability of limited parameters to control, it is observed that the porosity achieved using the 2-S technique is lower and cannot be controlled. Hence, the proposed approach is advantageous in terms of improving the morphological properties of the coatings.

Table 6 shows the comparison of static, advancing, and receding contact angles for the 2-S, 3-S, and 7-S surfaces. A drastic increase in hydrophilicity is observed for the 7-S surface. This indicated that better control on wettability of the coatings is achieved with a multi-step electrodeposition technique, which otherwise would be impossible to achieve using the two-step electrodeposition technique.

Table 6. Comparison of contact angles for different steps electrodeposition

Test Chip	Contact angle (°)			
	Static	**Advancing**	**Receding**	**Hysteresis**
Cu on Cu (Three-Step deposition) (2-S)	53	67	18.4	48.6
Cu on Cu (Two-Step deposition) (3-S)	58	65	21	44
Cu on Cu (Seven-Step deposition) (7-S)	32	38	12.2	25.8

4.2.3 Comparison of pool boiling performance:

To compare the effect of multi-step electrodeposition on heat transfer performance, pool boiling tests with water as a working fluid were performed on 2-S, 3-S, and 7-S copper on copper-coated surfaces. It is observed from Fig. 36a that the CHF values of the test surfaces deposited with proposed multi-step electrodeposition techniques are much higher than both the existing two-step electrodeposited surface and a plain copper surface. CHF of 213 W/cm² at wall superheat of 21.6°C was achieved for the seven-step (7-S) electrodeposited surface. For the copper electrodeposition on a plain surface, this is the highest heat flux that has ever been achieved. Compared to the plain copper, ~72% enhancement in CHF and ~93% enhancement in HTC (as observed from Fig. 36b) was achieved with the 7-S coated surface. The 3-S deposited surface also gave higher performance than the 2-S surface, giving CHF of 169 W/cm² at wall superheat of 15.6°C.

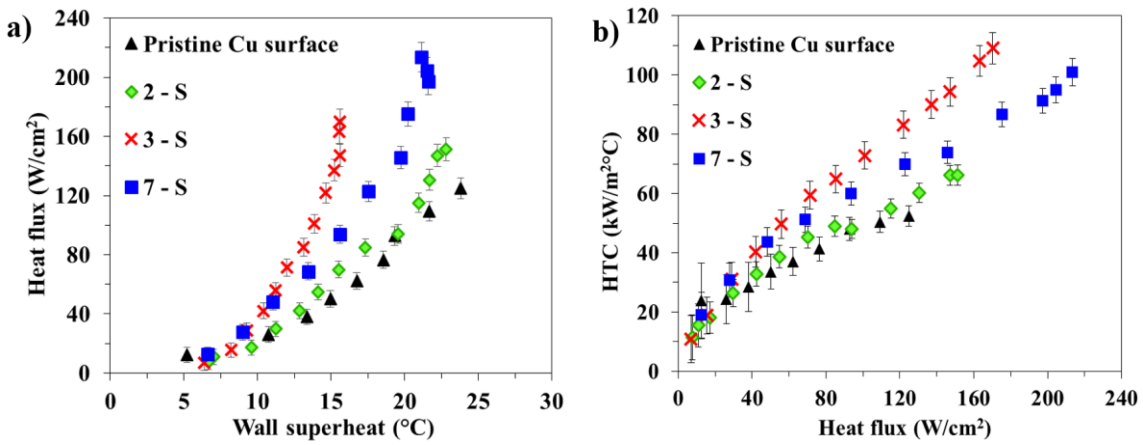

Figure 36: a) Comparison of pool boiling curve, b) comparison of heat transfer coefficients for various multi-step copper on copper electrodeposited surfaces

Improved morphological structure increased nucleation sites, which helped in the rapid boiling process and increased CHF. However, an increase in the number of steps increased coating thickness, leading to an increment in thermal resistance due to coating. Thus, compared to the 7-S surface, a lower wall superheat temperature was attained by the 3-S surface. Table 7 below shows the comparison of CHF and HTC of various surfaces with the plain copper surface.

Table 7: CHF & HTC comparison with respect to the plain copper surface

Test surfaces	**CHF (W/cm^2)**	**% Enhancement in CHF**	**HTC (kW/m^2-°C)**	**% Enhancement in HTC**
Plain Cu	125		53	
2-S (Cu coating)	151	22	66	27
3-S (Cu coating)	170	37	109	108
7-S (Cu coating)	213	72	100	93

4.2.4 Durability or aging study of electrodeposited surfaces:

Due to repetitive pool boiling, the morphology of the coatings prepared with conventional single and two-step electrodeposition process alters, reducing boiling performance and removal of the coating. The test surfaces created using the proposed multi-step electrodeposition technique aim at improving the long-term use of the surface by enhancing the cohesive and adhesive bond strength of the coatings to sustain repetitive boiling.

The aging study was performed on copper-on-copper electrodeposited surfaces to compare the advantages of the newly employed electrodeposited coatings in terms of longevity and adhesion improvement. Boiling involves vigorous motion of bubbles on the surface and causes damage to the bonds of the electrodeposited surface. The damage is more if the substrate bond strength is less and if the adhesive forces are weak. These weak forces also reflect the reduction of pool boiling performance and increase in wall superheat temperature, which is the temperature difference between substrate surface temperature

and the saturation temperature of the bulk fluid. Hence, if the bond strength is more, the boiling performance will be better, and a wall superheat temperature will be lower.

In this study, the bond strength was established through pool boiling studies by conducting repetitive boiling tests over long durations and observing the performance degradation in the boiling curve over the repetitive testing. Repetitive pool boiling tests were performed on the same test surface repetitively. Heat flux was raised to 80 W/cm^2 for each pool boiling test and then again reduced back to zero, thus tracing the pool boiling curve backward. Between two successive pool boiling tests, the cooling cycle was of 20 hours.

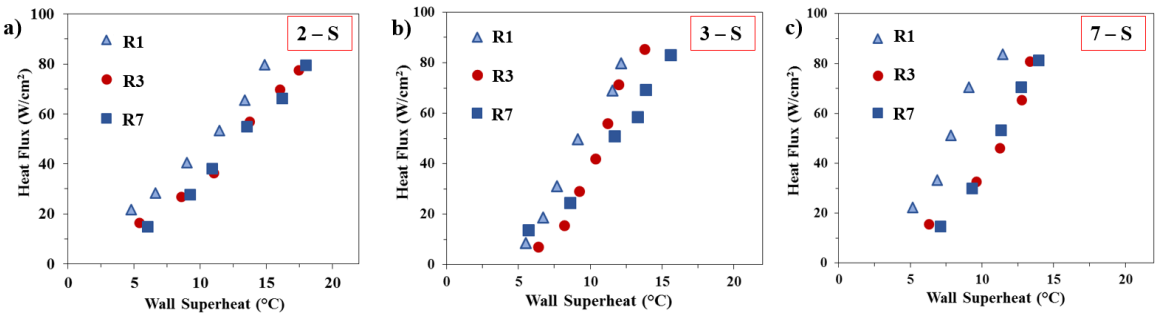

Figure 37: Comparison of wall superheat copper on copper deposited surfaces at different repetitive pool boiling tests (R1 – first repetitive test) a) two-step (2 – S), b) three-step (3 – S), and c) seven-step (7 – S)

Figure 37 shows the comparison of wall superheat temperatures for different multi-step electrodeposited surfaces. It is observed that compared to the conventional two-step (2 – S) electrodeposition technique, surfaces coated with three-step (3 – S) and seven-step (7 – S) electrodeposition technique show lower wall superheat at each repetitive boiling test, indicating higher bond strength. For example, wall superheat at the end of the 7th repetitive test for 2 – S surface was 18°C, while the corresponding wall superheat for 3-S and 7-S were 15.65°C and 14°C. This also translated in higher heat transfer coefficients

for 3-S and 7-S surfaces, indicating higher efficiency of these coatings. This improvement in the aging performance of the 7-S surface is primarily due to enhancement in cohesive and adhesive bond strength which assisted in sustaining the repetitive pool boiling testing and a hierarchical microporous coating maintained the lower wall superheat temperature as compared to 2-S and 3-S coatings.

4.3 Effect of Ball Milling Followed by Sintering of Graphene Nanoplatelets/Copper (GNP/Cu) Composite Coatings on Pool Boiling Performance and Bubble Dynamics:

Concept and hypothesis:

Here, a distinctive approach was followed to develop graphene nanoplatelets-copper (GNP-Cu) composite coatings via a combination of ball milling and sintering methods. High-energy ball milling is known to be a cost-effective technique that is widely used to form composite materials and alloys because of its ability to create a homogeneous mixture. While sintering process comprises of the formation of microporous coating by heating the metal particles without melting them to the point of liquefaction. It was hypothesized that the ball milling will enable the draping of highly thermally conductive graphene nanoplatelets (GNP) around the copper particles and sintering these GNP-draped-copper particles will result in microporous coatings with enhanced wetting and wicking properties. This will improve the pool boiling heat transfer performance.

Preliminary studies: *Validation of effectiveness of ball milling followed by sintering technique over merely sintering technique*

To test whether ball milling of GNP-Cu particles before sintering will be beneficial for pool boiling enhancement, a variety of coatings were formed using different copper particle diameters and different GNP concentrations. The pool boiling performance of merely sintered coatings was compared with the coatings formed by the ball milling + sintering technique to determine the superiority of the latter. Table 8 shows the test matrix created for the validation of the ball milling concept.

Table 8. Test matrix for comparing the effect of copper particle size and effect of ball milling followed by sintering of GNP and copper

Sample preparation technique	Composition
Only Sintering	1 µm Cu particles + 2 wt. % GNP
	20 µm Cu particles + 2 wt. % GNP
Ball Milling followed by sintering (BM + sintered)	1 µm Cu particles + 2 wt. % GNP
	20 µm Cu particles + 2 wt. % GNP
	45 µm Cu particles + 2 wt. % GNP

4.3.1 Ball milling technique:

Ball milling is a solid-state powder processing technique with repeated cold welding, fracturing, and re-welding of powder particles. During the ball milling process, the powder particles are loaded in the metal cylinder along with a process control agent and milling balls. Two different powder particles can be combined during a ball milling to yield a homogeneous mixture of the two components. Ball milling also reduces the resultant particle size and is a cost-effective technique to achieve a homogeneous powdered mixture of two different components. In this work, a high-energy ball mill obtained from Across International was used for the ball milling of GNP and copper particles, schematically shown in Fig. 38.

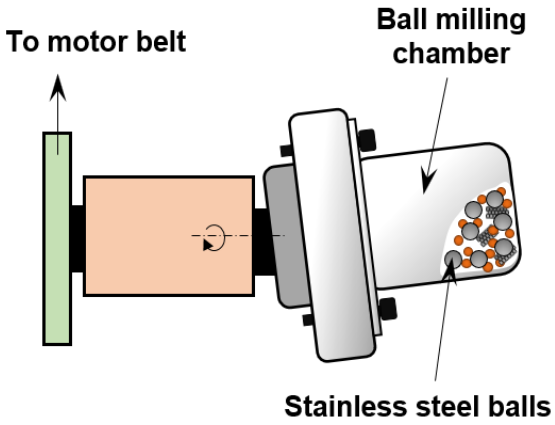

Figure 38: Ball milling process

For higher efficiency, a small quantity of copper particles and varying GNP concentration was blended by loading them into the ball milling chamber. Before loading the composite particles mixture, GNP and copper particles were dispersed in the ethanol bath for 30 min to achieve a homogeneous mixing. The entire solution was then transferred into the ball milling chamber along with stainless-steel balls, and the ethanol was used as a process control agent during the ball milling process. The ball-to-powder ratio of 40:1 was used to ensure the homogeneous distribution of GNP in the copper particles. The entire mixture was ball milled at 700 rpm for one hour. After every 15 min of ball milling, the ball milling chamber was allowed to cool down for one hour to avoid overheating. The resultant ball milled composite particles were then screen-printed on the copper test surfaces using the binder obtained from Nazdar SourceOne. The binder to powder ratio of 1:2 was maintained for developing all the sintered coatings. This ratio was selected based on previous studies that showed better boiling performance using this particular ratio [51].

4.3.1.1 Sintering via screen-printing:

Sintering is a thermal process by which the adjacent metal particles are bonded together to enhance the final properties of the metal powder compact. The loose metal and/or non-metal and/or composite powder is typically screen-printed on the test surface with the addition of sintering oil/binder to achieve the coating. Fig. 39 shows a schematic of a typical screen-printing process. A homogeneous mixture of the powder and sintering oil is transferred onto a substrate using squeegee strokes. This forces the mixture through a screen mesh. Prior to coating, the test sections of the copper substrates were prepared to ensure the 1 cm^2 by covering the surplus area with Kapton tape. The exposed boiling area was thoroughly cleaned with distilled water and IPA. The ball-milled powders were mixed with urethane overprint clear screen binder obtained from Nazdar SourceOne and were screen printed on the plain copper test surfaces using a squeegee and a CP-100 frame. The screen mesh with 250 threads/$inch^2$ were used for all the screen-printing processes. The mesh was thoroughly cleaned with IPA, distilled water, and flushed with compressed air after each screen-printing process. The binder to Cu/GNP powder weight ratio was kept constant at 1:2 for all the coatings.

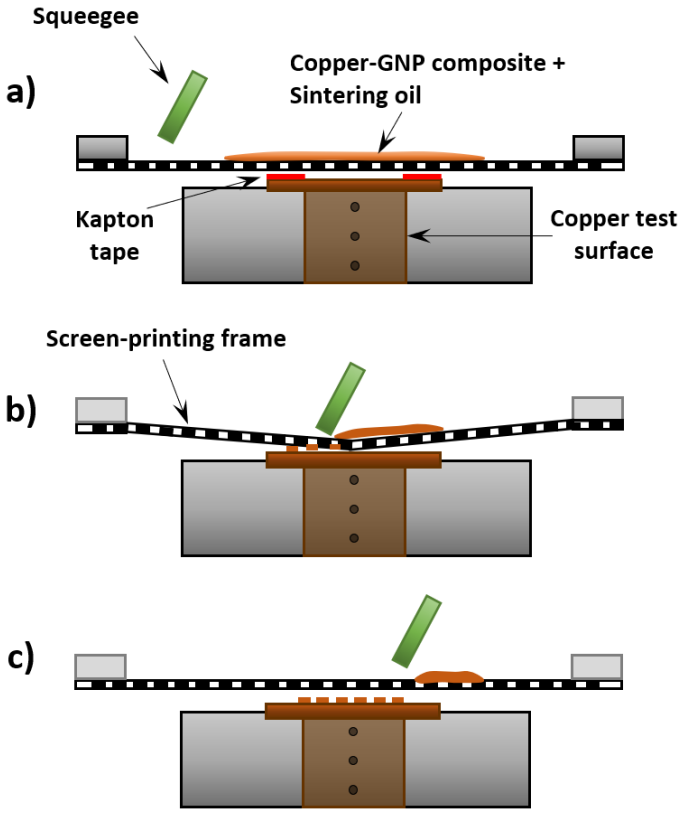

Figure 39. Schematic representing the screen-printing process

Screen-printed surfaces were then transferred to a sintering furnace and sintering was performed under an inert helium atmosphere (Fig. 40). The sintering process consisted of initial heating with a ramp-up to 450°C and the temperature was maintained constant for 30 min in order to burn off the binder from the coating. This was followed by a second temperature ramp to 800°C and holding at that temperature for 1 hr. The sintered coatings were then allowed to cool down in the furnace to room temperature under continuous helium flow.

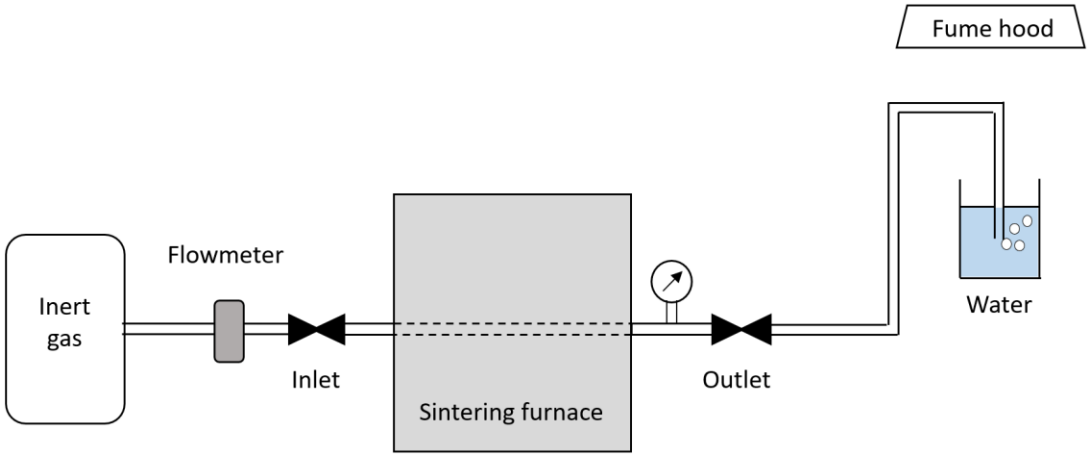

Figure 40: Schematic showing the overall sintering process

4.3.1.2 Pool boiling performance – quantification of critical heat flux and wall superheat:

4.3.1.2.1 Comparison of only sintered and ball-milled followed by sintered GNP-Cu surfaces:

After developing the coatings using only sintering and ball milling followed by sintering characterization techniques were implemented before performing the pool boiling studies with water as a working fluid. Pool boiling tests were then conducted on the surfaces to validate the better efficacy and performance of the ball milled followed by sintered coatings. Table 9 compares the CHF and HTC values of the different coatings.

Table 9. Comparison of pool boiling performance for merely sintered and ball milled followed by sintered coatings

Sample preparation method	**Composition**	**CHF (W/cm²)**	**Wall superheat temperature (°C)**
Sintering only	2% GNP-1 µm Cu	164 ± 8	22.5
	2% GNP-20 µm Cu	237 ± 10.5	16.3
Ball milling followed by sintering	2% GNP-1 µm Cu	164 ± 7.5	10.8
	2% GNP-20 µm Cu	239 ± 10.2	8.4
	2% GNP-45 µm Cu	203 ± 9	9.3

Compared to merely sintered coatings, a substantial enhancement in heat transfer efficiency and the pool boiling performance after the ball milling of GNP and copper particles was observed. One of the primary factors responsible for the enhancement was observed to the uniform spreading of GNP over the entire coating due to the implementation of the ball milling technique. Figure 41 compares the EDS analysis of only sintered, and ball milled + sintered coatings, conforming the uniform spreading of GNP (Fig. 41b and 41d). In the case of sintered coatings, copper particle size is the primary factor that dictates the microporous structure of the coating. SEM images of only sintered and ball milled + sintered coatings confirm the similarity of morphological structures for both the cases, except the GNP spreading phenomena. Ball milling of GNP/Cu composite prior to sintering assists in GNP draping phenomena and thus uniformly spreads GNP. GNP have very high in-plane thermal conductivity (~3000 W/m-K) and uniform spreading of GNP thus efficiently removes the heat during pool boiling. Additionally, higher in-plane

thermal conductivity also reduces local temperature rise and hot spot generation during boiling, thereby enhancing heat transfer coefficients (as observed from Table 9).

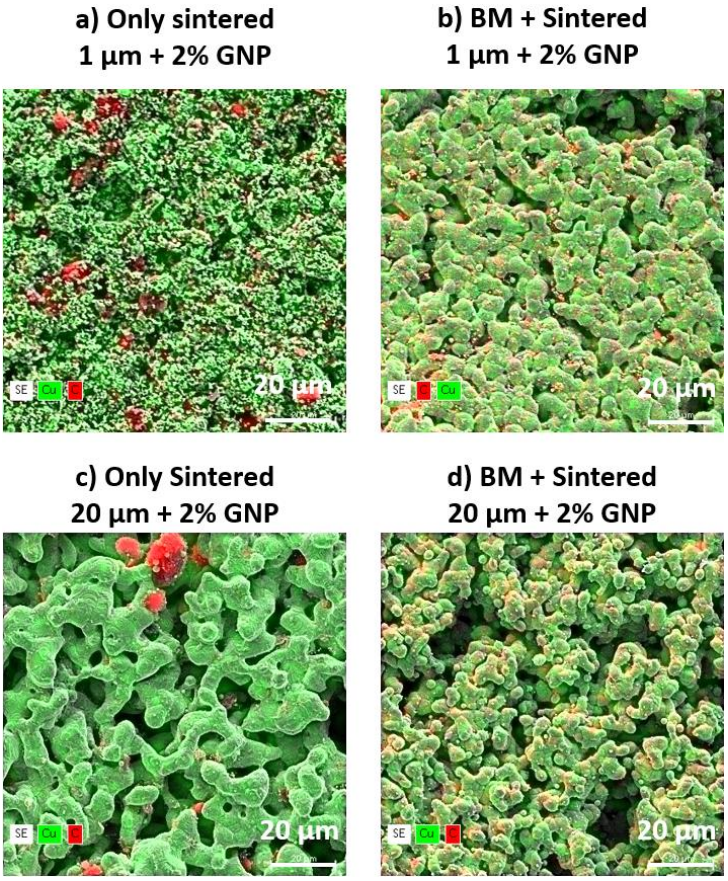

Figure 41. Scanning electron microscope (SEM) images at 500X magnification of sintered surfaces showing carbon and copper mapping a) S1 – sintering of 1 µm Cu-2% GNP, b) BM-S1 – ball milling followed by sintering of 1 µm Cu-2% GNP, c) S2–sintering of 20 µm Cu-2% GNP, and d) BM-S2 – ball milling followed by sintering of 20 µm Cu-2% GNP

After validating that the ball milling followed by sintering-based coatings offer higher surface activity which contributes for enhanced pool boiling heat transfer performance, the effects of different copper particle sizes during ball milling were considered to optimize the pool boiling performance further. Three different copper particle sizes (1 µm, 20 µm, and 45 µm) were subjected to the ball milling while keeping GNP concentration to 2 wt. %. The 2 wt. % GNP concentration was selected based on the

previous work. With increased particle sizes, an improvement in the pool boiling performance was achieved. However, in the case of 45 µm copper particles, a drop in the performance was observed. The highest performance was achieved with 20 µm copper particles. A detailed comparison of morphological structures of different copper particle size sintered surfaces and the number of deposited layers of GNP on these surfaces is provided in the following paragraphs.

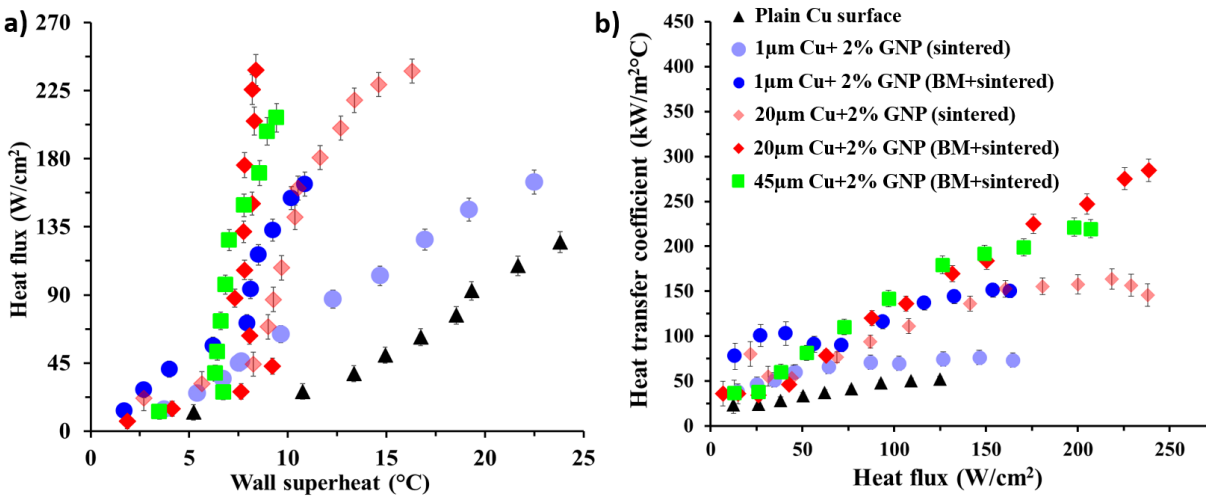

Figure 42. Comparison of the effect of ball milling and the effect of copper particle size during GNP draping on pool boiling performance showing a) Heat Flux vs wall superheat depicting pool boiling regimes, b) heat transfer coefficient vs heat flux summarizing heat transfer performance

Figure 42 compares the pool boiling performance of the only sintered surfaces (labeled as - sintered in Fig. 42), and ball milled followed by sintered test surfaces (labeled as - BM + sintered in Fig. 42). All these coatings were developed without salt templating. The pool boiling performance plot in Fig. 42a showed the highest critical heat flux for the ball milled 2% GNP-20 µm Cu surface. This surface yielded a CHF of 239 W/cm² at a wall superheat of 8.3°C for ball milled 2% GNP-20 µm Cu surface. This is a dramatic increase in the CHF by ~91% and HTC by ~438% compared to a plain copper surface. The highly

desirable low wall superheat is achieved due to uniform spreading of GNP on the boiling surface as a result of draping of GNP around the copper particles caused by ball milling. This is also reflected in increased heat transfer coefficients which are indicative of extremely high heat transfer efficiencies of GNP-draped-Cu surfaces. Microscopically, higher CHF and HTC are attributed to the formation of optimum-sized porous pockets, which act as nucleation cavities to generate additional vapor bubbles that improve the phase change heat transfer efficiency. The nano-sized cavities function as pathways of liquid supply in the porous pockets.

4.3.1.2.2 Enhancement mechanism of ball milled followed by sintered coatings (optimization of copper particles size):

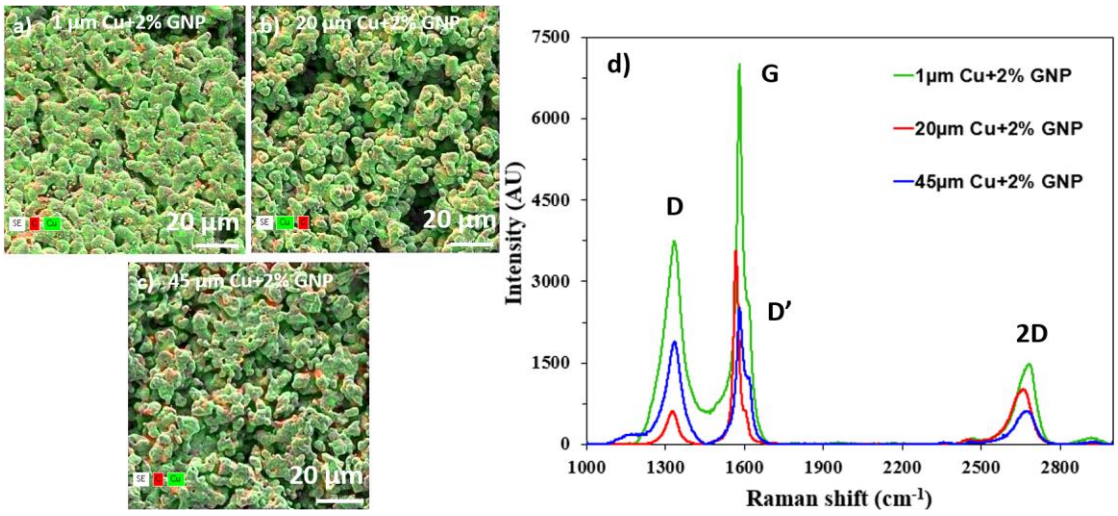

Figure 43. Scanning electron microscope (SEM) images at 500X magnification of GNP draped copper particle surfaces showing carbon and copper mapping a) BM-S1 – 1 µm Cu-2% GNP, b) BM-S2 – 20 µm Cu-2% GNP, c) BM-S3 – 45 µm Cu-2% GNP, and d) comparison of Raman spectra of GNP draped copper particle surfaces

Raman spectroscopy analysis was performed on all three samples (1 µm Cu-2% GNP, 20 µm Cu-2% GNP, and 45 µm Cu-2% GNP) to quantify the number of deposited

graphene layers. Figure 43d shows the Raman spectra, and the ratios of intensities I_D/I_G on the Raman plot demonstrate the oxidation degree and defects of a graphene sheet and ratio I_G/I_{2D} quantify the number of GNP layers in each sample. I_G/I_{2D} ratio of around ~4 for all the GNP surfaces was observed, indicating a multi-layer graphene deposition. I_D/I_G ratios for all three surfaces were less than 1 (0.534, 0.17, and 0.62 for 1 µm Cu-2% GNP, 20 µm Cu-2% GNP, and 45 µm Cu-2% GNP, respectively), indicating the less defects on deposited graphene sheets.

Since the number of deposited GNP layers were approximately the same for all three 1, 20, and 45 µm copper particle surfaces, it is believed that other factors such as wickability, porosity, and overall morphology of the coatings are responsible for the variation in pool boiling results. Various pool boiling studies have shown that liquid spreading or higher wicking properties of the boiling surface assist in delaying vapor layer formation due to continuous liquid supply to the nucleation cavities.

Owing to the higher wettability of GNP and copper particles and uniform spreading of GNP over the entire coating, the formation of hydrophilic sintered surfaces was anticipated. After measuring the contact angles of these surfaces using a Goniometer, all the coatings exhibited a superhydrophilic (0° contact angle) nature. Thus, wickability and wicking rates of all three surfaces were measured using a sessile water droplet method before conducting the pool boiling experiments. Figure 44d shows the comparison of the change in water droplet volume with respect to time for all three surfaces. It was found that the ball milled 2% GNP-20 µm Cu surface yielded the highest wicking rate indicating the highest wicked volume in a short time as compared to the ball milled 2% GNP 1 µm and 45 µm copper surfaces. Thus, higher wickability is established as one of the factors

responsible for the increment in CHF and reduction in wall superheat temperature of the ball milled 2% GNP-20 µm Cu surface.

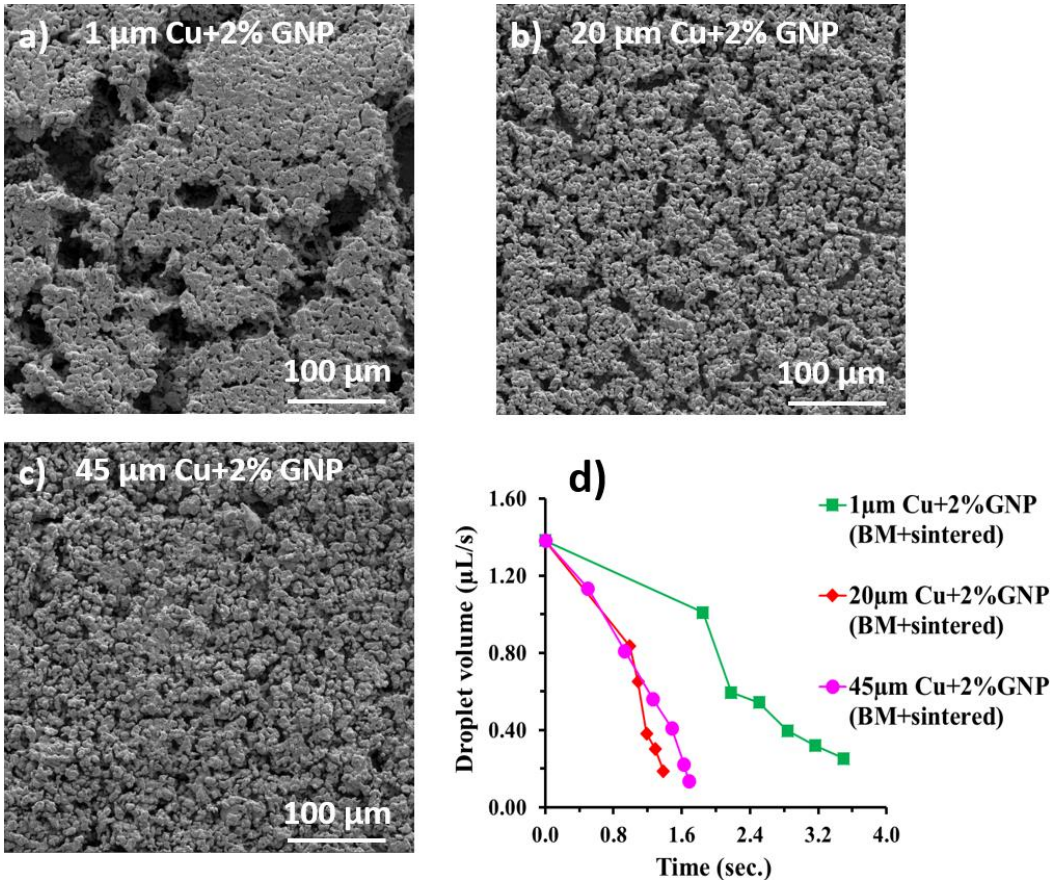

Figure 44. Scanning electron microscope (SEM) images at 500X magnification of GNP draped Cu coatings a) ball milled and sintered (BM + sintered) 1 µm Cu-2% GNP, b) BM + sintered 20 µm Cu-2% GNP, c) BM + sintered 45 µm Cu-2% GNP, d) comparison of change in water droplet volume over time

To comprehend the role of morphological structure in enhancing the overall pool boiling performance, an in-depth morphological analysis on all three coatings was performed. It was detected that there is an optimum size of pore pockets that is responsible for enhancing the effective liquid pathway and a maximum vapor departure. For example, in the case of 1 µm Cu-2% GNP surface, owing to the continuous collision between stainless-steel balls and the powder during the ball milling process, the size of the copper

particles reduced further. An agglomeration of these particles was observed post sintering (Fig. 44a), which led to the formation of huge rectangular-shaped pores termed as “pore pockets” with a length of ~92 µm and width of ~24 µm after the sintering process (Fig. 44a, calculated using ImageJ software). Agglomeration of the particles also reduced the number of small-sized pores as compared to other coatings. This caused early bubble coalescence and reduced both CHF and HTC for 1 µm Cu-2% GNP surface. The reduction in particle size after the ball milling process for 20 µm Cu-2% GNP surface was optimum. This surface generated pore pockets of ~32 µm long and ~7.4 µm wide (Fig. 44b, calculated using ImageJ software). While for 45 µm Cu-2% GNP surface, the pore pockets of ~28 µm long and ~9 µm wide were formed (Fig. 44c).

In addition to the pore pocket dimensions, the number of pore pockets also play a crucial role in determining the pool boiling performance and efficiency of the boiling surface. For the SEM images shown in Fig. 44, the view field is 415 µm at a magnification of 500X. Thus, for this same view field in all the three images (Fig. 44a, 44b, and 44c), a maximum of 17 pore pockets were observed for 20 µm Cu-2% GNP surface, as against 6 and 8 for 1 µm and 45 um Cu-2% GNP surfaces, respectively. Due to the formation of a large number of optimum-sized interconnected porous pockets, 20 µm Cu-2% GNP coated surface yielded the highest performance as compared to 1 µm and 45 µm copper-2% GNP surfaces.

4.3.2 Optimization of GNP concentration for pool boiling studies with ball milled and sintered coatings:

After validation of marginal enhancement and optimization of copper particle size for pool boiling efficiencies with ball milling followed by sintering technique, GNP concentration was optimized for ball milling followed by sintering technique using 20 µm copper particles (optimum size of copper particles). In-depth studies and analysis were performed to establish the mechanism of formation of GNP-Cu composite particles. A separate analysis of ball milled GNP-Cu composite powders was performed using various characterization techniques. Additional analysis on coatings was also conducted to determine the pool boiling enhancement mechanisms. Table 10 shows the test matrix for optimizing the GNP concertation.

Table 10. Test matrix for comparing the effect of GNP concentration during ball milling followed by sintering process

Sample preparation technique	**Composition**
Ball Milling followed by sintering (BM + sintered)	20 µm Cu particles + 2 wt. % GNP
	20 µm Cu particles + 3 wt. % GNP
	20 µm Cu particles + 5 wt. % GNP

Figure 45 shows the overall process during ball milling and the development of sintered coatings using ball milled powder. Ultrasonication of GNP and copper particles in an ethanol bath was performed for proper mixture formation of GNP and copper particles.

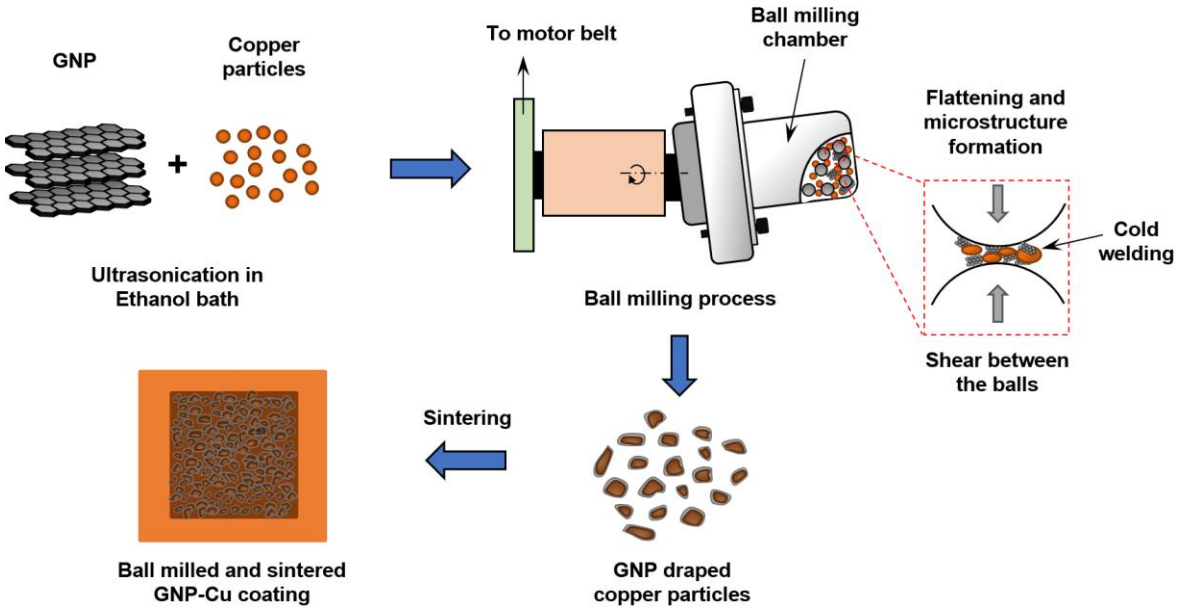

Figure 45: Overall ball milling process and formation of sintered coating via ball milled powder

4.3.2.1 Mechanism of formation and characterization of GNP-draped-copper particles:

Draped GNP copper particles were obtained by a solid-state powder processing technique which involved repeated cold welding, fracturing, and re-welding of copper particles in a high-energy ball mill as shown schematically in Fig. 46a. Smaller quantities of a powdered mixture of copper and varying GNP concentration were blended by loading into the ball milling chamber containing stainless-steel balls. The mixture was then agitated at higher speeds for a predetermined length of time. During this process, the copper and GNP particles are repeatedly flattened, cold-welded, fractured, and re-welded. The effect of a collision between the constituent particles resulted in flattening and hardening of the composite particles, as seen in Fig. 46a. The collisions of the ball to ball and ball to wall cause the entrapment of GNP and copper particles. The force of impact plastically deforms the particles and results in fracture, subsequently work hardening of the particles. The severe plastic deformation also increases the surface-to-volume ratio of the particles.

Additionally, the pure shear between the milling balls prevented the agglomeration of the GNP [66]. The repetitive events of ball to ball and ball to wall collisions throughout the milling period enable the cold welding, which leads to the draping of GNP on copper particles. In this work, after every 15 minutes of ball milling, an hour of cooling cycle to enable a short annealing cycle was implemented to promote the alloying of GNP and copper and GNP draping phase. This is further confirmed with a scanning electron microscope (SEM), transmission electron microscope (TEM), and scanning transmission electron microscope (STEM) characterization tools. The annealing cycle also relieved the internal stresses and defects of GNP caused due to continuous collisions of GNP with the stainless-steel balls and the wall of the milling chamber (Id/Ig ratio less than 1, Raman spectroscopy analysis, Fig. 54e). The ball milling process also promoted considerable reduction in the particle size (~90-95% of the original particle size, observed from STEM and TEM images) and yielded a uniform distribution of GNP around individual copper particles leading to increased wicking rates of the coatings.

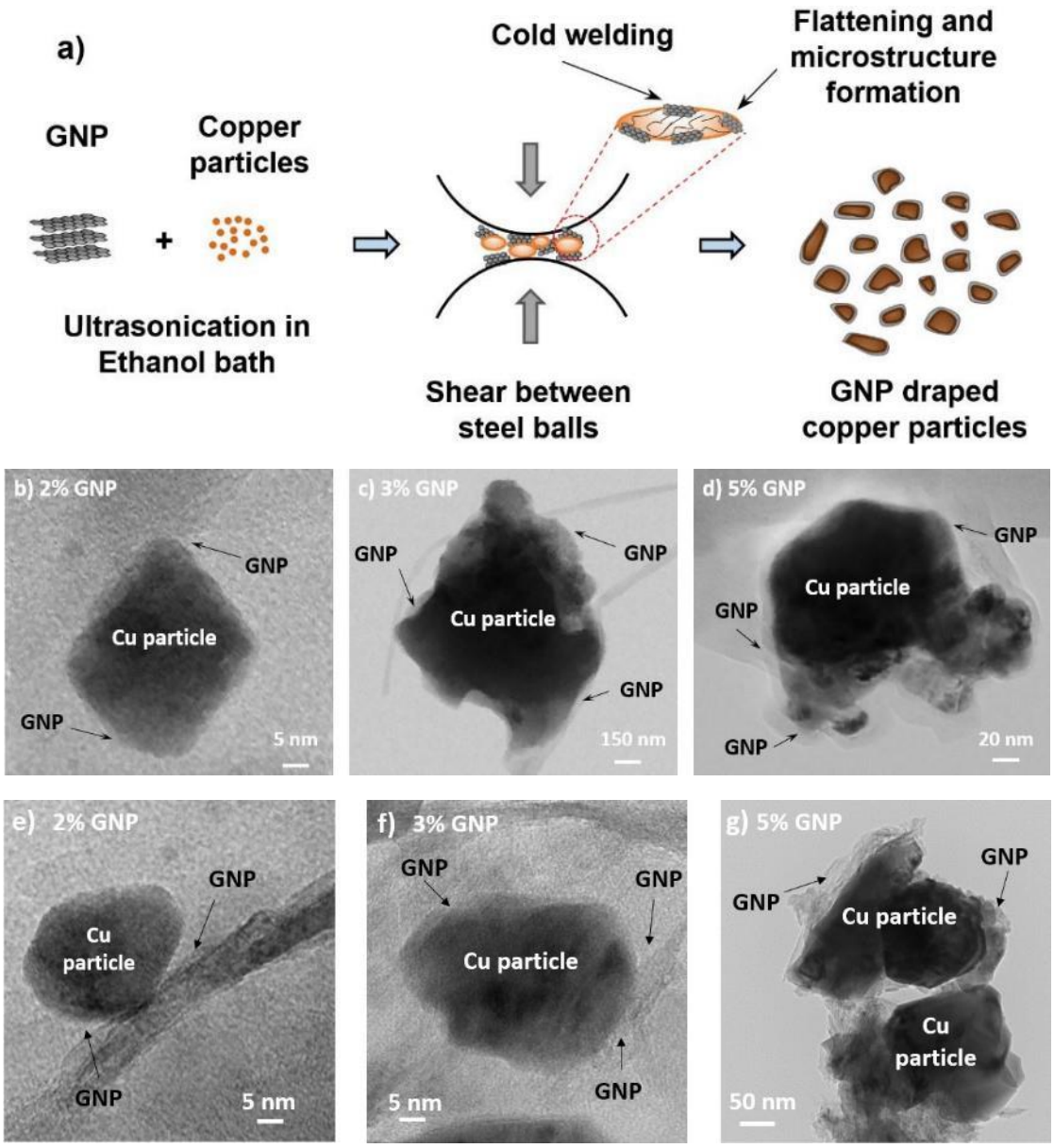

Figure 46. a) Schematic representing the mechanism of GNP-draped-copper particles via ball milling, transmission electron microscopy images of 20 µm (b, c, d) and 45 µm (e, f, g) copper particles draped with 2% GNP, (b, e), b) 3% GNP (c, f), and c) 5% GNP (d, g)

The flattening of the particles during the ball milling process is validated via transmission electron microscope (TEM) images shown in Fig. 46e, 46f, and 46g. A smaller number of layers were draped around the copper particle for 2% GNP. With the increase in wt. % of GNP, additional layers were draped around the copper. The energy

dispersive spectroscopy plot of the TEM images also indicated the increment in carbon peak intensity with increment in GNP concentration (Figure 47).

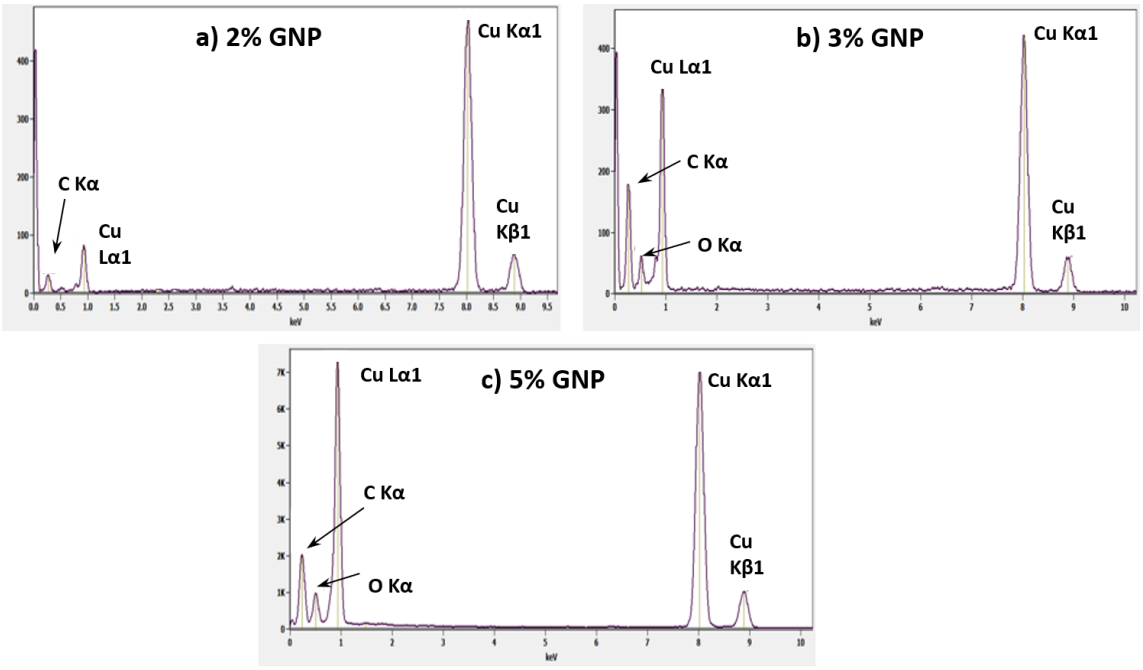

Figure 47: Energy dispersive spectroscopy images of TEM analysis showing carbon and copper peaks for GNP draped copper particle a) 2% GNP, b) 3% GNP, and c) 5% GNP

Figure 48 a-c show the scanning electron microscope (SEM) images of ball milled 45 µm copper particles at 2, 3, and 5 wt.% GNP concentrations. A higher concentration of GNP in the mixture resulted in the draping of additional layers of GNP on copper particles which is shown in Fig. 48 a-c, with red arrows indicating the direction of elemental analysis of the particles. A detailed elemental analysis shows an increment and stabilization of GNP and copper peaks in the direction of the arrow. The stabilization of the GNP peak further confirmed the draping of GNP around the copper particles. The increment in GNP peak intensity resulting from draping of additional layers due to increased wt. % of GNP was

further confirmed using Raman spectroscopy analysis (discussed in the next sub-section, Fig. 54e).

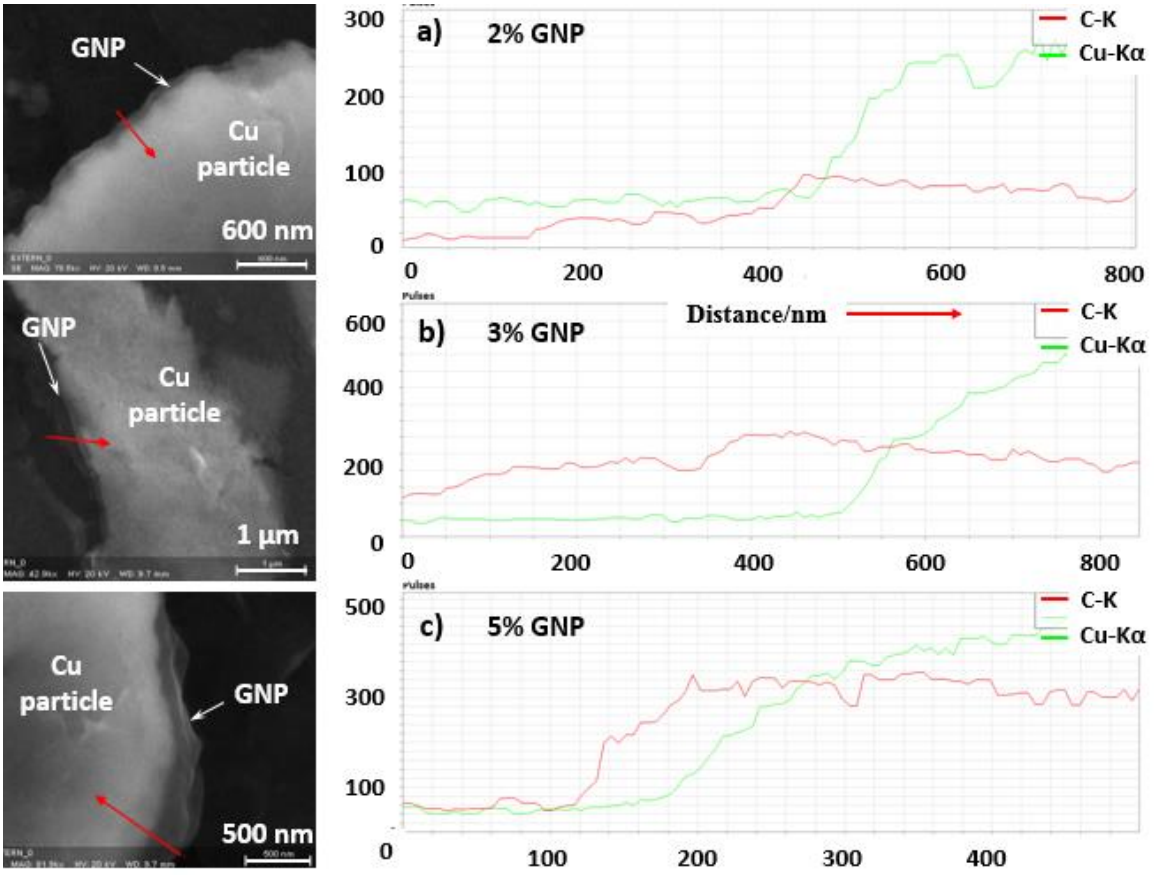

Figure 48. Elemental analysis of GNP draped copper particles indicating the increment followed by saturation of carbon peaks in the direction of red arrow a) 2% GNP, b) 3% GNP, and c) 5% GNP

STEM analysis was performed on GNP draped copper particles to understand the distribution of graphene on the individual copper particle. Figures 49a and 49b show the STEM images of 3% and 5% GNP particles along with copper and carbon mapping on the particle. The presence of carbon traces over the entire particle is indicative of the GNP draping around the copper particle.

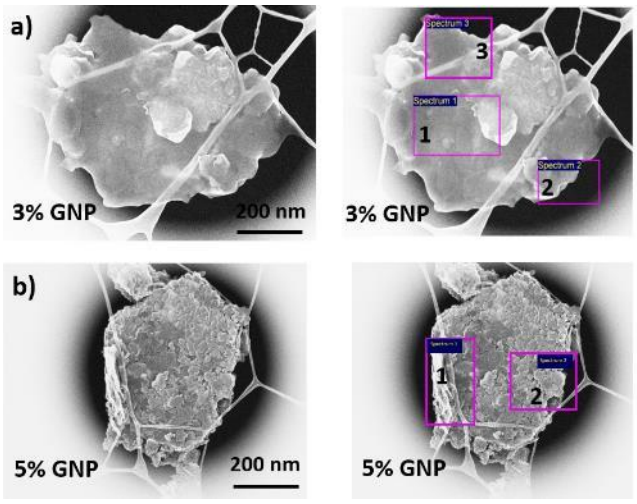

Spectrum	C	O	Cu	Total
Spectrum 1	7.89		92.11	100.00
Spectrum 2	20.42		79.58	100.00
Spectrum 3	73.48	5.83	20.69	100.00

Spectrum	C	O	Cu	Total
Spectrum 1	60.06		39.94	100.00
Spectrum 2	36.84		63.16	100.00

Figure 49. STEM images showing the GNP draping around 20 µm copper particles along with carbon and copper mapping e) 2% GNP, f) 3% GNP, g) 5% GNP

STEM images also showed surface morphologies of the GNP-draped-copper particles post ball milling, as shown in Fig. 50, revealing an escalation in surface roughness and the morphological changes that particles experience after ball milling owing to continuous collisions and trapping of particles between ball-to-ball and ball-to-wall. The morphology of the particles can be tuned by varying GNP concentrations and ball milling process parameters. Such microstructure alterations via chemical and structural inhomogeneity are highly desirable in pool boiling applications.

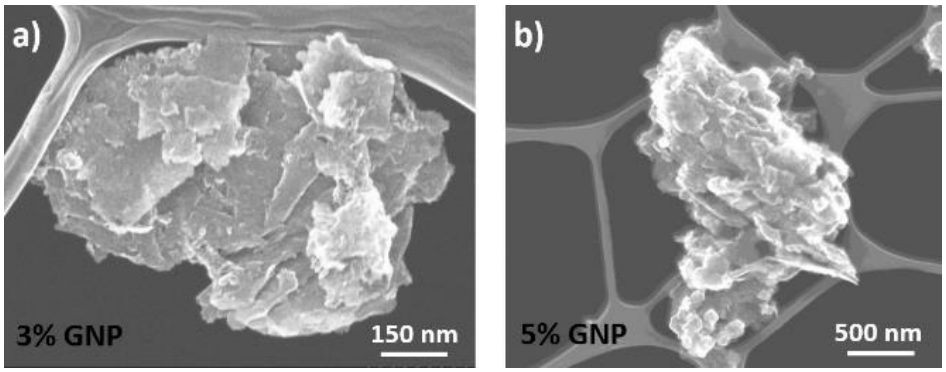

Figure 50. STEM images showing the GNP draping around 20 µm copper particle along with carbon and copper mapping e) 2% GNP, f) 3% GNP, g) 5% GNP

4.3.2.1.1 Porosimetry analysis:

Porosimetry is an analytical technique used to determine the various aspects and characteristics of a powder, such as pore size, pore volume, and surface area. The gas adsorption-desorption porosimetry technique typically uses nitrogen or argon gas to understand different characteristics of the powder. Adsorption refers to the accumulation of gas molecules at the interface regions of the surfaces of particles and in the pores. The surface area in gas porosimetry analysis is calculated using two methods, Langmuir and Brunauer–Emmett–Teller (BET), while average pore size and pore volume are calculated using Brunauer–Emmett–Teller (BET) and Barrett-Joyner-Halenda (BJH) methods. The gas is supplied in controlled increments in the closed chamber consisting of a powder with pressure (p) measured in-situ relative to the saturation vapor pressure (p_0) of the gas. The pressure is allowed to equilibrate, and the corresponding adsorbate quantity is calculated at each pressure and temperature. With an increase in pressure, the coverage of adsorbed molecules increases to form a monolayer. Langmuir and BET methods calculate the surface area based on monolayer gas molecules adsorption. The gas is supplied until the pores are completely filled, signified by $p/p_0 = 1$. Afterward, the pressure is again reduced until the relative pressure ratio $p/p_0 = 0$, and this process is called desorption.

The porosimetry of the ball milled Cu-GNP powders were measured using a porosimetry analyzer (ASAP 2020, Micromeritics Instrument) with nitrogen gas adsorption and desorption at 77 K. All three samples were outgassed at 250°C for 4 hrs. prior to the measurement to remove the contaminants. Figure 49 shows the isotherm plots for the three powders (20 µm Cu-2% GNP, 3% GNP, and 5% GNP). For all three samples, weaker hysteresis loop effects were observed, ensuring minimal losses and errors in the

results. Similar hysteresis loops were observed in the literature [67], which suggests that the slit-shaped pores are observed in all three samples used in this study. The maximum volume adsorption for the 5% GNP-draped-Cu powder indicated the maximum available pore area compared to 3% and 2% GNP samples (Fig. 51). Since the volume fraction of the nanopores is very small and micro-pores occupy a significant fraction of the pore volume post sintering, the combination of these nano- and micro-sized pores assists in enhancing the effective liquid supply during the pool boiling.

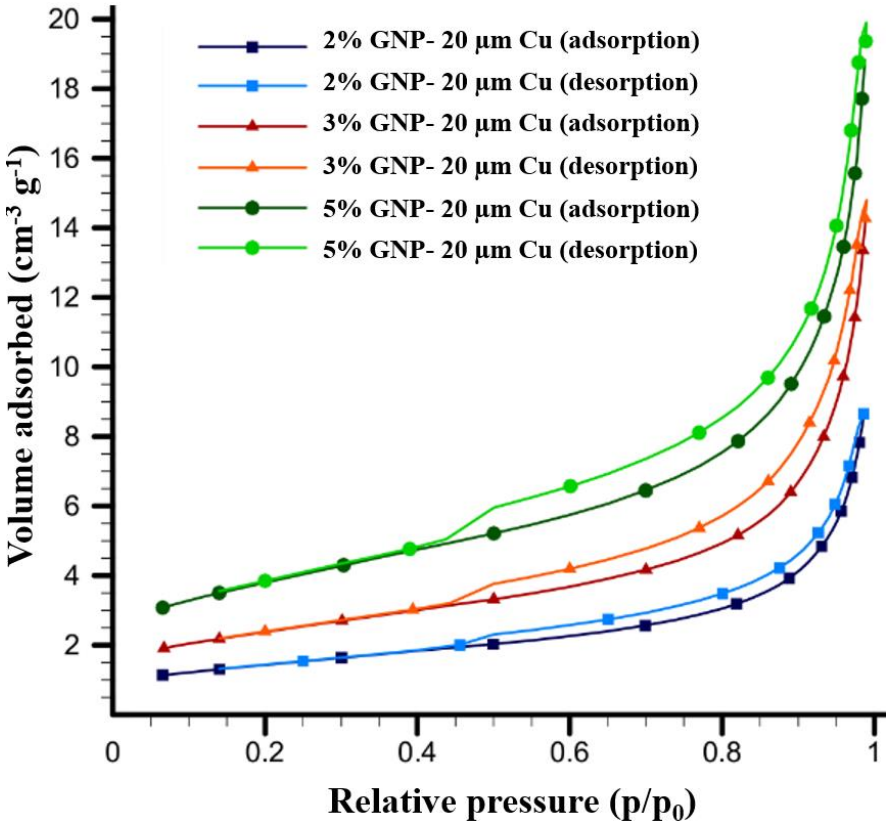

Figure 51: Porosimetry analysis of different GNP concentration ball milled powders

Table 11 summarizes the measured results of surface area, pore volume, and average pore size for all three samples. 5% GNP- 20 µm copper sample shows the highest

values of the surface area in both BET (13.24 m^2/g) and Langmuir methods (18.6 m^2/g). 5% GNP sample also shows the highest pore volume of 0.027 cm^3/g and 0.03 cm^3/g in both BET and BJH methods, respectively. On the other hand, 2% GNP- 20 µm copper sample shows the lowest values for the surface area and pore volume size. Results from table 11 indicate that despite distinct differences in surface areas and pore sizes of the three samples, the average pore sizes of all the samples are the same in the nanoscale range.

Table 11. Surface area and pore characteristics of GNP-draped-copper powder samples

Sample Name	**Surface Area (m^2/g)**		**Pore Volume Size (cm^3/g)**		**Average Pore Size (nm)**	
	BET	Langmuir	BET	BJH	BET	BJH
2% GNP- 20 µm Cu	5.09	7.09	0.012	0.0137	9.516	10.93
3% GNP- 20 µm Cu	8.38	11.76	0.0206	0.0227	9.856	11.85
5% GNP- 20 µm Cu	13.24	18.59	0.0274	0.0302	8.28	10.58

4.3.2.1.2 Thermogravimetric analysis (TGA):

TGA is a technique used to monitor the change in mass of a material (typically powders) as a function of temperature in an inert atmosphere. The stability of the material with a rise in temperature is determined, and the change in mass is recorded over a wide

temperature range. The reduction in mass typically corresponds to chemical reactions, and these gaseous byproducts are removed in TGA.

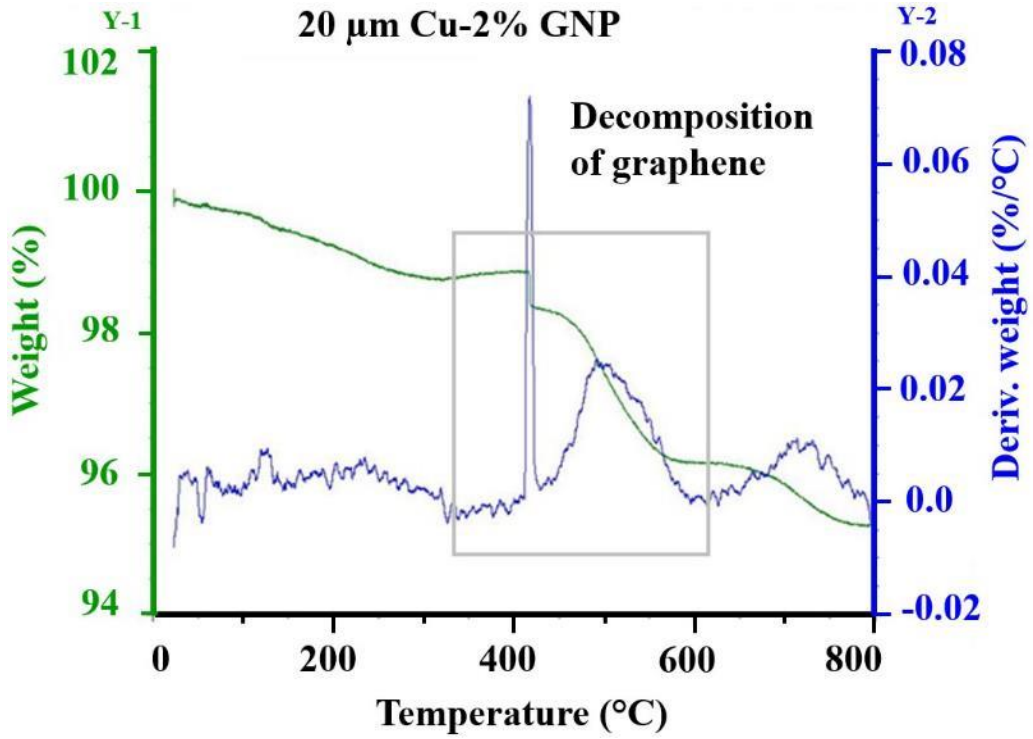

Figure 52: Thermogravimetric analysis of 20 µm Cu-2% GNP ball milled powder indicating the stability of powder with temperature

Thermogravimetric analysis (TGA) shown in Fig. 52 confirmed the presence of graphene as a decomposition between 400-600°C that corresponds to the degradation of unstable carbon constituent of graphene [68]. Derivation weight plotted on Y-2 axis provides the information related to the temperature at which the mass loss occurs. Thus, a sharp peak at ~420°C indicates the mass loss followed by a small mass loss peak between ~470°C to 550°C. It is important to note that the mass loss between the temperatures 400°C–600°C is negligible (0.07% and 0.02%) and the decomposition is of only unstable carbon, oxygen, hydroxyl, and carboxyl-based functional groups. Literature studies have also indicated the similar decomposition of graphene to indicate the thermal stability of

graphene [69,70]. Additionally, sintering techniques for deposition with graphene-based coatings with temperatures up to 1000°C have been studied [71]. This indicates that graphene-based composite coatings can yield stable coatings and stability of graphene nanoplatelets during pool boiling studies.

4.3.2.1.3 Fourier transform infrared (FTIR) spectroscopy analysis:

Fourier Transform Infrared (FTIR) spectroscopy is an optical analytical technique used to identify the organic and inorganic compounds present on the surface. FTIR passes infrared radiation through samples, and a detector plots the peaks of absorbance v/s wave number of the radiation. All matter contains molecules and molecules have bonds. These bonds continually vibrate and move around when they are in a ground state. When these molecules are exposed to the radiation of the exact same frequency as the energy difference between the ground state and excited state, they get promoted to an excited state. Hence, there is a designated wavenumber for a bond that absorbs that wavelength and thus, the peak intensity in terms of absorbance is observed.

Figure 53 illustrates the Fourier transform infrared (FTIR) analysis for 2%, 3%, and 5% GNP surfaces to support the association of GNP with copper particles through characteristic peaks of GNP-based functional groups. The peaks include aromatic rings (C=C) at 1570 cm^{-1}, stretching vibration C=O of carboxyl groups at 1630 cm^{-1}, O-H deformation vibrations resulting from C–OH at 1310 cm^{-1}, and C–O–C stretching vibration at 1200 cm^{-1}. A summary of the peaks, their corresponding frequency region, and their structural description is provided in Table 12.

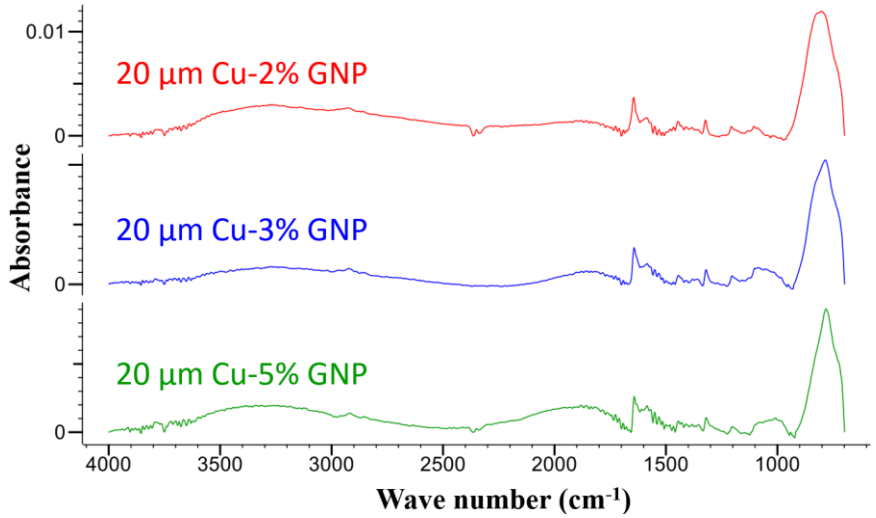

Figure 53: Fourier transform infrared spectroscopy analysis of different GNP concentration ball milled powders

Table 12: Functional groups of GNP-Cu sintered surfaces showing respective absorption frequencies for FTIR (Fourier transform infrared) spectra

Functional group	Absorption frequency	Description
C=C	1590	Stretch-Aromatic structure
C=H	752	Bend-Alkenes, Aromatic
	2900	Stretch-Alkanes, Aldehydes
C-O-H	1310	Stretch-Alcohol
	2350	Stretch-Aldehyde
C=O	1630	Stretch-Ketones
C-O-C	1200	Stretch-Ester

4.3.3 Scanning electron microscope (SEM) and Raman spectroscopy analysis of ball milled + sintered GNP-Cu coatings:

SEM images demonstrate the formation of variable morphologies with open hierarchical porous networks. EDS mapping on all the surfaces confirms the presence of GNP throughout the substrate along with copper particles. Typically, sintering and electrodeposition techniques form fairly circular pores. However, in addition to circular pores, the coatings developed via ball milling followed by sintering demonstrated the unique morphological structures forming the rectangular porous cavities which are termed as "pore pockets" in this work. After performing an ImageJ analysis of the SEM images of the surfaces, compared to 2% GNP-20 μm copper coating (~17) (as indicated in Figure 54b), the number of pore pockets for 3% GNP-20 μm copper coating (~10) and 5% GNP-20 μm copper coating (~13) was less. It is believed that these pore pockets act as liquid supply pathways providing higher wickability to the coatings.

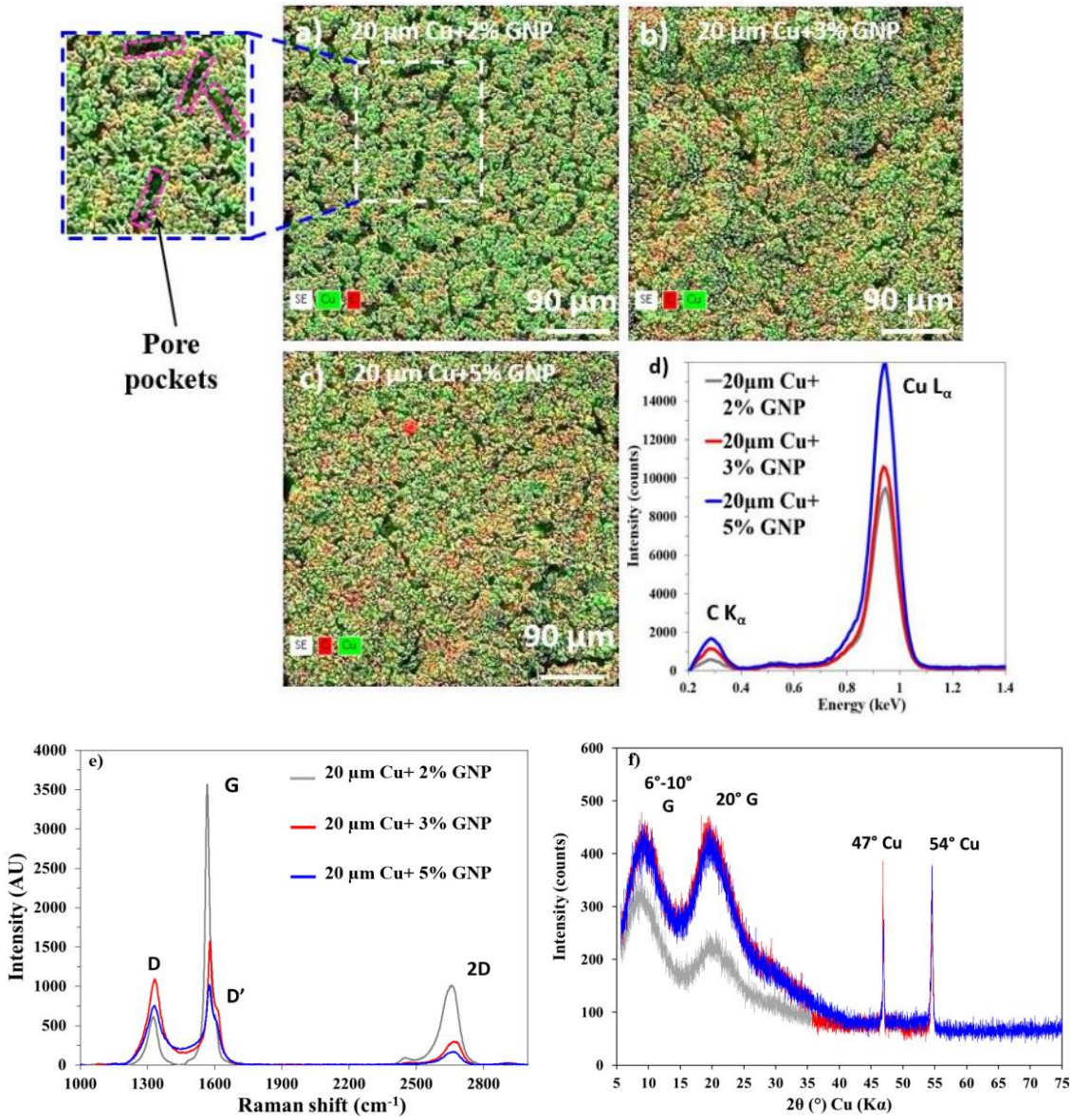

Figure 54: Scanning electron microscope (SEM) image of 2% GNP draped around 20 µm copper particles after ball milling at 500X magnification of GNP draped 20 µm copper coatings showing carbon and copper mapping with a) 2% GNP, b) 3% GNP, c) 5% GNP, d) energy dispersive X-ray spectroscopy (EDS) analysis, e) comparison of Raman spectra and, f) X-ray diffraction analysis of 2, 3, and 5% GNP draped copper surfaces

Raman spectroscopy was used to quantify the number of graphene layers corresponding to each GNP concentration added with the copper particles during the ball milling. Figure 54e demonstrates the distinct graphene peaks – G at 1580 cm^{-1}, and D at

1340 cm^{-1}, that correlate to the in-plane vibration of sp^2-hybridized carbon atoms and degree of disorder of sp^3-hybridized carbon structure, respectively [72,73]. G and 2D peak intensities (IG/I2D) ratios from the Raman spectroscopy plot were used to find the number of deposited graphene layers [74–76]. 5% GNP coating deposited the maximum number of graphene layers (~7), while ~6 and ~4 layers were deposited for 3% and 2% GNP coatings, respectively. An additional small peak D' at ~1610 cm^{-1} was observed for all the three samples, which is attributed to the intra-valley double resonant Raman process in which the defects provide the missing momentum to satisfy the momentum conservation in a Raman scattering process [77]. The intensity ratio I_D/I_G of Raman spectra is typically used to identify the defects and damage degree of the graphene sheets. We observed an increase in I_D/I_G ratio from 0.18 to 0.76 with an increment in GNP wt. % from 2% to 5%. The lower value of I_D/I_G ratio in 2% GNP coating suggests that the crystal structure in 2% GNP coating is more preserved post ball milling. The increased defect ratio of the samples can be attributed to the higher disordering of the GNP sheets due to the increased number of collisions between stainless-steel balls and the GNP resulting from an additional quantity of GNP. However, despite the increment in I_D/I_G ratio for all three samples, the ratio less than 1 indicated fewer defects and good quality of GNP deposition. The implementation of an hour of cooling cycle after every 15 minutes of ball milling enabled a short annealing cycle which relieved the internal stresses and defects of GNP. 2D peaks transitioned from a sharp profile to a broader peak with the increasing number of layers which arises from the stacking between the layers [78].

4.3.3.1 Comparison of ball milled followed by sintered surfaces with different GNP concentration:

To optimize the GNP concentration for pool boiling, the pool boiling performance of different wt. % GNP surfaces were quantified. Table 13 shows the comparison of CHF and HTC for the coatings developed with three different GNP concentrations 2, 3, and 5% considered during ball milling with 20 µm copper particles.

Table 13. Comparison of pool boiling performance for the ball milled followed by sintered coatings for different GNP concentrations

Sample preparation method	**GNP concentration**	**CHF (W/cm²)**	**Wall superheat temperature (°C)**
Ball milling followed by sintering with 20 µm Cu particles	2%	239 ± 9.3	8.3
	3%	203 ± 8.2	18
	5%	200 ± 8	13.5

Figure 55 shows the pool boiling plot and the heat transfer efficiencies of these three surfaces. For 2% GNP-20 µm copper coating, after certain heat flux, a reduction in wall superheat temperature was observed with increased heat flux, a phenomenon also termed as "Boiling Inversion" [79]. This phenomenon is because of the formation of micro-scale morphological features on the coating and excessive active nucleation sites evolving from wickability, tunable porosity, and formation of the thermal gradient across the microstructure of the coating.

The maximum heat transfer coefficient of 285 kW/m²-°C was attained for 20 µm Cu-2% GNP coating, while that for the 20 µm Cu-3% GNP and 20 µm Cu-5% GNP coatings was 113 kW/m²-°C and 148 kW/m²-°C, respectively. A very low wall superheat is achieved by virtue of uniform spreading of GNP on the boiling surface and draping of GNP around copper particles. This is reflected in larger heat transfer coefficients indicating extremely high efficiencies of GNP-draped-Cu surfaces. A detailed enhancement mechanism of the coatings is explained in the following section.

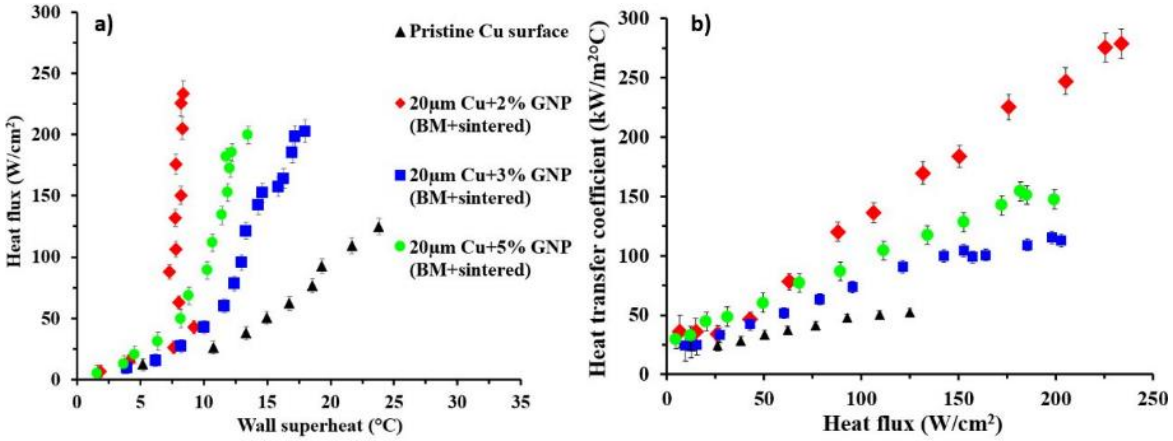

Figure 55. Comparison of effect of different GNP concentration during ball milling on pool boiling performance showing a) Heat Flux vs wall superheat depicting pool boiling regimes, b) heat transfer coefficient vs heat flux summarizing heat transfer performance

The primary pool boiling enhancement factor in these coatings is the increased thermal conductivity of the coating. The thermal conductivity of a few layered graphene (2-4 layers) lies in the range of ~2500 W/m-K to ~3000 W/m-K. It reduces to ~2000 W/m-K with the increment in the number of deposited graphene layers (in most cases, greater than 4 layers) [80,81]. In this work, ~4 layers of graphene were deposited for 2 wt. % GNP coating (calculated from Raman spectroscopy analysis), while for 3% and 5% GNP coatings, ~6 and ~7 layers were deposited. With ball milling, draping of GNP on individual

copper particles occurs and sintering with this powder increases in-plane thermal conductivity of the coatings. And since the thermal conductivity of coatings plays an important role in lateral dissipation of heat in the thin film developed under a growing vapor bubble, this increment in thermal conductivity of the coatings contributed to the enhancement of the CHF and HTC. Thus, the number of deposited GNP layers has a significant impact on contribution to pool boiling performance enhancement. Owing to the minimum number of deposited GNP layers, 2% GNP coating showed the maximum enhancement CHF and HTC compared to 3% and 5% GNP coatings. Additional enhancement mechanisms established for these coatings are discussed as follow:

4.3.3.1.1 Enhancement mechanism for improved CHF and HTC: Variable morphologies and increased wickability due to GNP-draped-Cu particle deposition:

A detailed morphological study was conducted to comprehend the enhancement mechanism for the pool boiling performance of the ball milled followed by sintered coatings. Commonly, circular pores are formed with sintered copper surfaces. However, in this work, in addition to circular pores, sintering with ball milled powders yielded rectangular pores with favorable pore pocket sizes that served as liquid pathways allowing maximum vapor departure. For 20 µm Cu-2% GNP coating, post ball milling, the pore pockets were ~32 µm long and ~7.4 µm wide (Figure 56 a), using ImageJ software, while 20 µm Cu-3% GNP and 20 µm Cu-5% GNP coatings produced pore pockets of ~40 µm × 6 µm wide and ~47 µm × ~15 µm respectively (Figure 54b and 54c).

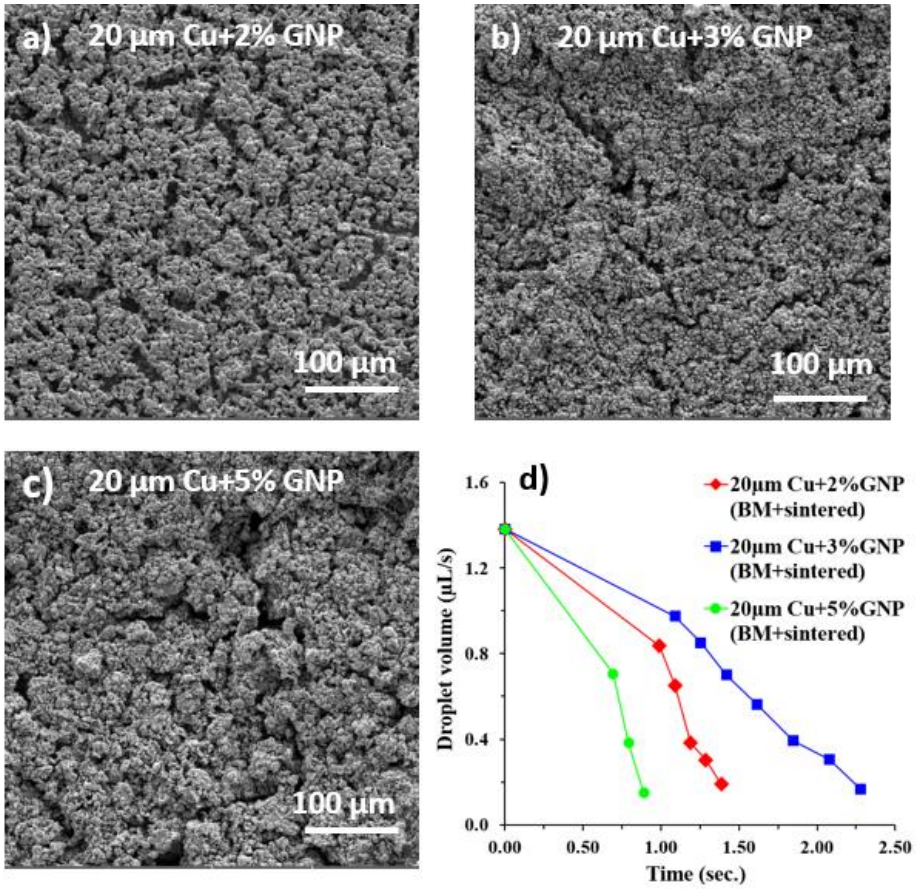

Figure 56. Scanning electron microscope (SEM) images at 500X magnification of 20 µm copper particles coatings with a) 2% GNP, b) 3% GNP, c) 5% GNP, and d) comparison of change in water droplet volume for 2, 3, and 5% GNP coatings

In addition to the microporous structure, the overall enhancement in pool boiling performance is also attributed to wickability and the number of deposited GNP layers. Initially, the wetting properties of the coatings were determined by measuring the contact angles. After measuring the contact angles of these surfaces using a Goniometer, it was found that all the coatings were superhydrophilic (0° contact angle). Thus, the wicking rates of the coatings were used for the comparison. Figure 56d compares the propagation of water droplets in terms of the change in droplet volume with respect to time for the different GNP concentration substrates that correlates to the wickability of the coatings. One of the factors responsible for the increment in wickability of the coatings is the

increment in deposition GNP layers on the surfaces. Based on the Raman studies shown in Figure 54e, the highest number of GNP layers were deposited for the 5% GNP coating, which reflected in achieving the highest wicking rate for the 5% GNP coating. However, due to a small number of optimum-sized pore pockets on the surface (~12 for 5% GNP compared to ~17 for 2% GNP), CHF for 5% GNP surface was lower than 2% GNP surface. A large wicking rate of 5% GNP surface contributed to reducing a wall superheat temperature more effectively than 3% GNP surface. Since pool boiling is a highly complex phenomenon, the combined effect of several factors such as wickability of the coating, optimum size and geometry of the pores, and a number of deposited GNP layers decide the pool boiling performance. When comparing the performance of 2% and 3% GNP coatings, although more GNP layers (Figure 54e, ~6 layers) were deposited for 3% GNP surface when compared to 2% GNP surface (Figure 54e, ~4 layers), significantly less pore pockets were formed for 3% GNP surface (~7 for 3% GNP as against ~17 for 2% GNP). Hence, the reduction in the CHF and increment in wall superheat for 3% GNP surface than 2% and 5% GNP surfaces.

Critical heat flux models of wicking microstructures to estimates the CHF values have been studied in the literature. Rahman et al. [21] have demonstrated the effect by introducing a wicking number (Wi), which correlates to CHF increment.

$$W_i = \frac{V_0" * \rho_l}{\sqrt{\rho}_v * [\sigma * g * (\rho_l - \rho_v)]^{1/4}} \qquad (14)$$

Where, $V_0"$ is the wicking rate, ρ_l and ρ_v are liquid and vapor densities, g is the acceleration due to gravity, and σ is the surface tension.

The wicking rate measured in this analysis is different from the method provided by Rahman et al. [21]. The wicked volume (mm^3/s) was estimated as the droplet volume

change over time using VCA Optima Goniometer. The wicking rate (mm/s) was then calculated by normalizing the wicked volume over the droplet impingement area. Using this method, the wicking number W_i was estimated and CHF was estimated using Zuber's limit [21]:

$$\frac{q''_{CHF,W}}{q''_{CHF,Zuber}} = 1 + W_i \qquad (15)$$

Where, $q''_{CHF,W}$ is the CHF of the wicking structure and $q''_{CHF,Zuber}$ = 111 W/cm². Based on this, CHF of GNP coatings was estimated. Wicking rates for 2%, 3%, and 5% GNP coatings were 1.46 mm/s, 1.36 mm/s, and 1.63 mm/s, respectively. This translated into CHF values of 152.4 W/cm², 149.6 W/cm², and 157.2 W/cm² for 2%, 3%, and 5% GNP coatings, respectively. Compared to experimental values, these CHF values are much less, indicating that the wicking is not the dominant factor responsible for the enhancements. Performance primarily depends on thermal conductivity as discussed in the results paragraph. High-speed image analysis also provides an insight on bubble behavior and dynamics on different GNP wt. % surfaces which is discussed below.

4.3.3.1.2 Bubble dynamics study using high-speed images for different GNP concentration surfaces:

To understand the role of the bubble dynamics in deciding the overall pool boiling performance, high-speed images during pool boiling on different GNP concentration surfaces were captured and analyzed to correlate with the enhancements obtained. The nucleation, growth, and departure patterns of vapor bubbles usually assist in correlating the obtained pool boiling performance. Typically, the surfaces with vapor bubbles of smaller departure diameters and less departure time yield higher pool boiling performance as they contribute to delaying the vapor blanket formation. High-speed images for 2%, 3%, and

5% GNP coated surfaces obtained at a heat flux of ~15 W/cm² were captured using a Photron Fastcam high-speed camera as summarized in Figure 57 a-c. The bubble dynamics observation was conducted on the plain copper surface to create a baseline. The total time taken for a single bubble to nucleate, grow, and depart was 13.25 ms for the plain copper surface. Figure 57d compares the progression of bubble diameters measured during nucleation, growth, and just before the departure from the nucleation cavity as a function of time for a plain copper surface, 2%, 3%, and 5% GNP coatings.

Owing to the existence of microporous cavities on the boiling surface as a result of ball milling followed by the sintering process, the high-speed images indicate rapid bubble growth on 2%, 3%, and 5% GNP coatings compared to the plain copper surface. The total time required for a bubble to depart from the plain copper surface was 13.25 ms and attained the bubble departure diameter was 2.1 mm. The smallest bubble departure diameter of 0.81 mm and the shortest departure time of 8 ms were recorded for the 2% GNP coating. For 3% GNP coating and 5% GNP coating, the departure diameters were 1.12 mm and 0.89 mm, with the departure time of 12 ms and 14 ms, respectively. Attributing to multiple contraction and expansion of bubbles before departure, the increased time of departure from the nucleation cavities was recorded for 3% and 5% GNP coatings and subsequently reflected as a reduction in the CHF and HTC as compared to 2% GNP coating.

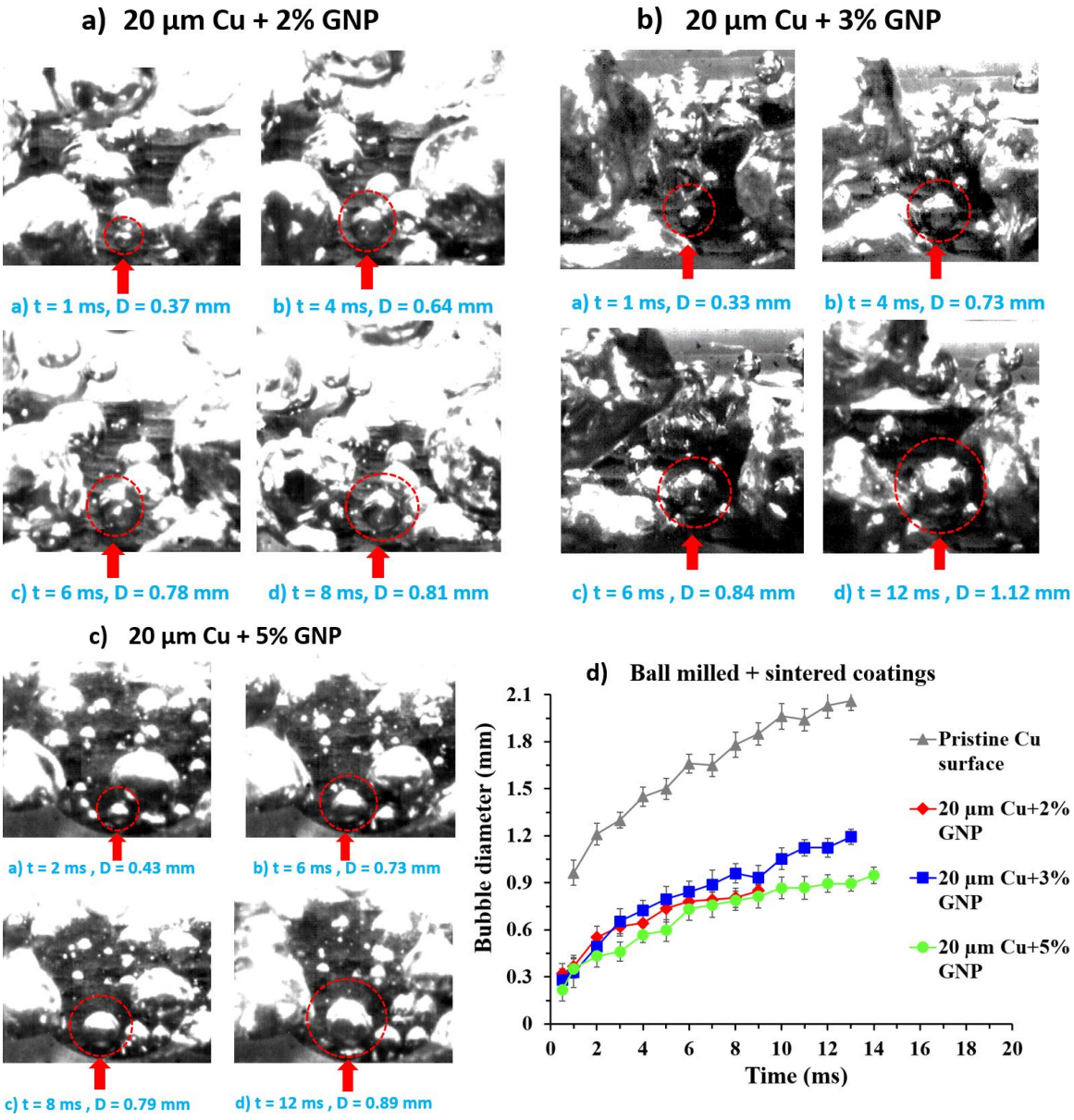

Figure 57. a), b), c) Nucleation, growth, and just before departure bubble diameter comparison for the 20 µm copper with 2, 3, and 5% GNP coatings, d) comparison of progression of bubble diameters with respect to time on different GNP-Cu surfaces

Optimum pore sizes of ~32 µm × ~7.4 µm were achieved for 2% GNP-20 µm copper coating, which led to the formation of the smallest bubble departure diameter. This further contributed to procuring the highest pool boiling performance. Additionally, it is observed that even though the total bubble cycle time for the 5% GNP-20 µm copper coating was 14 ms, the smaller bubble diameters enabled delayed vapor blanket formation

and thus achieving higher CHF. Thus, the boiling surface temperature is directly dependent on the number of active nucleation sites and is a function of the rapidness of the vapor bubble departure from the surface. This in turn, allows the liquid to rush into the nucleation cavities and maintain lower surface temperature. Conclusively, the lowest bubble departure diameter and departure time were observed for 2% GNP coating, which maintained the lowest wall superheat and highest HTC, followed by 5% GNP coating and 3% GNP coating. This indicates that bubble dynamics is also one of the enhancement mechanisms and alter CHF and HTC of the coated surfaces.

4.3.3.1.3 Effect of active nucleation sites:

In addition to bubble departure diameter and total time, active nucleation sites for the vapor bubbles also play a critical role in deciding the surface temperature and thus the heat transfer coefficients (HTC). Since at higher heat fluxes (> ~20 W/cm²), owing to chaotic and rapid boiling, the visualization of the vapor bubbles departing from the boiling surface becomes difficult, the analysis of active nucleation sites was performed at heat flux ~15 W/cm². Figure 58 a, b, and c show the available active nucleation sites for all three GNP wt. % surfaces. It is observed that 5% GNP coating produced more active nucleation sites than 2% GNP and 3% GNP coatings, resulting in lower wall superheat. Figure 58 d shows an enlargement of a small section of the pool boiling curve (up to heat flux ~60 W/cm²) that compares the wall superheat temperatures of the different GNP wt. % surfaces. Initially, 5% GNP coating produced the lowest wall superheat due to higher nucleation sites. However, with increasing heat flux, the wall superheat temperature was increased to ~9°C. After the measured heat flux ~50 W/cm², "Boiling Inversion" phenomenon was observed for 2% GNP-20 μm copper coating, which showed a significant reduction in the

wall superheat temperature with increment in heat flux. At favorable wall superheat temperature, the number of active nucleation sites increase resulting in excessive heat removal, thereby drastically reducing the wall superheat temperature.

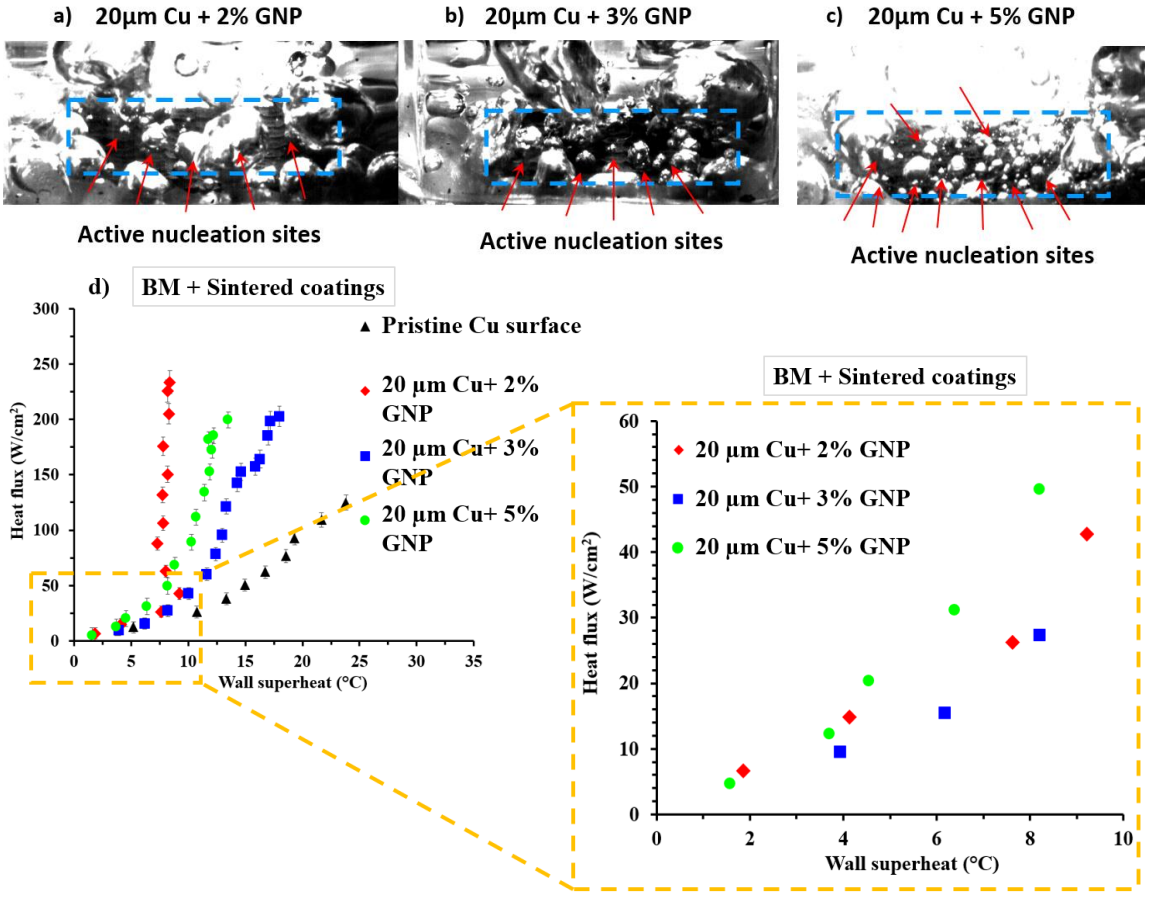

Figure 58. a, b, c) high-speed images for 2, 3, and 5% GNP coated surfaces showing the number of active nucleation sites, and d) pool boiling curve for 2, 3, and 5% GNP coated surfaces showing the enlarged section till ~60 W/cm² heat flux

4.3.3.1.4 Durability study and comparison of pool boiling performance with literature:

To confirm the reproducibility of the results, two different samples of 2% GNP-20 µm Cu test surface were prepared from separately manufactured ball milled powders. A close match in the pool boiling test results of these surfaces confirmed the reproducibility of the ball milling followed by the sintering technique used in this work. CHF values

obtained for both the test were 239 W/cm² and 237 W/cm² at wall superheats of 8.3°C and 7.5°C. Three repetitive pool boiling tests were conducted on the best performing test surface, i.e., 2% GNP-20 µm-copper coating. Figure 59a shows the pool boiling curve representing the repetitive pool boiling tests (R1 represents the first repetitive test and so on). At the end of the third repetitive pool boiling test (R3), a CHF of 226 W/cm² was attained at the wall superheat of 10.4°C. A significant deterioration of the pool boiling heat transfer performance was not observed, indicating the strong adhesion between the coating and the substrate.

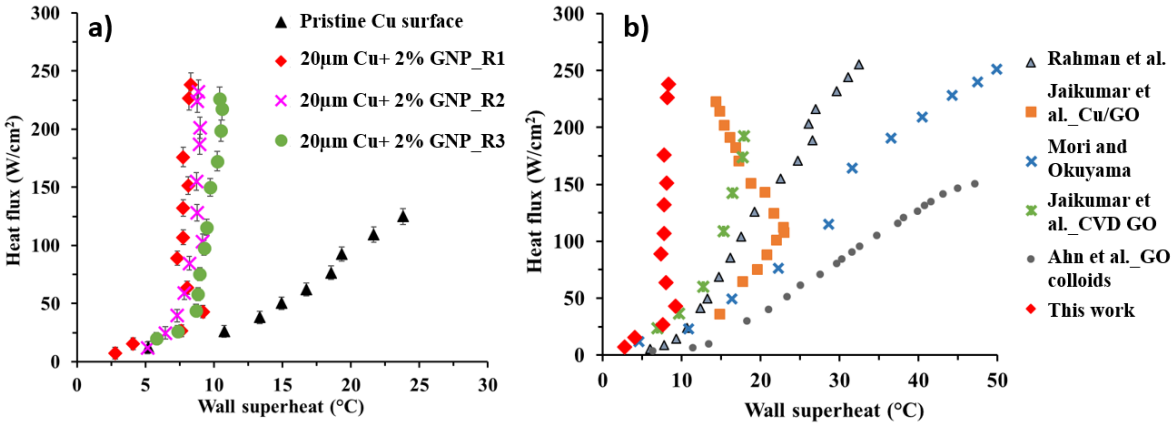

Figure 59. Pool boiling curves showing a) Repetitive testing (R1 – repetitive pool boiling test 1), b) Comparison of the current work with the existing literature

In the recent years, various techniques have been developed to coat graphene-based coatings owing to very high thermal conductivity of graphene. To compare the performance of the present work with the literature, the pool boiling curve, as shown in Fig. 59b, was plotted. The CHF achieved using the sintered surface developed from ball milled GNP draped copper particles is slightly smaller as compared to the literature. Nonetheless, the wall superheat temperature attained by 2% GNP-20 µm-copper coating used in this work is the lowest (highest heat transfer efficiency) of any graphene-based

coatings available in the literature. Due to the current trend of miniaturization of electronic devices, maintaining a lower boiling surface temperature is extremely desirable in many electronic equipment and high-power electronic devices. The coatings developed using the ball milling and sintering methods described in this work can thus be immensely beneficial in enhancing the heat transfer efficiencies of the boiling surfaces.

4.4 Salt Templated and Graphene Nanoplatelets Draped Copper (GNP-draped-Cu) Composites for Dramatic Improvements in Pool Boiling Heat Transfer

Concept and hypothesis:

Typically, the pore sizes and porosity obtained via the sintering technique is uniform throughout the coating. Additionally, there is not control over the pore size developed via sintering. This drawback is overcome in this work by implementing the salt template-assisted sintering, in which, depending on the quantity and size of the salt pellets, porosity can be tuned for sintered coatings. This work presents a novel manufacturing approach to obtain surface-active coatings via a combination of sintering, salt-templating, and ball milling techniques to yield graphene nanoplatelets (GNP) draped sintered copper coatings displaying a hierarchical porous network with high wickability that produced very high heat fluxes at lower surface temperatures. The porosity can be tuned via salt-templating during the sintering process. GNP were selected owing to their high surface area and thermal conductivity and their concentration in the coatings were varied with respect to copper particles (by weight).

It was hypothesized that: i) GNP draped copper particles obtained via ball milling may yield inhomogeneous coatings with optimum roughness that will further promote surface wetting and wicking properties for boiling applications, ii) Salt templating may lead to tunable porous coatings with hierarchical pores which will allow a continuous passage of bubbles and liquid during the pool boiling process, iii) Varying concentration of GNP and copper particle diameter will remarkably affect the surface morphology and

related properties that are essential in achieving higher pool boiling performance compared to mono and multi-layered graphene.

4.4.1.1 Porous sintered GNP draped copper surfaces via ball milling and salt templated sintering

The GNP/copper coating was further improved by tuning the porosity and wickability of the surfaces using salt pellets as the templates during the sintering process. The schematic in Fig. 60 shows the overall salt templated sintering process. Precisely, sodium carbonate pellets were added to the ball milled GNP draped copper particles followed by sintering. Post sintering, the surface was rinsed thoroughly with distilled water to dissolve the salt pellets. Elemental analysis of the surfaces displayed no trace of salt on the surfaces before performing the pool boiling studies (see Fig. 60b). The thicknesses of the sintered coatings were measured using a laser confocal microscope and an average thickness of 65±3 μm was obtained after sintering for all the coatings.

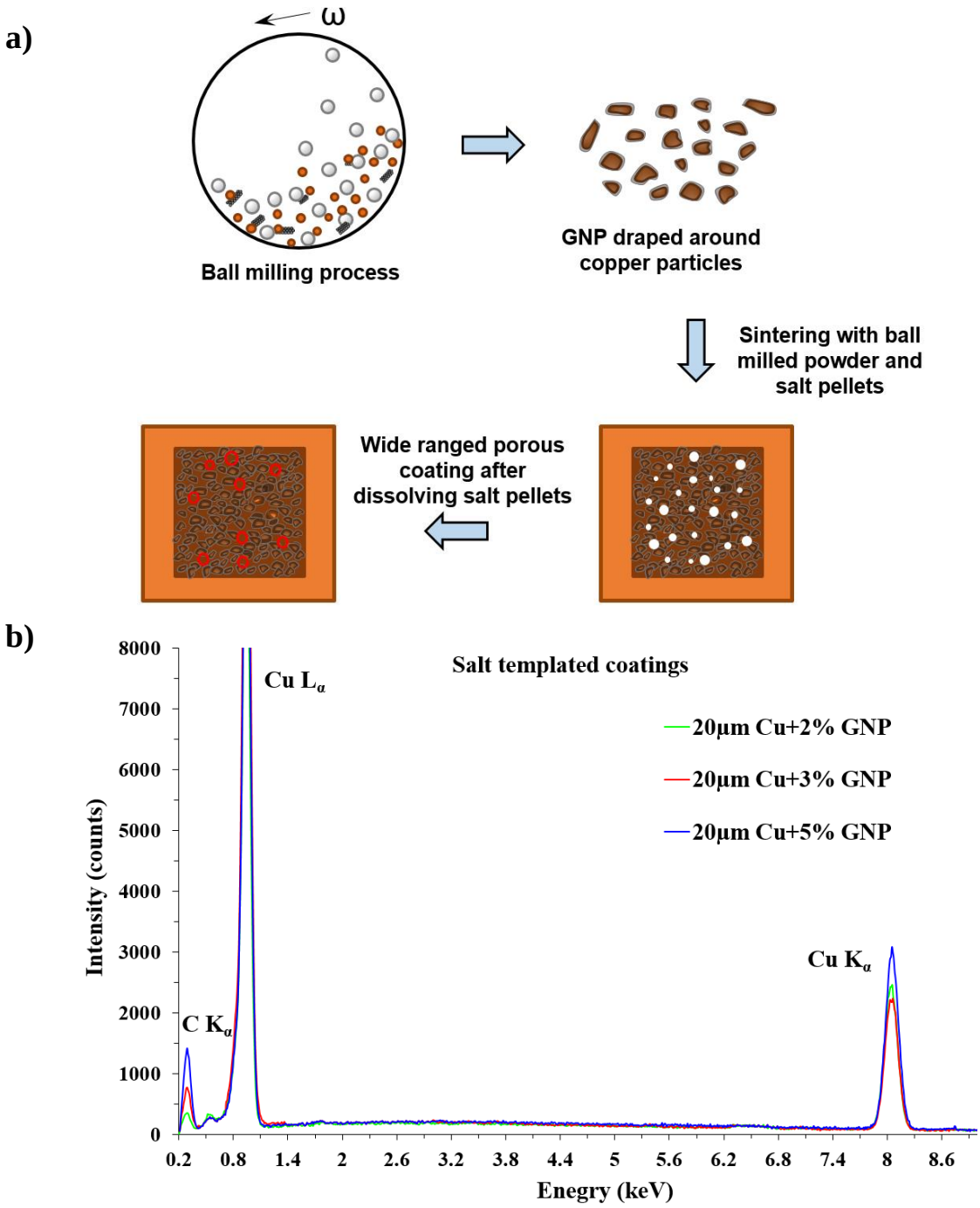

Figure 60. a) Schematic showing the development of coatings using salt templated sintering technique, b) Plot showing elimination of salt traces post salt templated sintering

4.4.1.1.1 Scanning electron microscope and Raman spectroscopy analysis of ball milled and salt templated sintered coatings:

SEM studies shown in Fig. 61 confirm the evolution of pores as a result of salt templating compared to the mere ball milled GNP-copper sintered surfaces. This was consistent for all the different weight ratios of GNP to copper particles. We established previously that the presence of hierarchical pores allows a continuous passage of bubbles and liquid via tunnel effect during the pool boiling process[30]. As shown in Figures 61 d-f a hierarchical porous network with pore diameters ranging from 2 μm to several hundred microns was achieved by salt templating. Coatings with 3 wt. % GNP (Fig. 61e) exhibited an open porous network with a larger number of pores compared to 2% and 5% GNP surfaces.

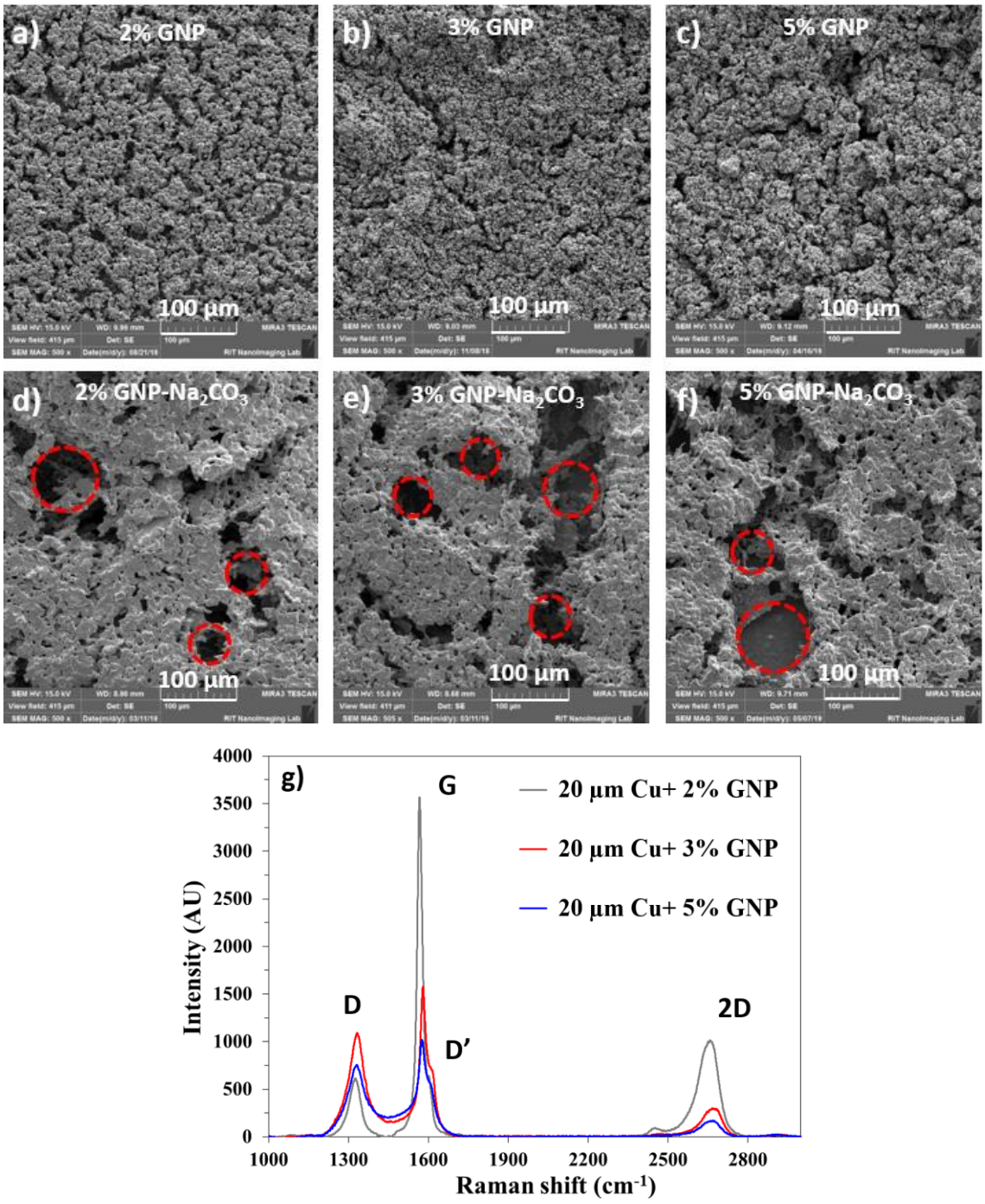

Figure 61. Comparison of scanning electron microscope (SEM) images of GNP draped 20 µm Cu coatings with a) 2%, b) 3%, and c) 5% by weight GNP and d) 2% GNP, e) 3% GNP, and f) 5% GNP via salt templating, and g) Raman spectroscopy analysis of different wt. % GNP draped copper coatings

Raman spectroscopy further confirmed the deposition of graphene nanoplatelets (GNP) layers on the copper particles and quantified the number of layers of GNP obtained as a result of varying concentrations of GNP. Figure 61g shows the typical G, D, and 2D peaks correspond to graphene correlating their in-plane vibrations of sp^2-hybridized carbon atoms and degree of disorder of sp^3-hybridized carbon structure[82][83]. The ratio of intensities of G peak to 2D peak (I_G/I_{2D}) yielded the number of deposited GNP layers for each GNP concentration. The intensity ratio I_D/I_G of Raman spectra is typically used to identify the defects and damage degree of the graphene sheets. The observed I_D/I_G ratio was less than 1 for all three samples indicating the fewer defects and good quality of deposited GNP. An increment in the number of deposited GNP layers was observed with an increase in wt. % of GNP. A maximum of ~7 layers were deposited for 5 wt. % GNP, while for 3 wt. % and 2 wt. %, the number of layers were ~6 and ~ 4, respectively.

For all the absorption peaks at D, G, and 2D, a slight shift of peaks toward the right was observed owing to the application of a higher wavelength of Laser (λ = 632.8 nm instead of λ = 514 nm), which has also been reported in the literature [84]. For all the samples, the absorption peaks for D and G bands were seen at ~1335 cm^{-1} and ~1580 cm^{-1}. An additional small peak D' at ~1610 cm^{-1} was observed for all three samples, which is attributed to the intra-valley double resonant Raman process, where the defects provide missing momentum to satisfy the momentum conservation in a Raman scattering process [84].

4.4.1.2 Enhanced heat transfer properties during the pool boiling process: Effect of salt templated induced porosity and GNP concentration

Pool boiling performance with regards to the maximum heat dissipated by boiling surface and the corresponding heat transfer coefficients was evaluated after characterization of the surfaces. Figures 62a and 62b show the comparison of pool boiling performance for 0%, 2%, 3%, and 5% GNP surfaces obtained via salt templating. A dramatic increment in CHF was observed for the combined ball milled and salt templated sintered surfaces. A maximum critical heat flux of 289 W/cm² was attained for 20 µm Cu-3% GNP surface, displaying approximately 131% enhancement in CHF compared to a plain copper surface. Furthermore, the wall superheat of just 2.2°C was achieved, indicating ~2390% improvement in HTC in contrast to a plain copper surface. These are the highest CHF and HTC values reported in the pool boiling literature for graphene-based and porous coatings coated on a plain copper surface. For 0%, 2%, and 5% GNP coatings, CHF of 155 W/cm², 269 W/cm², and 267 W/cm² were achieved respectively. The heat transfer coefficient for each heat flux was calculated for each surface after performing the pool boiling test and was plotted against the heat flux as shown in Fig. 62b. The maximum HTC of 1314 kW/m²-°C was obtained for 20 µm Cu-3% GNP coating, while HTC of 227 kW/m²-°C, 399 kW/m²-°C, and 431 kW/m²-°C were achieved for 20 µm Cu-0%, 2%, and 5% GNP coatings (Fig. 62b), respectively.

A reduction in the wall superheat temperatures with increased heat flux, a phenomenon termed as ‘‘Boiling Inversion” by Jaikumar and Kandlikar, was also observed for these surfaces. This shift is attributed to the surface morphology of the coatings and increased active nucleation sites culminating from tunable porosity resulting from salt

templating. However, owing to the complexity related to combined effects of wettability, active nucleation site density, number of deposited graphene layers, and changes in the morphological structure, an in-depth study is required to understand the individual effects of each parameter.

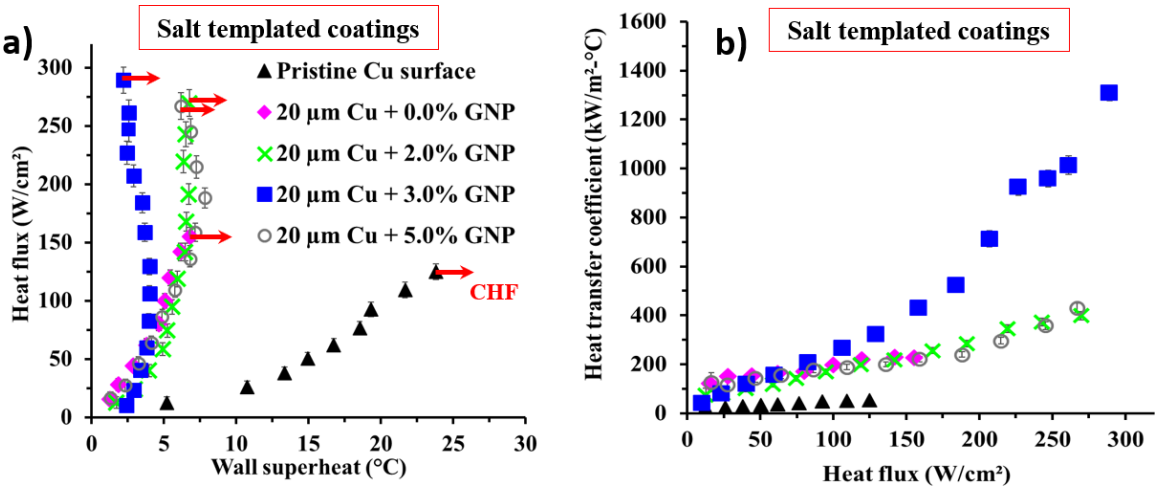

Figure 62. Comparison of effect of salt templating during sintering on pool boiling performance of 2%, 3%, and 5% GNP draped 20 µm Cu coatings showing a) Heat Flux vs wall superheat depicting pool boiling regimes, b) heat transfer coefficient vs heat flux summarizing heat transfer performance

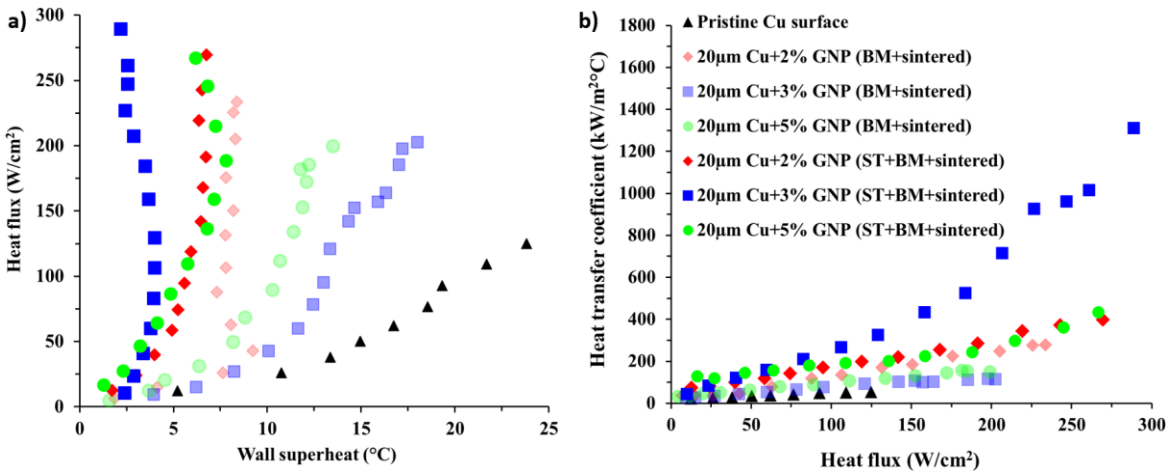

Figure 63: Comparison of pool boiling performance of the ball milled non-salt templated sintered and ball milled salt templated sintered coatings, showing the superiority of the latter coating technique

4.4.1.2.1 Enhancement mechanism for dramatic improvements in pool boiling performance for ball milled and salt templated sintered coatings:

To observe the effect of sintering via GNP-draped-copper particles and increased porosity on wicking properties of the coatings, we measured wettability and wickability of the coated surfaces using a sessile water droplet method before conducting the pool boiling experiments. After measuring the contact angles of these surfaces using a Goniometer, all the coatings were superhydrophilic (0° contact angle). Thus, the wicking rates of the coatings were used for the comparison. The salt templated 20 µm Cu-3% GNP surface yielded the highest wicking rate indicating the highest wicked volume (Fig. 64a) as compared to salt templated 20 µm Cu-2% and 5% GNP surfaces. Figure 64a compares the change in water droplet volume with respect to time for all the surfaces. Higher wickability of the coatings allows a continuous liquid supply to the nucleation cavities during boiling, thereby delaying the vapor layer formation and enhancing the critical heat flux of the coatings. Several reports [85–87] have shown that the thermal conductivity of a few layered

graphene (2-4 layers) is in the range of ~2300 W/m-K to ~3000 W/m-K (as against 3000 W/m-K to 5000 W/m-K for a single layer of graphene). And reduces to ~2000 W/m-K with increase in the number of deposited graphene layers (greater than 4 layers). Draping of GNP on individual copper particles obtained via ball milling increased the overall thermal conductivity of the coatings. And since the pool boiling performance is primarily governed by the thermal conductivity of the coating, this increment in thermal conductivity of the coatings contributed in the enhancement of the CHF.

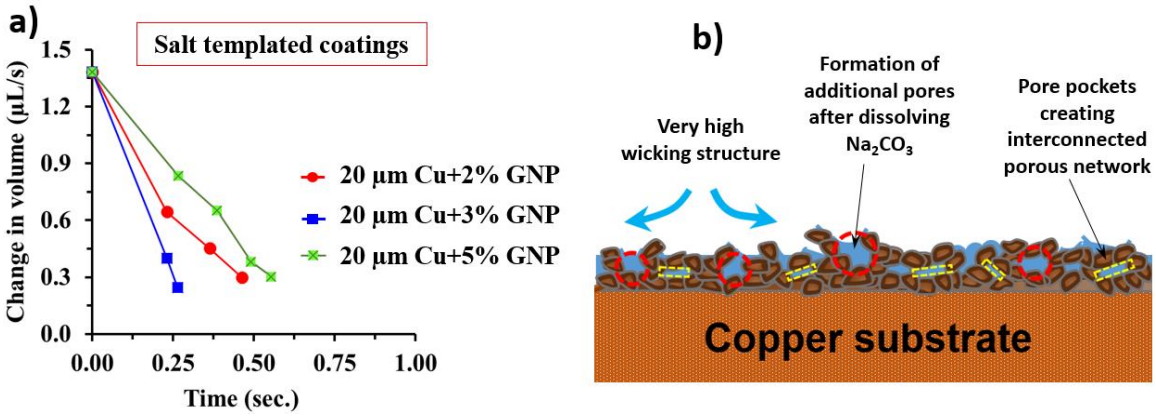

Figure 64: a) comparison of change in water droplet volumes, b) schematic indicating the factors responsible for enhancement in pool boiling performance

A detailed morphological analysis of the coatings reveals inhomogeneous and irregular porous surface morphology as a result of combined ball milling and sintering with salt templating (Fig. 61d, 61e, 61f, and Fig. 66). Ball milling induced additional rectangular pores termed as "pore pockets" as shown in Fig. 66b. Salt templating and sintering methods provided supplementary pores with a wide range of porosity ranging from ~2 µm – ~200 µm. To further understand the effect of these additional pores on nucleation activity, the application of Hsu's model [88] to the pool boiling results can support in estimating the

cavity sizes that nucleate at different wall superheat temperatures. This model can also assist in determining the cavity sizes that nucleate at the point of "Boiling Inversion" and the cavity sizes which act as liquid reservoirs. The range of active nucleation cavity sizes is determined by the following equation:

$$\left[R_{c,max}, R_{c,min}\right] = \frac{\delta_t C_2}{2C_1}\left[\frac{\Delta T_{sat}}{\Delta T_{sat}+\Delta T_{sub}}\right] \times \left[1 \pm \sqrt{\frac{1-8C_1\sigma T_{sat}(\Delta T_{sat}+\Delta T_{sub})}{\rho_v h_{fg}\delta_t(\Delta T_{sat})^2}}\right] \quad (16)$$

Where $C_1 = 1 + \cos\theta_r$ and $C_2 = \sin\theta_r$. $R_{c,max}\ and\ R_{c,min}$ are maximum and minimum radii of the nucleation cavities, θ_r is the receding contact angle, δ_t is thermal boundary layer thickness (m), ΔT_{sat} is the wall superheat temperature ($\Delta T_{sat} = T_{surface} - T_{sat}$) (K), ΔT_{sub} is the subcooled temperature (K), σ represents the surface tension of water at saturation temperature (N/m), ρ_v is the vapor density (kg/m^3), and h_{fg} represents the latent heat of vaporization (J/kg).

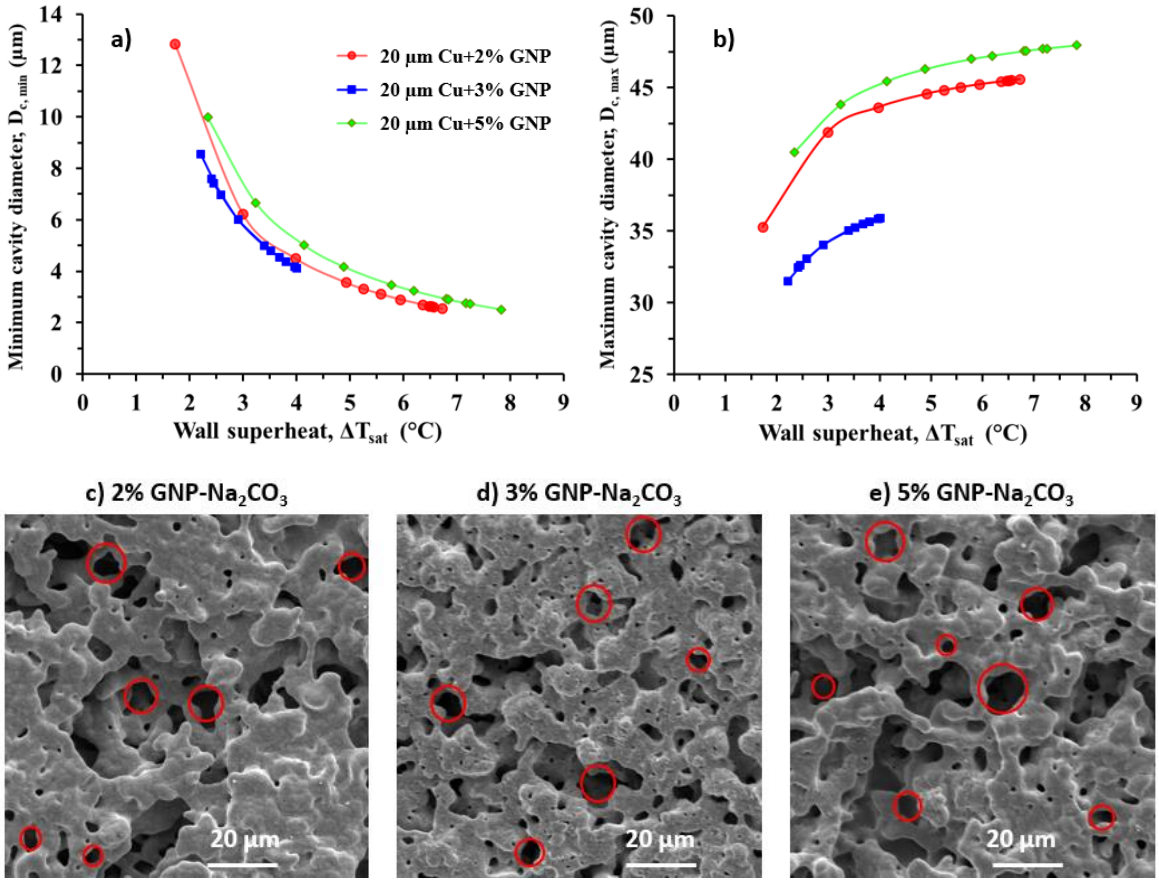

Figure 65: Range of active nucleation cavities for 2%, 3%, and 5% GNP coatings showing a) Minimum cavity diameters, b) Maximum cavity diameters as a function of wall superheat temperature using Hsu's model41, c), d), and e) SEM images at 2kX magnification confirming the availability of wide range of porous network in the estimated range of diameters

Figures 65a and 65b show the minimum and maximum diameters of the active nucleation cavities for all three coatings. The receding contact angle for each surface was measured at multiple nucleation sites using a high-speed camera, and the average value was considered while calculating the range of active nucleation cavities. The plots show the range of possible nucleation cavity diameters, 45.5 µm to 2.6 µm for 2% GNP coating, 31.5 µm to 8.5 µm for 3% GNP coating, and 47.3 µm to 3.3 µm for 5% GNP coating. These diameters are estimated using equation (16), and similar to our previous work[19], the HTC of 6000 W/m²-°C was used assuming a linear thermal boundary layer during the

calculation of boundary layer thickness for each surface. Figures 65c, 65d, and 65e, as well as Figs. 61d, 61e, 61f demonstrate the morphologies of the salt templated sintered coatings confirming the pores with a different range of cavity sizes. These cavity sizes are within the predicted nucleation range of Fig. 65a and 65b. When the pool boiling curve (see Fig.62a) begins to shift to the left, the effects arising from additional cavities is amplified. Consequently, the HTC increases significantly due to the increased contribution from the rapid nucleation activity.

From the plot shown in Fig. 65a, it is observed that as the wall superheat increases, smaller nucleation cavities activate, resulting in significant enhancement in HTC due to the amplified contribution from the rapid nucleation activity. It is proposed that the cavities outside the range of active nucleation site diameter range act as liquid reservoirs and liquid supply sites (Fig. 66 a-f). The larger pores resulted from the salt templating (Fig. 66 a-c) and micro, and nanoscale tunnels resulted from sintering (Fig. 66 d-f), thus provide a continuous liquid supply to the nucleating cavities, thereby increasing both CHF and HTC. Compared to 2% and 5% GNP surfaces (Fig. 66a, and 66c), in case of 3% GNP coating, additional liquid pathways are developed on the coating termed as “pore pockets” (length: 50–150 µm and width: 10–50 µm) (see Fig. 66b). The combination of all these factors resulted in achieving the lowest wall superheat temperature (2.2°C) and the highest CHF (289 W/cm²) for 3% GNP coating.

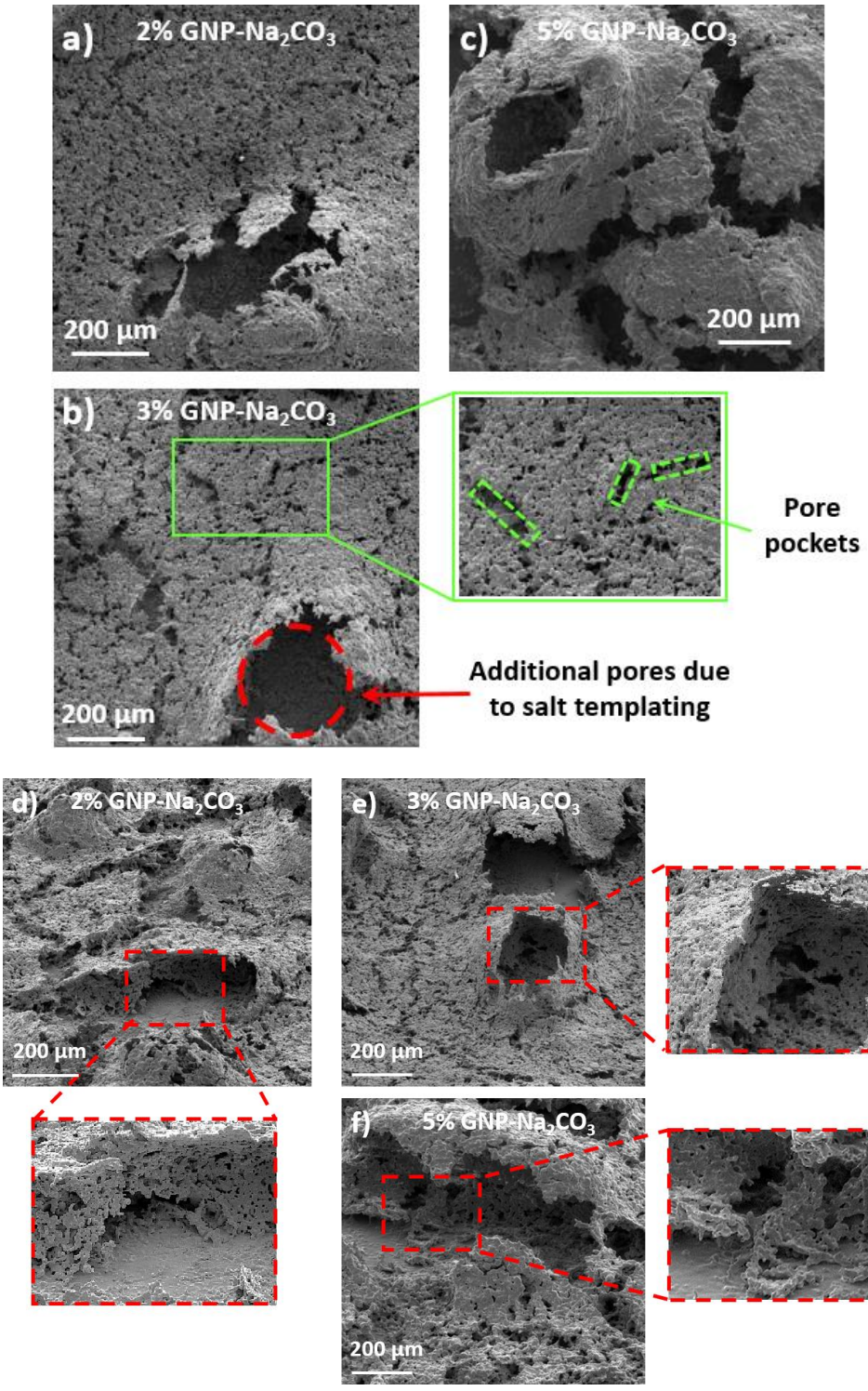

Figure 66. Scanning electron microscope images at 200X for salt templated GNP draped Cu coatings (20 µm Cu particles) a) 2% GNP, b) 3% GNP, and c) 5% GNP, Stage tilted scanning electron microscope images for salt templated GNP draped Cu coatings d) 2% GNP, e) 3% GNP, and f) 5% GNP

To further understand the effect of salt templated coatings on bubble dynamics, high-speed images for 2%, 3%, and 5% GNP salt templated coatings were obtained at a heat flux of ~10 W/cm² using a Photron Fastcam high-speed camera. As a baseline, the bubble dynamics was captured for the plain copper surface. The total time required for a single bubble to nucleate, grow, and depart was 13 ms and a bubble departure diameter of 2.1 mm was attained for a plain copper surface. Due to the presence of hierarchical porous structures on the salt-templated sintered coatings, rapid bubble growth was observed for all coatings containing GNP wt. % at varying ratios. The smallest bubble departure diameter of 0.452 mm at the shortest departure time of 2.25 ms was recorded for the 20 µm Cu-3% GNP salt templated coating. In contrast, departure diameters and time of 0.51 mm, 3 ms and 0.554 mm, 2.75 ms were observed for 20 µm Cu-2% GNP and 20 µm Cu-5% GNP salt templated coatings, respectively. Rapid bubble departures in short durations for the salt templated coatings resulted in high heat transfer performances.

This work presents a novel approach of obtaining highly surface-active composite coatings with tunable properties by combining ball milling, sintering, and salt-templating techniques. These coatings demonstrated a significant enhancement in the pool boiling heat transfer performance by yielding the highest critical heat flux (289 W/cm²) and the heat transfer coefficient (1314 kW/m²-°C), compared to similar surfaces reported in the literature. These high CHF and HTC values are desirable for effective thermal management in many applications, including electronics cooling, reboilers, and heat exchangers. Our extensive studies indicated that an alternate 15 min. ball milling and 1 hr. cooling cycles implemented during the ball milling process draped higher thermal conductivity GNP on individual copper particles (GNP ~2000-3000 W/m-K and copper ~391 W/m-K), which

ultimately enhanced wicking and thermal properties of the coatings, thereby dramatically improving the pool boiling performance. This dramatic enhancement in heat transfer performance is also attributed to the salt templating via the addition of Na_2CO_3 pellets during the sintering process and eliminating them after sintering to achieve a wide range of porous network. Wide range of available porous network and pore openings act as liquid retention reservoirs to provide a continuous liquid supply to the nucleation sites which delays the vapor blanket formation. As indicated in schematic 64b, unique properties of GNP-draped-copper particles and a subsequent formation of microporous coating with salt templating using Na_2CO_3, optimized the factors responsible for higher pool boiling performance.

4.4.1.2.2 High-speed image analysis and repetitive testing of salt templated coatings:

To understand the behavior of vapor bubbles during boiling due to implementation of salt templated sintering, high-speed images were captured for 2, 3, and 5% GNP coatings. Due to the presence of hierarchical porous structures on the salt-templated sintered coatings, rapid bubble growth was observed for all coatings. The smallest bubble departure diameter of 0.452 mm at the shortest departure time of 2.25 ms was recorded for the 20 μm Cu-3% GNP ball milled and salt templated sintered coating. While departure diameters and time of 0.51 mm, 3 ms and 0.554 mm, 2.75 ms were observed for 2% GNP 5% GNP coatings, respectively. Rapid bubble departures in short durations for the salt templated coatings resulted in very high heat transfer performances. Total 3 repetitive pool boiling tests were performed on the best performing 20 μm Cu-3% GNP salt templated coating. A small deterioration in the pool boiling performance was observed at the end of the third repetitive pool boiling test, yielding the CHF of 279 W/cm² at a wall superheat of

4.9°C. This can be minimized by stopping the pool boiling test before the surface hits the CHF.

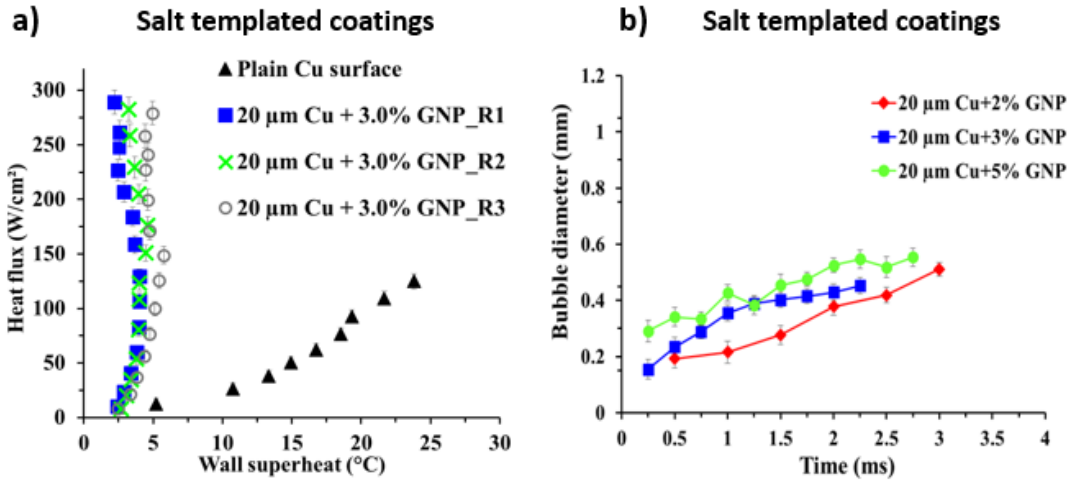

Figure 67: a) Pool boiling curve showing repetitive testing of 20 µm Cu-3% GNP BM + salt templated + sintered coating, b) Plot showing the progression of vapor bubble diameter with respect to time for salt templated sintered coatings

4.5 Comparison Study of Best Performing GNP-based Coatings:

To compare the electrodeposition and sintering effects on overall morphological and structural properties of the developed coatings, the best performing (overall pool boiling performance) surfaces from electrodeposition and sintering methods were considered. These surfaces under consideration for comparison were – 2% GNP electrodeposited coating, 20 µm Cu-2% GNP BM + sintered coating, and 20 µm Cu-3% GNP BM + salt templated + sintered coating. ImageJ analysis was performed on the SEM images (Figure 68 a-c) to quantify the number of pores and their surface area. Initially, the images were converted in black and white to understand the difference in the porous and non-porous areas. The analysis was then performed via analyzing the porous area and

obtaining a pore size vs pore volume distribution. The correlation between their equivalent projected circle (EQPC) diameters of pores with number of pores as shown in Fig. 68d. EQPC is a widely used method to estimate the projected area of the particles of arbitrary shapes, in this work, it was also used to assess the pore diameter [89,90]. The plot on Fig. 68d corresponds to the ImageJ analysis of the SEM images on Figs. 68 a-c. Ball milled + salt templated sintered coating comprising of 20 µm diameter copper particles with 3 wt. % GNP yielded a maximum number of pores for almost all EQPC diameters ranging from 5-16 µm. Additional SEM images revealed larger pores (> 50 µm) were also observed for salt patterned sintered coatings. This was one of the main factors responsible for achieving the highest pool boiling performance for graphene-based coatings on plain copper surfaces. Highly microporous structure with the presence of larger pores (> 50 µm) act as liquid retention sites and delay horizontal coalescence of vapor bubbles. As mentioned in the previous part of the results, all GNP-based coatings, irrespective of their deposition technique, exhibited superhydrophilicity.

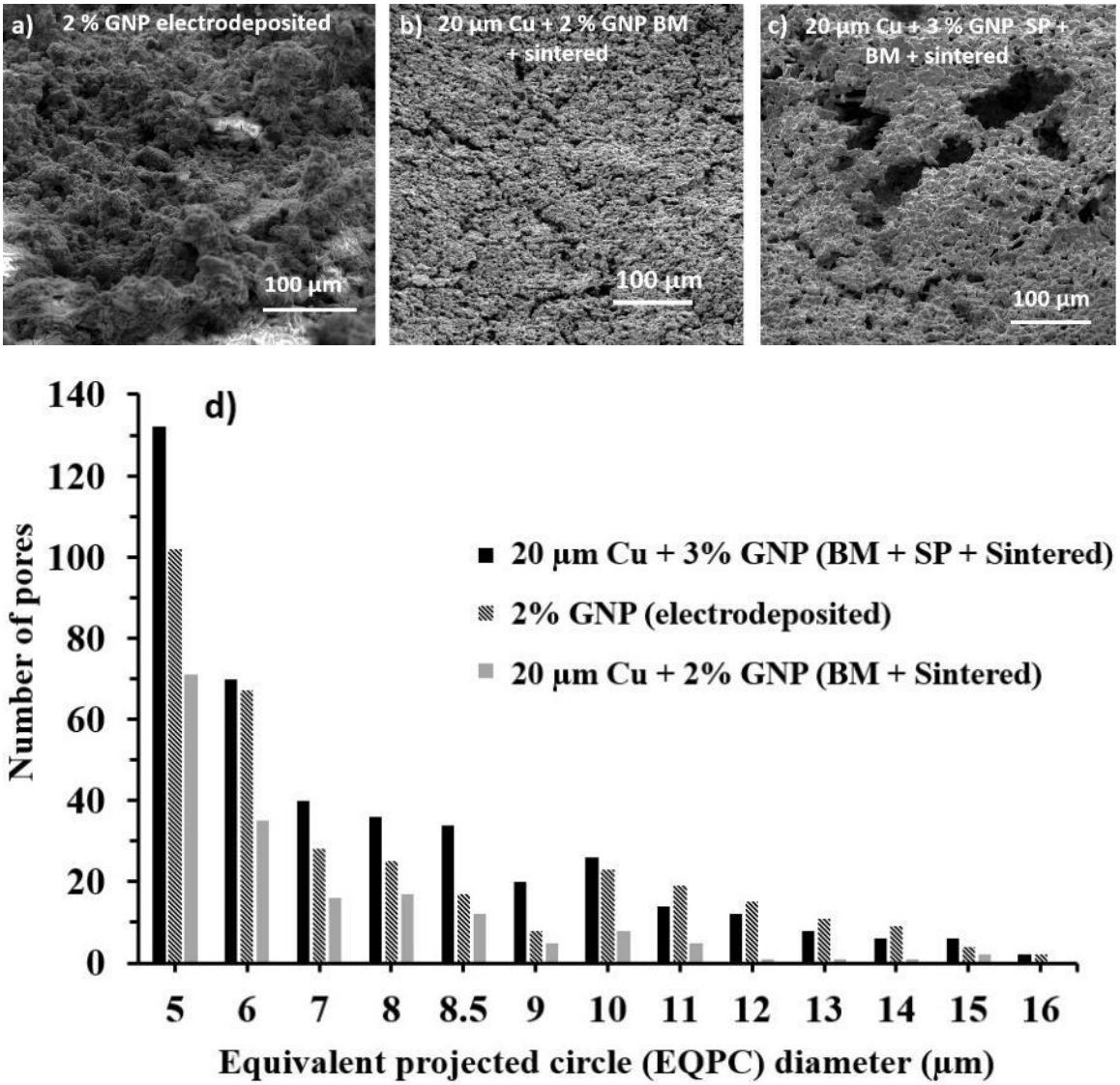

Figure 68: 55° stage tilted scanning electron microscope images for a) 2% GNP electrodeposited surface, b) 20 µm Cu-2% GNP ball milled + sintered surface, and c) 20 µm Cu-3% GNP ball milled + salt templated sintered surface, d) Plot showing the number of pores vs equivalent projected circle (EQPC) diameter of pores for different functional surfaces

Figure 69a and 69b compares the pool boiling and heat transfer coefficient performance of the three coatings that are compared. High CHF and HTC values obtained for the coatings can be correlated to their unique surface morphologies. The higher CHF of 286 W/cm² obtained for electrodeposited coatings is due to the presence of the tall ridge-like structures, as observed in Fig 68a. The void spaces between the taller structures supply a liquid reservoir that induces microlayer evaporation. The microlayer enhances the nucleation on the surface and subsequently increases the heat flux dissipation. Additionally, these types of structures create roughness by increasing wickability at the sub-micron scale. However, when compared to ball milled surfaces, the HTC obtained for electrodeposited surfaces were observed to be lower at ~200 kW/m^2-°C (Fig. 69b). The CHF obtained for ball milled and the sintered coating was found to be 239 W/cm² which is comparatively lower than CHF obtained for electrodeposited coatings. This is ascribed to the flatness of the copper particles induced by their collisions with balls and the subsequent spreading or draping of GNP on the copper surfaces that occurs during the ball milling and seen in Fig. 68b. This flatter surface lacked optimum roughness to induce microlayer evaporation to enhance heat dissipation through bubble nucleation. However, a higher HTC was obtained for this coating as compared to electrodeposited coatings. An extensive electron microscopy investigation indicated the presence of open and closed pores on these coatings (Fig. 69e). Electrodeposited coatings possessed open pores as shown schematically in Fig. 69d that yielded a pathway for bubble departure to improve the critical heat flux.

The reduced heat dissipation or lower CHF obtained with a sintered coating comprising of ball milled particles was overcome by implementing a salt templating step

that formed an interconnected porous network and provided larger liquid retention sites for enabling microlayer evaporation. These larger pores also delayed horizontal bubble coalescence, effectively cooling the boiling surface and providing with the highest heat transfer coefficient of 1314 kW/m²-°C achieved till date for porous coatings on plain copper surfaces. Such large pores also provide secondary boiling effects, which is also established in the literature [91]. In terms of pore characteristics discussed earlier, the pores resulting from ball milled particles and, more so, salt patterning demonstrated closed pore morphology schematically illustrated in Fig. 69e and 69f. These closed pores introduced a large thermal gradient during boiling, which primarily reduced the wall superheat temperature, thereby increasing the HTC. These pore characteristics influence the wall superheat and were responsible for an increasing trend in the heat transfer coefficient observed in Fig 69b.

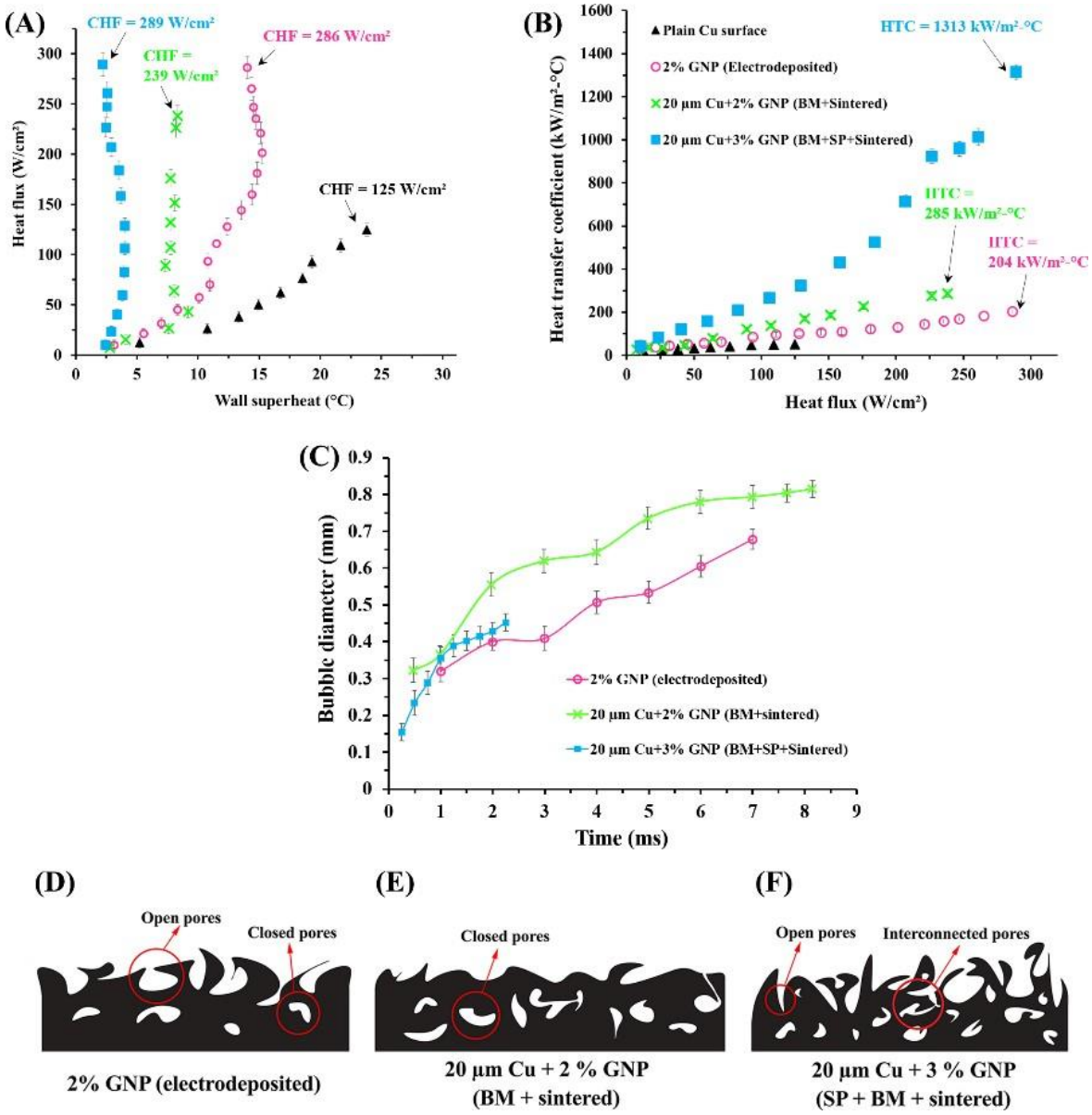

Figure 69: Schematic representing the types of pores formed for a) comparison of CHF and HTC values of different functional surfaces with the plain copper surface b) 2% GNP electrodeposited surface, c) 20 µm Cu-2% GNP ball milled + sintered surface, and d) 20 µm Cu-3% GNP ball milled + salt templated sintered surface

In addition to bubble departure diameter and time (Fig. 69c), bubble release frequency is also one of the important parameters that dictates the overall pool boiling performance. One of the most comprehensive correlation between bubble release

frequency and vapor bubble departure diameter is provided by Malenkov [92]. Based on this, a bubble release frequency was estimated for all the three coatings used in this study with the following equation:

$$\boldsymbol{f D_d = \frac{V_d}{\pi * \left(1 - \frac{1}{1 + V_d * \rho_v * h_{fg}/q}\right)}} \qquad (17)$$

where, f is the bubble release frequency (numbers/second), D_d is the vapor bubble departure diameter (m), ρ_l and ρ_v are densities of liquid and vapor (kg/m^3), g is the acceleration due to gravity (m/s^2), σ is the surface tension of the liquid at saturation conditions (N/m), h_{fg} is the latent heat of vaporization (J/kg), q is the corresponding heat flux (W/m^2), and V_d represents the velocity of the departing bubble (m/s). Here, V_d is given by Equation 2 [93].

$$\boldsymbol{V_d = \sqrt{\frac{D_d * g * (\rho_l - \rho_v)}{2 * (\rho_l + \rho_v)} + \frac{2 * \sigma}{D_d * (\rho_l + \rho_v)}}} \qquad (18)$$

During boiling, a new bubble can grow only when the pressure at the nucleation cavity becomes equal to the total pressure at the heated surface. With the increase in heat flux, bubble release frequency from nucleation sites increases, and bubbles merge in the vertical direction forming vapor columns [93]. A smaller bubble diameter and departure time and a higher bubble release frequency thus provide a rapid heat transfer allowing the greater reduction in wall superheat temperature. Based on the measured vapor bubble departure diameters for each of the coating, bubble release frequency was calculated. And a maximum f of ~450 (~250 and ~210 for 2% GNP electrodeposited surface and 20 µm Cu-2% GNP ball milled + sintered surface, respectively) was obtained for 20 µm Cu-3% GNP ball milled + salt templated sintered surface. This value depicts an extremely large

number of vapor bubble release from the heated surface and thus contributed to achieving the highest HTC for the salt pattered surface. At higher heat fluxes, activation of additional nucleation sites contributed to obtaining higher heat transfer coefficients for sintered and salt templated sintered coatings.

Chapter 5

5. Summary and major Accomplishments

5.1 Major accomplishments:

Efficient thermal management of microelectronic components, integrated circuit chips, and high-power electronic devices has transpired into one of the most critical factors over the recent years due to increment in the number of smaller transistor devices and compact electronic package systems. Data centers have become an indistinguishable part of numerous industries, and currently implemented single-phase cooling techniques in data centers consume ~40% of the total power consumption. In this era of electric vehicles (EV) technology, efficient heat removal from lithium-ion battery packs via two-phase cooling is also observed as the potential application to prevent overheating and thermal runaway of automobile vehicles. Large power consumption and inefficient cooling with the existing single-phase cooling techniques are the primary purposes of research in the field of two-phase cooling. Pool boiling heat transfer is a type of two-phase cooling which is frequently restricted by lower heat dissipation due to excessive vapor generation and early coalescence. Thus, the specific purpose of this research work was to enhance this pool boiling performance to higher values using various coating techniques. Higher values of heat fluxes and heat transfer coefficient ensure safe operational ranges with an increased safety and lower power consumption while maintaining the surface temperatures within limits.

The major contributions from this work are summarized below:

1) To make usage of properties of both copper and GNP, composite coatings were developed. The role of graphene nanoplatelets in coatings was to alter the wettability and to improve thermal conductivity of the coatings while the role of copper was to control and influence the morphological structure at microscale.
2) The use of graphene nanoplatelets (GNP) for pool boiling heat transfer enhancement was explored owing to higher thermal properties, surface area, and wettability of GNP. Graphene nanoplatelets/copper-based (GNP/Cu) composite coatings were developed using two-step electrodeposition technique by varying GNP concentration. And 2% GNP/Cu coating rendered the critical heat flux (CHF) of 286 W/cm² and a heat transfer coefficient (HTC) of 204 kW/m²-°C. This performance was ~130% higher in CHF and ~290% higher in HTC with respect to a plain copper surface.
3) Formation of unique tall microporous structures developed unique morphological microstructures, which increased microlayer evaporation. While deposition of highly thermally conductive and highly wettable GNP (~3000 W/m-K) drastically increased wicking rates and in-plane thermal conductivity of the coatings that delayed vapor blanket formation. A combination of these two enhancement mechanisms was responsible for dramatic improvements.
4) Repetitive testing was performed on 2% GNP/Cu coating, which indicated the improvements in heat transfer coefficient (300 kW/m²-°C after the third repetitive test) as compared to the initial HTC of 204 kW/m²-°C with a slight reduction in CHF (262 W/cm² vs. 286 W/cm² after the third repetitive test). Raman spectroscopy analysis revealed the formation of reduced-GNP (r-GNP)/Cu coating with repetitive boiling. r-GNP is the reduced form of GNP, which forms by the elimination of hydroxyl and

carboxyl groups from carbon chains of GNP. This also dramatically changed wettability, forming superhydrophobic coatings, which promoted early nucleation and yielded higher HTC.

5) The theoretical model indicated that in addition to roughness induced enhancement, an additional mechanism was responsible for the increment in HTC. Higher thermal conductivity of r-GNP also assisted in reducing local hot spot generation on the boiling surface and increased efficient heat removal with lower wall superheat (i.e., higher HTC). This study indicates that GNP/Cu composite coatings have a substantial potential to provide sustainable and durable coatings for boiling related applications.
6) To further enhance the cohesive and adhesive bond strength of the electrodeposited coatings, a novel multi-step electrodeposition technique was developed and was tested on copper-based coatings. Particularly, three-step and seven-step electrodeposited coatings were developed with copper deposition. Owing to the initial low current and high time step, an initial base layer was deposited, which increased adhesion with the substrate. Subsequent deposition and bond strengthening steps provided additional bolstering, increasing adhesive and cohesive bond strength of the coatings which was tested using repetitive pool boiling studies.
7) Multi-step electrodeposition technique also enhanced the surface properties of the coatings, including porosity, wickability, and wettability. And ultimately resulted in the highest CHF and HTC for the copper coatings. Compared to the existing two-step electrodeposition with copper coatings in literature, the novel seven-step electrodeposition technique increased the CHF by 41% and HTC by 52%. Compared

to a plain copper surface, this enhancement in CHF and HTC was 72% and 93%, respectively.

8) The sintering technique is widely implemented in various industries to develop coatings and materials from metal powders. For pool boiling applications, to enhance the performance, graphene nanoplatelets-copper (GNP-Cu) composite coatings were developed, but due to the lack of uniform spreading of GNP throughout the coating, a drastic improvement was not observed. To overcome this, a novel technique was developed through which initially a ball milling of GNP and copper particles was conducted to drape GNP around individual copper particles. The ball milling process also developed a homogeneous powdered mixture of GNP and copper particles and along with the reduction in particle size, altered the surface features. This ball milled powder was then sintered using a screen-printing technique. As a result, among various copper particle sizes and GNP concentrations, 20 μm Cu-2% GNP coating yielded a higher pool boiling performance with a CHF of 239 W/cm² (~91% higher than a plain copper surface) and the HTC of 285 kW/m²-°C (~438% higher than a plain copper surface).
9) Theoretical analysis suggested that apart from higher wicking rates of coatings, an additional enhancement factor was responsible for the enhancement. This excessive enhancement was attributed to the combination of formation of rectangular pore pockets formed on the coatings, additional thermal conductivity due to draping of GNP around individual copper particles, and uniform spreading of GNP over the coating.
10) To obtain a better control on the porosity and wicking properties of the sintered coatings, a distinctive technique of salt templated sintering was developed in the final

part. Sintered coatings obtained by the combination of ball milling and salt templated sintering method formed a large spectrum of pore diameters ranging from a few microns to a few hundred microns. Amongst various GNP concentrations and copper particle sizes, the 20 μm Cu-3% GNP coating yielded the highest CHF, and HTC reported in the pool boiling studies involving graphene and porous coatings on a plain copper surface, with a CHF of 289 W/cm² at a wall superheat of just 2.2 °C (HTC of 1,314 kW/m²-°C). Compared to available enhancements on plain boiling surfaces, CHF obtained using these coatings was ~13% higher, while HTC showed ~1500% of massive improvement.

11) This dramatic enhancement was due to a combination of various factors that are listed as follow: i) uniform spreading of GNP over the entire coating due to ball milling of GNP and copper particles that also led to a drastic increment in thermal conductivity of sintered coatings due to draping of copper particles with higher in-plane thermal conductivity of GNP (~3000 W/m-K). This reduced local variations in surface temperatures and hot spots, allowing very efficient heat dissipation – highest HTC (1314 kW/m²-°C). ii) Altered nano and microstructures of the ball milled GNP-draped-Cu particles – increased surface area to volume ratio, modified and generated unique morphological structures, iii) Increased wicking properties of the sintered coatings due to uniform spreading of highly wettable GNP and sintered deposition with porous copper. iv) Formation of larger pores (> 50 μm) due to implementation of salt templated sintering that acted as liquid retention sites. And provided a continuous liquid supply to nucleation sites, acted as spacers between nucleation sites, and delayed horizontal vapor bubble coalescence, thus achieving the highest CHF (289 W/cm²), v) Formation

of closed pores, tunnel structures, nano and micro-sized pores assisting in enhancing the overall boiling performance via thermal gradient formation, and effective vapor-liquid supply pathways, vi) Smaller vapor bubbles formation with higher bubble frequency – overall improvement in bubble dynamics assisting in increasing the performance.

12) Additional theoretical modeling for salt templated sintered coatings was performed, indicating the range of active nucleation cavities sizes (~8 µm to 32 µm) during boiling and their corresponding activation temperature ranges. This analysis confirmed that additional pores acted as liquid retention sites and contributed to improving the CHF and HTC.
13) The findings from this work were published in 5 journal articles, 4 international conference proceedings papers, and 4 international conference presentations.

5.2 Future work and recommendations:

In this work, novel techniques and processes were developed to test their efficacy for pool boiling heat transfer performance. The effect of porosity on alteration of wetting and wicking properties of the coatings as well as vapor bubble behavior led to increased microlayer evaporation, bubble generation, and departure rates, thus enhancing the CHF and HTC during boiling. Some of the relevant and beneficial suggestions for future work are discussed below:

- Selective deposition of the coatings developed in this work on different microchannel geometries will provide a combined intensified effect of porosity, alteration of bubble dynamics and surface area enhancement. This effect is expected to further delay the vapor layer formation on the boiling surfaces and obtain tremendous improvements in both CHF and HTC.
- Testing of graphene nanoplatelets (GNP)-based microporous surfaces developed in this work with dielectric fluids can provide better insight on their usage in electronics cooling applications. Overall pool boiling performance with these surfaces is expected to be better than plain copper surfaces due to deposition with highly thermally conductive GNP-copper composites and the development of smaller pores to assist increased boiling.
- Metal powders manufactured in this work via ball milling process possess higher thermal and mechanical properties. Using these metal powders, compact graphene nanoplatelets-reinforced-copper metal blocks can be manufactured using different high-pressure and high-vacuum press techniques followed by their subsequent sintering to tune the porosity as per the target application requirement. These highly thermally conductive surfaces can be directly used in boiling applications instead of coatings. A similar approach can be used to create graphene nanoplatelets-reinforced-aluminum structures since aluminum is widely used in automotive car radiators and cooling applications. A parametric study can be developed to create an optimum thickness that will provide higher thermal and mechanical properties than the base metal.

- In this work, multi-step electrodeposition (3-step and 7-step) study for further improvement in bond strength and durability of the coated surfaces is conducted on copper coatings. Implementation of using carbon nanomaterials such as graphene (G), graphene oxide (GO), graphene nanoplatelets (GNP), reduced-GO (r-GO), and r-GNP along with copper for 3-step and 7-step electrodeposition techniques will further bolster the coatings and enhance the durability and sustainability of the coatings.

Chapter 6

6. References

[1] Kandlikar, S. G., 1999, *Handbook of Phase Change: Boiling and Condensation*, CRC Press.

[2] Kandlikar, S. G., Shoji, M., and Dhir, V. K., eds., 2019, *Handbook of Phase Change: Boiling and Condensation: Boiling and Condensation*, Routledge, Boca Raton.

[3] Hsu, Y. Y., 1962, "On the Size Range of Active Nucleation Cavities on a Heating Surface," J. Heat Transf., **84**(3), pp. 207–213.

[4] Kandlikar, S. G., and Spiesman, P. H., 1998, *Effect of Surface Finish on Flow Boiling Heat Transfer, American Society of Mechanical Engineers, Heat Transfer Division (Publication*.

[5] Honda, H., and Wei, J. J., 2004, "Enhanced Boiling Heat Transfer from Electronic Components by Use of Surface Microstructures," Exp. Therm. Fluid Sci., **28**(2–3), pp. 159–169.

[6] "Wolverine Tube INC., 2006, Boiling heat transfer on external surfaces, engineering data book

[7] Barker, D., and Walsh, F. C., 1991, "Applications of Faraday's Laws of Electrolysis in Metal Finishing," Trans. IMF, **69**(4), pp. 158–162.

[8] Jang, M., 2016, "The Potential Power of Graphene," **3**(4), p. 12.

[9] 2011, "The Sp2 Nanocarbons: Prototypes for Nanoscience and Nanotechnology," *Raman Spectroscopy in Graphene Related Systems*, Wiley-VCH Verlag GmbH & Co. KGaA, Weinheim, Germany, pp. 1–15.

[10] Bergles, A. E., and Chyu, M. C., 1982, "Characteristics of Nucleate Pool Boiling from Porous Metallic Coatings," J. Heat Transf., **104**(2), pp. 279–285.

[11] Wojcik, T. M., 2009, "Experimental Investigations of Boiling Heat Transfer Hysteresis on Sintered, Metal ? Fibrous, Porous Structures," Exp. Therm. Fluid Sci., **33**(3), pp. 397–404.

[12] Sadaghiani, A. K., Motezakker, A. R., Kasap, S., Kaya, I. I., and Koşar, A., 2018, "Foamlike 3D Graphene Coatings for Cooling Systems Involving Phase Change," ACS Omega, **3**(3), pp. 2804–2811.

[13] WEBB, R. L., 1983, "Nucleate Boiling on Porous Coated Surfaces," Heat Transf. Eng., **4**(3–4), pp. 71–82.

[14] Mori, S., and Okuyama, K., 2009, "Enhancement of the Critical Heat Flux in Saturated Pool Boiling Using Honeycomb Porous Media," Int. J. Multiph. Flow, **35**(10), pp. 946–951.

[15] Jun, S., Kim, J., Son, D., Kim, H. Y., and You, S. M., 2016, "Enhancement of Pool Boiling Heat Transfer in Water Using Sintered Copper Microporous Coatings," Nucl. Eng. Technol., **48**(4), pp. 932–940.

[16] Li, Q., Wang, W., Oshman, C., Latour, B., Li, C., Bright, V. M., Lee, Y.-C., and Yang, R., 2011, "Enhanced Pool Boiling Performance on Micro-, Nano-, and Hybrid-Structured Surfaces," *Volume 10: Heat and Mass Transport Processes, Parts A and B*, ASME, Denver, Colorado, USA, pp. 633–640.

[17] Liter, S. G., and Kaviany, M., 2001, "Pool-Boiling CHF Enhancement by Modulated Porous-Layer Coating: Theory and Experiment," Int. J. Heat Mass Transf., **44**(22), pp. 4287–4311.

[18] Kandlikar, S. G., 2001, "A Theoretical Model to Predict Pool Boiling CHF Incorporating Effects of Contact Angle and Orientation," J. Heat Transf., **123**(6), p. 1071.

[19] Chu, K.-H., Soo Joung, Y., Enright, R., Buie, C. R., and Wang, E. N., 2013, "Hierarchically Structured Surfaces for Boiling Critical Heat Flux Enhancement," Appl. Phys. Lett., **102**(15), p. 151602.

[20] Yao, Z., Lu, Y.-W., and Kandlikar, S. G., 2011, "Effects of Nanowire Height on Pool Boiling Performance of Water on Silicon Chips," Int. J. Therm. Sci., **50**(11), pp. 2084–2090.

[21] Rahman, M. M., Ölçeroğlu, E., and McCarthy, M., 2014, "Role of Wickability on the Critical Heat Flux of Structured Superhydrophilic Surfaces," Langmuir, **30**(37), pp. 11225–11234.

[22] Park, S. D., Won Lee, S., Kang, S., Bang, I. C., Kim, J. H., Shin, H. S., Lee, D. W., and Won Lee, D., 2010, "Effects of Nanofluids Containing Graphene/Graphene-Oxide Nanosheets on Critical Heat Flux," Appl. Phys. Lett., **97**(2), p. 023103.

[23] Sarafraz, M. M., and Hormozi, F., 2016, "Experimental Investigation on the Pool Boiling Heat Transfer to Aqueous Multi-Walled Carbon Nanotube Nanofluids on the Micro-Finned Surfaces," Int. J. Therm. Sci., **100**, pp. 255–266.

[24] Azizi, M., Hosseini, M., Zafarnak, S., Shanbedi, M., and Amiri, A., 2013, "Experimental Analysis of Thermal Performance in a Two-Phase Closed Thermosiphon Using Graphene/Water Nanofluid," Ind. Eng. Chem. Res., **52**(29), pp. 10015–10021.

[25] Kim, J. M., Kim, T., Kim, J., Kim, M. H., and Ahn, H. S., 2014, "Effect of a Graphene Oxide Coating Layer on Critical Heat Flux Enhancement under Pool Boiling," Int. J. Heat Mass Transf., **77**, pp. 919–927.

[26] Ahn, H. S., Kim, J. M., Kaviany, M., and Kim, M. H., 2014, "Pool Boiling Experiments in Reduced Graphene Oxide Colloids. Part I – Boiling Characteristics," Int. J. Heat Mass Transf., **74**, pp. 501–512.

[27] Ahn, H. S., Kim, J. M., Kaviany, M., and Kim, M. H., 2014, "Pool Boiling Experiments in Reduced Graphene Oxide Colloids Part II – Behavior after the CHF, and Boiling Hysteresis," Int. J. Heat Mass Transf., **78**, pp. 224–231.

[28] Ujereh, S., Fisher, T., and Mudawar, I., 2007, "Effects of Carbon Nanotube Arrays on Nucleate Pool Boiling," Int. J. Heat Mass Transf., **50**(19–20), pp. 4023–4038.

[29] Ahn, H. S., Sinha, N., Zhang, M., Banerjee, D., Fang, S., and Baughman, R. H., 2006, "Pool Boiling Experiments on Multiwalled Carbon Nanotube (MWCNT) Forests," J. Heat Transf., **128**(12), p. 1335.

[30] Seo, G. H., Hwang, H., Yoon, J., Yeo, T., Son, H. H., Jeong, U., Jeun, G., Choi, W., and Kim, S. J., 2015, "Enhanced Critical Heat Flux with Single-Walled Carbon Nanotubes Bonded on Metal Surfaces," Exp. Therm. Fluid Sci., **60**, pp. 138–147.

[31] Zheng, X., and Park, C. W., 2015, "Experimental Study of the Sintered Multi-Walled Carbon Nanotube/Copper Microstructures for Boiling Heat Transfer," Appl. Therm. Eng., **86**, pp. 14–26.

[32] Lee, S., Seo, G. H., Lee, S., Jeong, U., Lee, S. J., Kim, S. J., and Choi, W., 2016, "Layer-by-Layer Carbon Nanotube Coatings for Enhanced Pool Boiling Heat Transfer on Metal Surfaces," Carbon, **107**, pp. 607–618.

[33] Dharmendra, M., Suresh, S., Sujith Kumar, C. S., and Yang, Q., 2016, "Pool Boiling Heat Transfer Enhancement Using Vertically Aligned Carbon Nanotube Coatings on a Copper Substrate," Appl. Therm. Eng., **99**, pp. 61–71.

[34] Protich, Z., Santhanam, K. S. V., Jaikumar, A., Kandlikar, S. G., and Wong, P., 2016, "Electrochemical Deposition of Copper in Graphene Quantum Dot Bath: Pool Boiling Enhancement," J. Electrochem. Soc., **163**(6), pp. E166–E172.

[35] Jin, L. W., Leong, K. C., and Pranoto, I., 2011, "Saturated Pool Boiling Heat Transfer from Highly Conductive Graphite Foams," Appl. Therm. Eng., **31**(14–15), pp. 2685–2693.

[36] An, S., Kim, D.-Y., Lee, J.-G., Jo, H. S., Kim, M., Al-Deyab, S. S., Choi, J., and Yoon, S. S., 2016, "Supersonically Sprayed Reduced Graphene Oxide Film to Enhance Critical Heat Flux in Pool Boiling," Int. J. Heat Mass Transf., **98**, pp. 124–130.

[37] Seo, H., Chu, J. H., Kwon, S.-Y., and Bang, I. C., 2015, "Pool Boiling CHF of Reduced Graphene Oxide, Graphene, and SiC-Coated Surfaces under Highly Wettable FC-72," Int. J. Heat Mass Transf., **82**, pp. 490–502.

[38] Udaya Kumar, G., Soni, K., Suresh, S., Ghosh, K., Thansekhar, M. R., and Dinesh Babu, P., 2018, "Modified Surfaces Using Seamless Graphene/Carbon Nanotubes Based Nanostructures for Enhancing Pool Boiling Heat Transfer," Exp. Therm. Fluid Sci., **96**, pp. 493–506.

[39] Jaikumar, A., Gupta, A., Kandlikar, S. G., Yang, C.-Y., and Su, C.-Y., 2017, "Scale Effects of Graphene and Graphene Oxide Coatings on Pool Boiling Enhancement Mechanisms," Int. J. Heat Mass Transf., **109**, pp. 357–366.

[40] Jaikumar, A., and Kandlikar, S. G., 2015, "Enhanced Pool Boiling Heat Transfer Mechanisms for Selectively Sintered Open Microchannels," Int. J. Heat Mass Transf., **88**, pp. 652–661.

[41] Patil, C. M., and Kandlikar, S. G., 2014, "Pool Boiling Enhancement through Microporous Coatings Selectively Electrodeposited on Fin Tops of Open Microchannels," Int. J. Heat Mass Transf., **79**, pp. 816–828.

[42] Graf, D., Molitor, F., Ensslin, K., Stampfer, C., Jungen, A., Hierold, C., and Wirtz, L., 2007, "Spatially Resolved Raman Spectroscopy of Single- and Few-Layer Graphene," Nano Lett., **7**(2), pp. 238–242.

[43] Ferrari, A. C., Meyer, J. C., Scardaci, V., Casiraghi, C., Lazzeri, M., Mauri, F., Piscanec, S., Jiang, D., Novoselov, K. S., Roth, S., and Geim, A. K., 2006, "Raman Spectrum of Graphene and Graphene Layers," Phys. Rev. Lett., **97**(18).

[44] Yu, A., Ramesh, P., Itkis, M. E., Bekyarova, E., and Haddon, R. C., 2007, "Graphite Nanoplatelet−Epoxy Composite Thermal Interface Materials," J. Phys. Chem. C, **111**(21), pp. 7565–7569.

[45] Ferreira, H., Poma, G., Acosta, D. R., Barzola-Quiquia, J., Quintana, M., Barreto, L., and Champi, A., 2018, "Laser Power Influence on Raman Spectra of Multilayer Graphene, Multilayer Graphene Oxide and Reduced Multilayer Graphene Oxide," J. Phys. Conf. Ser., **1143**, p. 012020.

[46] Welty, J. R., 2008, *Fundamentals of Momentum, Heat, and Mass Transfer*, Wiley, Chichester;Hoboken, N.J;

[47] Kandlikar, S. G., 2013, "Controlling Bubble Motion over Heated Surface through Evaporation Momentum Force to Enhance Pool Boiling Heat Transfer," Appl. Phys. Lett., **102**(5), p. 051611.

[48] Jaikumar, A., and Kandlikar, S. G., 2017, "Pool Boiling Inversion through Bubble Induced Macroconvection," Appl. Phys. Lett., **110**(9), p. 094107.

[49] Kruse, C., Tsubaki, A., Zuhlke, C., Anderson, T., Alexander, D., Gogos, G., and Ndao, S., 2016, "Secondary Pool Boiling Effects," Appl. Phys. Lett., **108**(5), p. 051602.

[50] Simon, N. J., Drexler, E. S., and Reed, R. P., 1992, *Properties of Copper and Copper Alloys at Cryogenic Temperatures*, error: 177, National Institute of Standards and Technology, Gaithersburg, MD.

[51] Jaikumar, A., Rishi, A., Gupta, A., and Kandlikar, S. G., 2017, "Microscale Morphology Effects of Copper–Graphene Oxide Coatings on Pool Boiling Characteristics," J. Heat Transf., **139**(11), p. 111509.

[52] Ma, J., Meng, Q., Dai, J., and Saber, N., 2015, "Fabrication, Structure, and Properties of Graphene Platelets," Nanotub. Nanosheets Funct. Appl. Boron Nitride Nanomater., p. 173.

[53] Renteria, J., Nika, D., and Balandin, A., 2014, "Graphene Thermal Properties: Applications in Thermal Management and Energy Storage," Appl. Sci., **4**(4), pp. 525–547.

[54] Zou, A., Singh, D. P., and Maroo, S. C., 2016, "Early Evaporation of Microlayer for Boiling Heat Transfer Enhancement," Langmuir, **32**(42), pp. 10808–10814.

[55] McHale, J. P., and Garimella, S. V., 2010, "Bubble Nucleation Characteristics in Pool Boiling of a Wetting Liquid on Smooth and Rough Surfaces," Int. J. Multiph. Flow, **36**(4), pp. 249–260.

[56] Xu, Z. G., and Zhao, C. Y., 2016, “Enhanced Boiling Heat Transfer by Gradient Porous Metals in Saturated Pure Water and Surfactant Solutions,” Appl. Therm. Eng., **100**, pp. 68–77.

[57] Ahn, H. S., Kim, J. M., Kaviany, M., and Kim, M. H., 2014, “Pool Boiling Experiments in Reduced Graphene Oxide Colloids. Part I–Boiling Characteristics,” Int. J. Heat Mass Transf., **74**, pp. 501–512.

[58] Mori, S., and Okuyama, K., 2009, “Enhancement of the Critical Heat Flux in Saturated Pool Boiling Using Honeycomb Porous Media,” Int. J. Multiph. Flow, **35**(10), pp. 946–951.

[59] Raj, R., Maroo, S. C., and Wang, E. N., 2013, “Wettability of Graphene,” Nano Lett., **13**(4), pp. 1509–1515.

[60] Rishi, A. M., Gupta, A., and Kandlikar, S. G., 2018, “Improving Aging Performance of Electrodeposited Copper Coatings during Pool Boiling,” Appl. Therm. Eng., **140**, pp. 406–414.

[61] Rishi, A. M., Kandlikar, S. G., and Gupta, A., 2019, “Repetitive Pool Boiling Runs: A Controlled Process to Form Reduced Graphene Oxide Surfaces from Graphene Oxide with Tunable Surface Chemistry and Morphology,” Ind. Eng. Chem. Res., **58**(17), pp. 7156–7165.

[62] Kandlikar, S. G., 2001, “A Theoretical Model to Predict Pool Boiling CHF Incorporating Effects of Contact Angle and Orientation,” J. Heat Transf., **123**(6), pp. 1071–1079.

[63] Chu, K.-H., Enright, R., and Wang, E. N., 2012, “Structured Surfaces for Enhanced Pool Boiling Heat Transfer,” Appl. Phys. Lett., **100**(24), p. 241603.

[64] Xu, X., Li, W., Wang, Y., Dong, G., Jing, S., Wang, Q., Feng, Y., Fan, X., and Ding, H., 2018, “Study of the Preparation of Cu-TiC Composites by Reaction of Soluble Ti and Ball-Milled Carbon Coating TiC,” Results Phys., **9**, pp. 486–492.

[65] Yazdani, A., and Isfahani, T., 2018, “Hardness, Wear Resistance and Bonding Strength of Nano Structured Functionally Graded Ni-Al2O3 Composite Coatings Fabricated by Ball Milling Method,” Adv. Powder Technol., **29**(5), pp. 1306–1316.

[66] Guo, W., and Chen, G., 2014, “Fabrication of Graphene/Epoxy Resin Composites with Much Enhanced Thermal Conductivity via Ball Milling Technique,” J. Appl. Polym. Sci., **131**(15), p. n/a-n/a.

[67] Qi, L., Tang, X., Wang, Z., and Peng, X., 2017, “Pore Characterization of Different Types of Coal from Coal and Gas Outburst Disaster Sites Using Low Temperature Nitrogen Adsorption Approach,” Int. J. Min. Sci. Technol., **27**(2), pp. 371–377.

[68] Gupta, A., Jaikumar, A., Kandlikar, S. G., Rishi, A., and Layman, A., 2018, “A Multiscale Morphological Insight into Graphene Based Coatings for Pool Boiling Applications,” Heat Transf. Eng., **39**(15), pp. 1331–1343.

[69] Shen, J., Hu, Y., Li, C., Qin, C., Shi, M., and Ye, M., 2009, “Layer-by-Layer Self-Assembly of Graphene Nanoplatelets,” Langmuir, **25**(11), pp. 6122–6128.

[70] Shen, J., Hu, Y., Li, C., Qin, C., and Ye, M., 2009, "Synthesis of Amphiphilic Graphene Nanoplatelets," Small, **5**(1), pp. 82–85.

[71] Swikker, K. R. J., Kanagasabapathy, H., Manickam, I. N., Nadar, N. V. P., and Alwin, S., 2020, "Effect of Sintering Temperature on Grain Growth and Mechanical Properties of Copper/Graphene Nanosheet Composite," Diam. Relat. Mater., **110**, p. 108111.

[72] Malard, L. M., Pimenta, M. A., Dresselhaus, G., and Dresselhaus, M. S., 2009, "Raman Spectroscopy in Graphene," Phys. Rep., **473**(5–6), pp. 51–87.

[73] Nemanich, R. J., and Solin, S. A., 1979, "First- and Second-Order Raman Scattering from Finite-Size Crystals of Graphite," Phys. Rev. B, **20**(2), pp. 392–401.

[74] Eckmann, A., Felten, A., Mishchenko, A., Britnell, L., Krupke, R., Novoselov, K. S., and Casiraghi, C., 2012, "Probing the Nature of Defects in Graphene by Raman Spectroscopy," Nano Lett., **12**(8), pp. 3925–3930.

[75] Ferrari, A. C., 2007, "Raman Spectroscopy of Graphene and Graphite: Disorder, Electron–Phonon Coupling, Doping and Nonadiabatic Effects," Solid State Commun., **143**(1–2), pp. 47–57.

[76] Casiraghi, C., Hartschuh, A., Qian, H., Piscanec, S., Georgi, C., Fasoli, A., Novoselov, K. S., Basko, D. M., and Ferrari, A. C., 2009, "Raman Spectroscopy of Graphene Edges," Nano Lett., **9**(4), pp. 1433–1441.

[77] Eckmann, A., Felten, A., Mishchenko, A., Britnell, L., Krupke, R., Novoselov, K. S., and Casiraghi, C., 2012, "Probing the Nature of Defects in Graphene by Raman Spectroscopy," Nano Lett., **12**(8), pp. 3925–3930.

[78] Tang, B., Guoxin, H., and Gao, H., 2010, "Raman Spectroscopic Characterization of Graphene," Appl. Spectrosc. Rev., **45**(5), pp. 369–407.

[79] Jaikumar, A., and Kandlikar, S. G., 2016, "Pool Boiling Enhancement through Bubble Induced Convective Liquid Flow in Feeder Microchannels," Appl. Phys. Lett., **108**(4), p. 041604.

[80] Ghosh, S., Bao, W., Nika, D. L., Subrina, S., Pokatilov, E. P., Lau, C. N., and Balandin, A. A., 2010, "Dimensional Crossover of Thermal Transport in Few-Layer Graphene," Nat. Mater., **9**(7), pp. 555–558.

[81] Potenza, M., Cataldo, A., Bovesecchi, G., Corasaniti, S., Coppa, P., and Bellucci, S., 2017, "Graphene Nanoplatelets: Thermal Diffusivity and Thermal Conductivity by the Flash Method," AIP Adv., **7**(7), p. 075214.

[82] Eckmann, A., Felten, A., Mishchenko, A., Britnell, L., Krupke, R., Novoselov, K. S., and Casiraghi, C., 2012, "Probing the Nature of Defects in Graphene by Raman Spectroscopy," Nano Lett., **12**(8), pp. 3925–3930.

[83] Malard, L. M., Pimenta, M. A., Dresselhaus, G., and Dresselhaus, M. S., 2009, "Raman Spectroscopy in Graphene," Phys. Rep., **473**(5–6), pp. 51–87.

[84] Ferrari, A. C., 2007, “Raman Spectroscopy of Graphene and Graphite: Disorder, Electron–Phonon Coupling, Doping and Nonadiabatic Effects,” Solid State Commun., **143**(1–2), pp. 47–57.

[85] Ghosh, S., Nika, D. L., Subrina, S., Pokatilov, E. P., Lau, C. N., and Balandin, A. A., 2009, “Dimensional Crossover of Thermal Transport in Few-Layer Graphene Materials,” p. 11.

[86] Yan, Z., Nika, D. L., and Balandin, A. A., 2014, “Review of Thermal Properties of Graphene and Few-Layer Graphene: Applications in Electronics,” p. 31.

[87] Potenza, M., Cataldo, A., Bovesecchi, G., Corasaniti, S., Coppa, P., and Bellucci, S., 2017, “Graphene Nanoplatelets: Thermal Diffusivity and Thermal Conductivity by the Flash Method,” AIP Adv., **7**(7), p. 075214.

[88] Hsu, Y. Y., 1962, “On the Size Range of Active Nucleation Cavities on a Heating Surface,” J. Heat Transf., **84**(3), pp. 207–213.

[89] Li, L., and Iskander, M., 2019, “Evaluation of Dynamic Image Analysis for Characterizing Granular Soils,” Geotech. Test. J., **43**(5), pp. 1149–1173.

[90] Hamilton, P., Littlejohn, D., Nordon, A., Sefcik, J., and Slavin, P., 2012, “Validity of Particle Size Analysis Techniques for Measurement of the Attrition That Occurs during Vacuum Agitated Powder Drying of Needle-Shaped Particles,” Analyst, **137**(1), pp. 118–125.

[91] Kruse, C., Tsubaki, A., Zuhlke, C., Anderson, T., Alexander, D., Gogos, G., and Ndao, S., 2016, “Secondary Pool Boiling Effects,” Appl. Phys. Lett., **108**(5), p. 051602.

[92] Malenkov, I. G., 1971, “Detachment Frequency as a Function of Size for Vapor Bubbles,” J. Eng. Phys., **20**(6), pp. 704–708.

[93] Dhir, V. K., 2018, “Nucleate Pool Boiling,” *Handbook of Thermal Science and Engineering*, Springer International Publishing, Cham, pp. 1645–1694.

7. Appendix

7.1 Uncertainty in heat flux:

The standard expression to calculate precision or biased uncertainties (U_a) is given by Equation 19, here 'a' is any property that is dependent on independent variable σ over n samples. U_σ term in the square root is the uncertainty associated to variable, σ.

$$U_a = \sqrt{\sum_{i=1}^{n} \left(\frac{\partial p}{\partial \sigma_i} U_{\sigma i}\right)^2} \tag{19}$$

The heat flux was calculated by Equation 20.

$$q^{"} = -k_{Cu}\left(\frac{3T_1 - 4T_2 + T_3}{2\Delta x}\right) \tag{20}$$

Using Equations (19) and (20) the percentage uncertainty associated to heat flux can be calculated as shown by Equation 21.

$$\frac{U_{q^{"}}}{q^{"}} = \sqrt{\frac{\left(\frac{\partial q^{"}}{\partial k_{Cu}} U_{k_{Cu}}\right)^2 + \left(\frac{\partial q^{"}}{\partial \Delta x} U_{\Delta x}\right)^2 + \left(\frac{\partial q^{"}}{\partial T_1} U_{T_1}\right)^2 + \left(\frac{\partial q^{"}}{\partial T_2} U_{T_2}\right)^2 + \left(\frac{\partial q^{"}}{\partial T_3} U_{T_3}\right)^2}{q^{"2}}} \tag{21}$$

For further simplification of Equation (21), a variable α is defined as shown in Equation 22.

$$\alpha = 3T_1 - 4T_2 + T_3 \tag{22}$$

Substituting this variable α in Eq. (20) will give,

$$q^{"} = -k_{Cu}\left(\frac{\alpha}{2\Delta x}\right) \tag{23}$$

The expressions of partial derivatives of variables in Equation (21) are derived using Equation (20) and are shown in Equations (24) – (28). The variable α as mentioned in Eq. (22) was used to simplify the expressions.

$$\frac{\partial q^{"}}{\partial k_{Cu}} = -\frac{\alpha}{2\Delta x} = \frac{q"}{k_{Cu}} \tag{24}$$

$$\frac{\partial q"}{\partial \Delta x} = -k_{Cu}\frac{\alpha}{2\Delta x^2} = -\frac{q"}{\Delta x} \tag{25}$$

$$\frac{\partial q"}{\partial T_1} = -k_{Cu}\frac{3}{2\Delta x} = \frac{3q"}{\alpha} \tag{26}$$

$$\frac{\partial q"}{\partial T_2} = -k_{Cu}\frac{-4}{2\Delta x} = \frac{-4q"}{\alpha} \tag{27}$$

$$\frac{\partial q"}{\partial T_3} = -k_{Cu}\frac{1}{2\Delta x} = \frac{q"}{\alpha} \tag{28}$$

Substituting the partial derivative terms in Equations (24) – (28) back in Equation (18), we obtain the following Equation 29.

$$\frac{U_{q"}}{q"} = \sqrt{\frac{\left(\frac{q"}{k_{Cu}}U_{k_{Cu}}\right)^2 + \left(-\frac{q"}{\Delta x}U_{\Delta x}\right)^2 + \left(\frac{3q"}{\alpha}U_{T_1}\right)^2 + \left(\frac{-4q"}{\alpha}U_{T_2}\right)^2 + \left(\frac{q"}{\alpha}U_{T_3}\right)^2}{q"^2}} \tag{29}$$

In Equation (29), by expanding the squared terms in the numerator and cancelling the $q"^2$ terms, we obtain Equation 30.

$$\frac{U_{q"}}{q"} = \sqrt{\left(\frac{U_{k_{Cu}}}{k_{Cu}}\right)^2 + \left(\frac{U_{\Delta x}}{\Delta x}\right)^2 + \left(\frac{3U_{T_1}}{\alpha}\right)^2 + \left(\frac{4U_{T_2}}{\alpha}\right)^2 + \left(\frac{U_{T_3}}{\alpha}\right)^2} \tag{30}$$

7.2 Uncertainty in wall superheat temperature:

The fundamental expression to calculate the uncertainty associated with wall temperature (T_w) is shown in Equation 31.

$$U_{T_w} = \sqrt{\sum_{i=1}^{n} \left(\frac{\partial T_w}{\partial \sigma_i} U_{\sigma i}\right)^2} \tag{31}$$

The percentage uncertainty of T_w can be calculated by using Equation (28). The expression is shown by Equation 32.

$$\frac{U_{T_w}}{T_w} = \sqrt{\frac{\left(\frac{\partial T_w}{\partial T_1} U_{T_1}\right)^2 + \left(\frac{\partial T_w}{\partial q"} U_{q"}\right)^2 + \left(\frac{\partial T_w}{\partial x_1} U_{x_1}\right)^2 + \left(\frac{\partial T_w}{\partial k_{Cu}} U_{k_{Cu}}\right)^2}{{T_w}^2}} \tag{32}$$

The partial derivative expressions of variables in Equation (29) are derived using Equation and are shown in Equations (33) – (36).

$$\frac{\partial T_w}{\partial T_1} = 1 - 0 = 1 \tag{33}$$

$$\frac{\partial T_w}{\partial q"} = 0 \; - 1\left(\frac{x_1}{k_{Cu}}\right) = -\left(\frac{x_1}{k_{Cu}}\right) \tag{34}$$

$$\frac{\partial T_w}{\partial x_1} = -\left(\frac{q"}{k_{Cu}}\right) \tag{35}$$

$$\frac{\partial T_w}{\partial k_{Cu}} = -q"x_1 \tag{36}$$

Substituting the partial derivative terms from Equations (33) – (36) back in the Equation (32), we obtain Equation (37) as shown below.

$$\frac{U_{T_w}}{T_w} = \sqrt{\frac{\left(U_{T_1}\right)^2 + \left(-\left(\frac{x_1}{k_{Cu}}\right)U_{q"}\right)^2 + \left(-\left(\frac{q"}{k_{Cu}}\right)U_{x_1}\right)^2 + \left(-q"x_1U_{k_{Cu}}\right)^2}{{T_w}^2}} \qquad (37)$$

Now in Equation (37), by expanding the squared terms in the numerator, we obtain Equation (38)

$$\frac{U_{T_w}}{T_w} = \sqrt{\frac{{U_{T_1}}^2}{{T_w}^2} + \frac{{U_{q"}}^2{x_1}^2}{{k_{Cu}}^2{T_w}^2} + \frac{{U_{x_1}}^2{q"}^2}{{k_{Cu}}^2{T_w}^2} + \frac{{U_{k_{Cu}}}^2{q"}^2{x_1}^2}{{T_w}^2}} \qquad (38)$$

7.3 Uncertainty in heat transfer coefficient:

The fundamental expression to calculate the uncertainty associated with the heat transfer coefficient (h) is shown in Equation (39).

$$U_h = \sqrt{\sum_{i=1}^{n}\left(\frac{\partial h}{\partial \sigma_i}U_{\sigma i}\right)^2} \qquad (39)$$

And the heat transfer coefficient is calculated using the following Eq. 40.

$$h = \frac{q"}{T_w - T_{sat}} \qquad (40)$$

The heat transfer coefficient can also be written in different forms:

$$\frac{h}{q''} = \frac{1}{T_w - T_{sat}} \; Or \quad h\,(T_w - T_{sat}) = q'' \; (41)$$

The percentage uncertainty of h can be calculated by using Equation (39) and (40). The expression is given by the following Equation (42):

$$\frac{U_h}{h} = \sqrt{\frac{\left(\frac{\partial h}{\partial q"} U_{q"}\right)^2 + \left(\frac{\partial h}{\partial T_w} U_{T_w}\right)^2 + \left(\frac{\partial h}{\partial T_{sat}} U_{T_{sat}}\right)^2}{h^2}} \qquad (42)$$

The percentage uncertainty of h can be calculated by using Equation (36) and are shown in Equations (43) – (45).

$$\frac{\partial h}{\partial q"} = \frac{1}{T_w - T_{sat}} = \frac{h}{q"} \qquad (43)$$

$$\frac{\partial h}{\partial T_w} = -\frac{q"}{(T_w - T_{sat})^2} = -\frac{h}{T_w - T_{sat}} = -\frac{h}{\Delta T_{sat}} \qquad (44)$$

$$\frac{\partial h}{\partial T_{sat}} = \frac{q"}{(T_w - T_{sat})^2} = \frac{h}{T_w - T_{sat}} = \frac{h}{\Delta T_{sat}} \qquad (45)$$

These terms are then substituted in the equation (42):

$$\frac{U_h}{h} = \sqrt{\frac{\left(\frac{h}{q"} U_{q"}\right)^2 + \left(\frac{-h}{T_w - T_{sat}} U_{T_w}\right)^2 + \left(\frac{h}{T_w - T_{sat}} U_{T_{sat}}\right)^2}{h^2}} \qquad (46)$$

Solving this equation further, will give the final expression for the uncertainty in heat transfer coefficient, given by Equation (47).

$$\frac{U_h}{h} = \sqrt{\frac{U_{q"}^2}{q"^2} + \frac{U_{T_w}^2}{\Delta T_{sat}^2} + \frac{U_{T_{sat}}^2}{\Delta T_{sat}^2}} \qquad (47)$$

7.4 Publication list:

7.4.1 Journal Papers:

1) **Rishi, A. M.**, Rozati, S. A., Trybus, C., Kandlikar, S. G., and Gupta, A., **2021**, "Investigation of Structure-Property-Boiling Enhancement Mechanisms of Copper/Graphene Nanoplatelets Coatings," Front. Mech. Eng., 7, p. 642214.
2) **Rishi, A. M.**, Kandlikar, S. G., Rozati, S. A., and Gupta, A., **2020**, "Effect of Ball Milled and Sintered Graphene Nanoplatelets–Copper Composite Coatings on Bubble Dynamics and Pool Boiling Heat Transfer," Adv. Eng. Mater., 22(7), p. 1901562. (Featured on the Journal Cover)
3) **Rishi, A. M.**, Kandlikar, S. G., and Gupta, A., **2020**, "Salt Templated and Graphene Nanoplatelets Draped Copper (GNP-Draped-Cu) Composites for Dramatic Improvements in Pool Boiling Heat Transfer," Sci. Rep., 10(1), p. 11941.
4) **Rishi, A. M.**, Kandlikar, S. G., and Gupta, A., **2019**, "Improved Wettability of Graphene Nanoplatelets (GNP)/Copper Porous Coatings for Dramatic Improvements in Pool Boiling Heat Transfer," Int. J. Heat Mass Transf., 132, pp. 462–472.
5) **Rishi, A. M.**, Kandlikar, S. G., and Gupta, A., **2019**, "Repetitive Pool Boiling Runs: A Controlled Process to Form Reduced Graphene Oxide Surfaces from Graphene Oxide with Tunable Surface Chemistry and Morphology," Ind. Eng. Chem. Res., 58(17), pp. 7156–7165.
6) **Rishi, A. M.**, Gupta, A., and Kandlikar, S. G., **2018**, "Improving Aging Performance of Electrodeposited Copper Coatings during Pool Boiling," Appl. Therm. Eng., 140, pp. 406–414.
7) Negi, A., **Rishi, A. M.**, and Kandlikar, S. G., **2021**, "Effect of Heat Flux on Bubble Coalescence Phenomena and Sound Signatures During Pool Boiling," J. Heat Transf., 143(051601).
8) Jaikumar, A., **Rishi, A.**, Gupta, A., and Kandlikar, S. G., **2017**, "Microscale Morphology Effects of Copper–Graphene Oxide Coatings on Pool Boiling Characteristics," J. Heat Transf., 139(11), p. 111509.
9) Gupta, A., Jaikumar, A., Kandlikar, S. G., **Rishi, A.**, and Layman, A., **2018**, "A Multiscale Morphological Insight into Graphene Based Coatings for Pool Boiling Applications," Heat Transf. Eng., 39(15), pp. 1331–1343.

7.4.2 Conference papers:

1) **Rishi, A. M.**, and Gupta, A., **2020**, "Fundamental Insight on Morphological Changes of Graphene Nanoplatelets-Copper (GNP-Cu) Coatings: Effects of Repetitive Pool Boiling Tests," ASME 2020 18th International Conference on Nanochannels,

Microchannels, and Minichannels, American Society of Mechanical Engineers, Virtual, Online, p. V001T12A003.

2) **Rishi, A. M.**, Gupta, A., and Kandlikar, S. G., **2018**, "Improving Liquid Supply Pathways on Graphene Oxide Coated Surfaces for Enhanced Pool Boiling Heat Transfer Performance," ASME 2018 16th International Conference on Nanochannels, Microchannels, and Minichannels, American Society of Mechanical Engineers, Dubrovnik, Croatia, p. V001T03A003.
3) **Rishi, A. M.**, Gupta, A., and Kandlikar, S. G., **2017**, "Electrodeposition of Selective Anions with Non-Electrolyte Bath for Enhancing the Pool Boiling Performance," Sri Lanka, p. 7.
4) Negi, A., **Rishi, A. M.**, and Kandlikar, S. G., **2020**, "Effect of Heat Flux on Bubble Coalescence Phenomena and Sound Signatures During Pool Boiling,", ASME 2020 18th International Conference on Nanochannels, Microchannels, and Minichannels, American Society of Mechanical Engineers, Virtual, Online, p. V001T09A001.
5) Raghupathi, P., Owens, A., Steinke, M., Lin, T. Y., Kalani, A., Moreira, D., Gonzalez-Hernandez, J.-L., Lu, Z., Banerjee, R., Daino, M., Jaikumar, A., Chauhan, A., **Rishi, A.**, Perez-Raya, I., Emery, T., and Guimarães Aguilar, F., **2020**, "Insight to Innovation: An Overview of Research Journey of Dr. Satish Kandlikar," ASME 2020 18th International Conference on Nanochannels, Microchannels, and Minichannels, American Society of Mechanical Engineers, Virtual, Online, p. V001T12A006.

7.4.3 Conference presentations:

1) **Rishi, A.**, Kandlikar, S., and Gupta, A., **2018**, "Application of Novel Porous Graphene Nanoplatelets Composites for Enhanced Heat Transfer Properties," American Institute of Chemical Engineers (AIChE) Annual Meeting.
2) **Rishi, A.**, Gupta, A., and Kandlikar, S., **2019**, "Repetitive Pool Boiling Runs: A Controlled Process to Form Reduced GO Surfaces from GO with Tunable Surface Chemistry and Morphology," American Institute of Chemical Engineers (AIChE) Annual Meeting.
3) **Rishi, A.**, and Gupta, A., **2019**, "Copper-Carbon Nanomaterial Composite Coatings for Dramatic Improvements in Phase Change Heat Transfer," American Institute of Chemical Engineers (AIChE) Annual Meeting.
4) **Rishi, A.**, Gupta, A., and Kandlikar, S., **2019**, "Transformation of GO Surfaces to Reduced-GO Surfaces with Tunable Surface Chemistry and Morphology Via Pool Boiling Process," American Institute of Chemical Engineers (AIChE) Annual Meeting.